CHEMOSTRATIGRAPHY OF THE GRIQUALAND WEST BASIN, SOUTH AFRICA BETWEEN 2.65 AND 2.5 GA: EVIDENCE FOR A MANTLE PLUME EVENT?

by

Christina L. Calvin

Submitted in Partial Fulfillment of the Requirements of the Degree of

Masters of Science in Geology

New Mexico Institute of Mining and Technology
Department of Earth and Environmental Science

Socorro, New Mexico, USA

June 2003

This thesis is accepted on behalf of the
Faculty of the Institute by the following committee:

Advisor

July 1, 2003
Date

I release this document to the New Mexico Institute of Mining and Technology.

Student's Signature

6/27/03
Date

Abstract

Mantle plume events are episodes of Earth's history during which several large mantle plumes rise to the Earth's surface with in a short period of time (<100Ma). These events are characterized by increased oceanic crust production and fast mid-ocean ridge spreading. Several geological indicators of mantle plume events have been correlated with these periods of intense magmatism, including increases in eustatic sea level, deposition of banded iron formations, increases in preserved black shale deposits, and increased plutonism at subduction margins. These four characteristics have all been identified at approximately 2.5 Ga. This study looks at sedimentary rocks deposited between 2.65 and 2.5 Ga in marine waters in an attempt to characterize the chemistry of the ocean water leading up to the mantle plume event at 2.5 Ga. $\delta^{13}C_{carb}$, $\delta^{18}O$, and trace metal concentrations were analyzed on carbonate samples. $\delta^{13}C_{org}$ and $\delta^{34}S$ were analyzed on black shales, interbedded with the carbonates. The $\delta^{13}C_{carb}$ and $\delta^{34}S$ values were anticipated to experience a positive excursion while $\delta^{13}C_{org}$ would experience a negative excursion. In addition, the fractionation between $\delta^{13}C_{org}$ and $\delta^{13}C_{carb}$ was expected to increase. Trace metal concentrations were expected to increase possibly by a factor of 2. In fact, the samples analyzed were remarkably homogenous throughout the stratigraphic column deposited between 2.65 and 2.5 Ga. Meanwhile, prior studies indicate a positive excursion is experienced in the $\delta^{13}C_{carb}$ after the onset of the mantle plume event at 2.45 Ga. This leads to speculation that the expected change in the geochemistry of ocean waters may have a 10 Ma lag from the onset of the mantle plume event.

Acknowledgments

I would first like to thank my advisor and my committee for their time and insight throughout the course of my thesis. In addition, I would like to thank Wlady Altermann for sharing his knowledge of the Griqualand West basin before, during, and after I completed my field work. Without his time and expertise, I would not have been able to complete this project. Special thanks goes to the Geological Society of America, Sigma Xi, the University of Pretoria in South Africa, and University of Maryland for providing funding to complete this project. I would also like to thank the many people who helped me prep and run my samples, specifically Jessica Cox, Bonnie Frey, Amber McIntosh, and Terry Thomas. Thank you to Nicole Hoffman, Sara McNamara, Erin Phillips, Jennifer Wilson and again to Jessica Cox for the many hours spent listening to me discuss the same aspects of my thesis over and over and over again and for always being supportive during those discussions. And finally, I would like to thank my family and my best friend Kate Matula for their constant encouragement.

Table of Contents

List of Figures

List of Tables

List of Appendices

1 Introduction

The geological record between 2.5 and 2.45 Ga exhibits several interesting features. The largest banded iron formation deposits in the world were deposited at this time over parts of southern Africa and Australia (Klemm, 2000; Isley and Abbott, 1999). Likewise, there are large deposits of preserved black shales that formed during a global marine transgression (Altermann and Siegfried, 1997). A significant number of large igneous intrusions, including the Great Zimbabwe Dyke in Africa, are dated at 2.46 Ga. The Matachewan and Hearst dike swarms of North America are dated at 2.47 and 2.45 Ga, respectively (Heaman, 1997). Together, these interesting geological features suggest a mantle plume event occurred at approximately 2.5 Ga (Larson, 1991). A mantle plume event is a period of time during which several large mantle plumes produce eruptions at the surface of the Earth (Condie, 2001). Mantle plume events are often accompanied by increased rates of ocean-ridge spreading and increased emplacement of plutons and dikes.

In order to investigate the presence of a mantle plume event at 2.5 Ga, this study looks at the geochemistry of carbonates and shales deposited on the Kaapvaal craton of southern Africa between 2.65 and 2.5 Ga. The carbonates are analyzed for trace metals and the carbonate carbon and oxygen isotopic signatures, while the interbedded shales are analyzed for sulfur and organic carbon isotopes. By looking at a period of uninterrupted deposition in this basin, changes in the geochemistry of the ocean should be preserved in the sedimentary sequence and may record changes that could be related to a mantle plume event at 2.5 Ga.

2 Mantle Plume Events

Mantle plumes are believed to be derived from the D'' layer at the core/mantle interface (Condie, 2001). During a mantle plume event, many large mantle plumes rise to the base of the lithosphere in a short period of time (<100 My). Several large mantle plume-derived eruptions within a short time frame can result in significant changes to the biological, geological, and environmental conditions of the Earth. In fact, mantle plume events have been shown to correlate with a wide variety of local and global changes. For example, during the Mid-Cretaceous, a mantle plume event coincided with increases in surface temperature, deposition of black shales, a rise in sea level, elevated $\delta^{13}C$ in seawater and a decrease in the rate of magnetic pole reversals (Larson, 1991; Kerr, 1998). In addition, proposed mantle plume events at 2.7 and 1.9 Ga are associated with enhanced chemical weathering corresponding to warm paleoclimates, peaks in the volume of preserved black shale and banded iron formations, and increases in global sea level (Condie, 2000; 2001). With the exception of magnetic pole reversals, the effects mentioned above are all direct effects of an increase in volcanic activity at the surface of the Earth, specifically in the ocean. Therefore, in the absence of preserved oceanic crust, conditions such as increases in sea level, black shale production and banded iron formation deposition can be used as proxies for mantle plumes (Isley and Abbott, 1999).

2.1 Proxies for Mantle Plume Events

During a mantle plume event, above average volumes of magma are produced in plume heads. When magma is erupted as part of oceanic crust, it increases the rate of oceanic crust production (Force, 1984). In addition, changes in mantle convection may increase the rate of sea-floor spreading. Increased production of oceanic crust has two

major effects. First, there is an increase in the subduction rate beneath continental margins (Larson and Pitman, 1972); this leads to an increase in plutonism above subducting slabs. A second effect of increased production of oceanic lithosphere is an increase in global sea level as ocean water is displaced onto continental shelves (Larson, 1991). Schlanger et al. (1981) calculated the rate of subsidence in the Pacific basin and found that it had not subsided at a constant rate. They further found that increases in volcanic activity beneath the Pacific plate resulted in uplift of the oceanic crust and hypothesized that this may be due to heating of the lithosphere. Uplift of oceanic crust displaces water onto the continents and results in water covering more global surface area (Force, 1984).

In addition to increased oceanic crust production, a mantle plume event also may increase global temperatures (Larson, 1991). There are three ways in which mantle plumes may cause an increase in global temperatures (Force, 1984). First, widespread volcanism increases CO_2 output, which in turn increases the greenhouse effect in the atmosphere and traps heat at the surface of the Earth. A second effect of mantle plume activity is a rise in sea level (Schlanger et al., 1981). As a consequence of the expanding ocean surface, absorption of solar radiation increases, which serves to further heat the surface of the ocean. The third effect that mantle plumes have on the climate of the Earth is a change in ocean circulation patterns. As sea level rises and global temperatures increase, the temperatures at the poles increase at a different rate than at the equator (Force, 1984). Decreased glaciation at the poles decreases albedo at the poles more quickly than at the equator. Thus the temperature increases at the poles at a much faster rate than at the equator. The differential warming of the Earth disrupts the density

controlled circulation pattern in the oceans. Changes in the circulation patterns of the oceans have the effect of increasing stratification in the oceans (Derry et al., 1992). Only the top portion of the oceans remain oxic, while the lower portions of the ocean become anoxic, creating an oxygen sink.

Another effect of widespread mantle plume activity is an increase in production of black shales and the burial of the organic precursors of oil and coal (Larson, 1991). Because black shales are composed of organic matter that is deposited under anoxic conditions, increase in black shale deposition can be the result of two causes: increases in total organic matter and/or an increase in anoxic depositional environments. (Force, 1984). These conditions can be attributed to increases in marine volcanism. In the case of increasing total organic matter, mid-ocean ridges and marine hotspot volcanism provide an influx of mineral nutrients to the oceans. Increases in available nutrients in seawater lead to increases in organic matter. Likewise, changes in ocean circulation patterns increase the anoxic environments of the oceans (Derry et al., 1992; Jahren, 2002). There are two proposed causes for the change in ocean circulation patterns. In the first scenario, differential warming of the Earth's surface, caused by changes in the Earth's albedo due to rising sea level, produces changes in the thermal characteristics of the ocean. In the second scenario, large amounts of methane released from methane hydrates alter the chemical cycling of the ocean. As with the rise in sea level, increasing methane, a greenhouse gas, causes differential warming of the Earth's surface, which alters the thermal circulation of the oceans. In both scenarios, O_2 is delivered to parts of the ocean that would ordinarily be anoxic and the O_2 is rapidly utilized creating an oxygen sink. Furthermore, reduced inorganic C is brought up from anoxic depths,

providing another oxygen sink. Mantle plumes can also create anoxic conditions through the input of large volumes of reduced gases such as methane (CH_4) at submarine volcanoes and hydrothermal vents. In addition, reduced metals are also released into the oceans. The reduced metals act as an uptake for O_2. The anoxic environments that mantle plumes create in the oceans provide an environment suitable for organic material to be deposited and preserved (Force, 1984; Des Marais et al., 1992). Not surprising, increases in oil and coal reserves, which depend upon anoxic depositional environments, have been linked to mantle plume events as well.

Banded iron formations have also been correlated with mantle plume events. Several observations have been made between the appearance of large-scale igneous activity and the appearance of banded iron formations (Barley et al., 1997; Garzanti, 1993). Isley and Abbott (1999) quantified the appearance of large igneous intrusions, komatiites, and continental flood basalts around the globe. They correlated this data to the ages and volumes of banded iron formation deposition. Their research shows a temporal correlation between the appearance of large volumes of igneous rocks and the appearance of banded iron formations. Furthermore, they have calculated that there is a 1 to 3 My time lag between the onset of mantle plume activity at the surface of the Earth and the onset of sedimentation of banded iron formation. Simonson and Hassler (1996) linked the formation of banded iron formations with increases in sea level. They studied stratigraphy from 6 regions: the Labrador Trough, Animikie-Mesabi, Animiki-Gunflint, Nabberu, Transvaal, and Hamersley. In all of these regions, marine transgressions immediately proceeded deposition of banded iron formations.

Mantle plume events also have been correlated with extended periods without magnetic pole reversals (Larson and Pitman, 1972). Two extended periods without a reversal of the magnetic poles have been observed by developing magnetic reversal models in the Pacific Ocean. The first occurred in during the middle Jurassic. The second event occurred during the Cretaceous. These two magnetic anomalies were then correlated to periods of rapid mid-ocean ridge spreading, which is a key indicator of a mantle plume event.

2.2 Mantle Plume Event at 2.5 Ga?

Based on the previous discussion of proxies for mantle plume events, several geological anomalies suggest that there may have been a mantle plume event at approximately 2.5 Ga. Among these indicators are a large increase in the number of black shale and banded iron formations, and an increase in the number of giant dyke swarms, flood basalts, and layered intrusions (Isley and Abbott, 1999). At this time, stromatolite populations underwent an increase both in population size and diversity that is closely linked to a global marine transgression (Eriksson et al., 1999; Simonson and Hassler, 1996). In addition to the geological anomalies that suggest the possibility of a mantle plume event, evidence has been presented for the existence of a mantle plume beneath the Baltic Shield at 2.45 Ga (Puchtel et al., 1997).

Black shales, which form from the deposition of organic-rich sediments in anoxic conditions, were prevalent in the Griqualand West basin in the Kaapvaal craton of southern Africa (Altermann and Siegfried, 1997). Furthermore, between 2.5-2.4 Ga, banded iron formations were deposited in several locations: South Africa, Australia, Brazil, and Baltica (Isley and Abbott, 1999). Isley and Abbott (1999) have estimated that

if these deposits were forming concurrently, they would comprise at least 40% and possibly as much as 60% of all known banded iron formations deposits ever deposited.

At the same time, several large dyke swarms were emplaced including the Scourie dike swarm of Scotland, The Great Dyke of the Zimbabwe craton; tholeiite dikes of the Vestfold craton in Antarctica, and the Bangalore dike swarm of the Dharwar craton, India (Heaman, 1997). Layered mafic intrusions and flood basalts were formed on the Karelian craton of Finland and Russia and the Jimberlana intrusion was intruded into the Yilgarn craton of Australia. Because all these events have been dated between 2.42 and 2.46 Ga and have similar geochemical signatures, Heaman (1997) collectively calls this magmatism the Matachewan Igneous Event and estimates that the total volume intruded may be greater than 250,000 km^2. Studies of komatiites intruded into the Baltic shield between 2.42 and 2.46 Ga indicate that these magmas may have had temperatures of 1630°C (Puchtel et al., 1997). This temperature is significantly hotter than the surrounding mantle and supports the existence of a mantle plume beneath the Baltic shield.

2.3 Testing for a Mantle Plume Event using Geochemistry

With the understanding that mantle plume events can have various effects on the paleoclimate of the Earth, it may be possible to look for evidence of a mantle plume event in the geological record. In the absence of preserved oceanic crust, one way to look for evidence of mantle plume events is through the geochemistry of seawater. Certain chemical characteristics are retained in the formation of marine sedimentary rocks. Amongst these characteristics are the carbon, oxygen, and sulfur isotopes and the trace element concentrations of the rocks. Observed changes in the geochemical signatures of

marine carbonates and shales may provide evidence of wide-spread magmatic activity within the oceans.

Carbon has two stable isotopes: ^{12}C and ^{13}C. Over 99.9% of carbon in the lithosphere is housed in the sedimentary reservoirs or a metamorphic equivalent (Schidlowski, 1995). Carbon in sediments and sedimentary rocks occurs as either carbonate carbon or organic carbon. Carbonate carbon (C_{carb}) is deposited in the form of calcite or dolomite either through inorganic precipitation or by organisms as oxidized carbon. Organic carbon (C_{org}) is carbon that is deposited as reduced carbon. Original mantle values for $\delta^{13}C$ are estimated to be approximately –5 ‰ (PDB). $\delta^{13}C_{org}$ is closer to -25‰ (PDB) due to biological fractionation, which preferentially incorporates ^{12}C. For example, autotrophic organisms that use CO_2 and dissolved bicarbonate (HCO_3^-) preferentially use ^{12}C over ^{13}C as a source for cellular carbon (Karhu, 1993). Therefore, organic carbon is isotopically lighter than the surrounding seawater, increasing the ^{13}C available for incorporation into carbonate carbon. Typical $\delta^{13}C_{carb}$ values are approximately 0‰ (PDB).

Previous studies of carbonates in the Griqualand West basin at 2.5 Ga indicate that the $\delta^{13}C_{carb}$ values are lighter than modern values (Watanabe et al., 1997). Futhermore, carbon isotopic values from the Fennoscandian shield indicate that carbonate carbon experienced a negative excursion at the same time (Karhu, 1993; Melezhik and Fallick, 1996). Condie et al. (2000, 2001) have suggested that during a mantle plume event, the ratio of $\delta^{13}C_{org}$ to $\delta^{13}C_{carb}$ is controlled by hydrothermal fluxes on the seafloor, anoxia, and disrupted ocean currents. As the rate of organic carbon burial increases, there is a corresponding increase in the value of $\delta^{13}C_{carb}$. Kump and Arthur (1999)

experimentally determined that periods of increased volcanic activity have a larger effect on organic carbon than on carbonate carbon. They have attributed this to the increase in atmospheric pCO_2, which increases the available carbon for marine photosynthetic organisms through exchange with ocean water. Marine organisms may incorporate more ^{12}C than normal due to the increased availability of carbon. This leads to an increase in the burial of anomalously light organic matter. Therefore, it might be possible to track the onset of large-scale volcanism by comparing the isotopic value for carbonate carbon and its organic counterparts.

In addition to carbon isotopes, sulfur isotopes should also be affected during a mantle plume event, because they are strongly fractionated by temperature, biologic processes and atmospheric reactions (Ohmoto and Felder, 1987; Farquahar et al., 2000). During a mantle plume event, $\delta^{34}S$ should increase in marine sulfides. There are two mechanisms by which $\delta^{34}S$ should increase. First, increased hydrothermal activity, as a result of the mantle plumes, increases the Fe^{+2}, which would, in turn, causes an increase in pyrite (FeS_2) precipitation (Derry and Jacobsen, 1990). Pyrite preferentially incorporates ^{32}S over ^{34}S out of seawater, causing seawater to become enriched in ^{34}S. The second mechanism for ^{34}S enrichment is caused by reactions that occur in the atmosphere (Farquahar et al., 2000). During a mantle plume event, reduced gases such as methane make up the majority of gas injected into the atmosphere/ocean system (Pavlov et al., 2000). Because there is less oxygen available for bacterial sulfate reduction, this leads to a decrease in the sulfate production rate, and therefore, a decrease in sulfate burial rate. To maintain mass balance, $\delta^{34}S$ in seawater increases which is reflected by sulfide deposition. Likewise, sulfate-reducing bacteria should increase during a mantle

plume event due to the injection of sulfur gases and methane into seawater. Sulfate-reducing bacteria preferentially use ^{32}S over ^{34}S, which would also increase $\delta^{34}S$ in seawater (Ohmoto et al., 1993). A high $\delta^{34}S$ ratio in Griqualand West sediments between 2.65 and 2.5 Ga would support the theory that a mantle plume event occurred at this time.

Weathering of continental material and hydrothermal inputs are the primary controls on trace elements concentration in seawater (Fryer et al., 1979). However, during the Precambrian, hydrothermal inputs have a stronger influence over trace metal concentrations than continental inputs. Pb, Mn, Fe, Zn, Ba, Sr, Cu, Ca, As, Sb, Ni, Hg, Ag, Mo, and W are found in waters of hydrothermal origin in concentrations of 1 to 2 orders of magnitude higher than in waters of continental origin. Therefore, an increase in hydrothermal activity during a mantle plume event may lead to an increase in trace metal concentrations in seawater.

3 The Kaapvaal Craton

3.1 The Kaapvaal Craton between 2.7 and 2.5 Ga

In order to use geochemistry to test for a mantle plume event at 2.5 Ga, it is necessary to find a suite of rocks that was deposited under similar depositional conditions leading up to and if possible continuing through the mantle plume event at 2.5 Ga. Unfortunately, the global deposition of banded iron formations beginning at approximately 2.5 Ga followed by a global marine regression prohibited the deposition of carbonates after the onset of the mantle plume event. However, the Griqualand West basin on the Kaapvaal craton has large carbonate deposits that were continuously deposited from approximately 2.65 Ga until 2.5 Ga and therefore makes it a suitable site for examining the geochemistry of the ocean water immediately prior to the mantle plume event (Figure 1).

The formation of the Kaapvaal Craton began approximately 3.7 Ga (Thomas et al., 1993). The formation of the Griqualand West basin begins with the Limpopo Orogeny between approximately 2.7 and 2.6 Ga (Thomas et al., 1993). The Limpopo Orogeny has been modeled as an oblique collision between the Kaapvaal craton and the Zimbabwe craton similar to the processes occurring in the Himalayas (Clendenin et al., 1988; Treloar et al., 1992). During the orogeny, the collision zone was uplifted, and a zone of foreland extension and compression was created on the Kaapvaal craton (Figure 2).

Three major basins formed during the Limpopo orogeny through foreland extension: the Griqualand West basin, the Kanye basin, and the Transvaal basin (Altermann and Nelson, 1998; Thomas et al., 1993; de Wit et al., 1992). Figure 1 is a

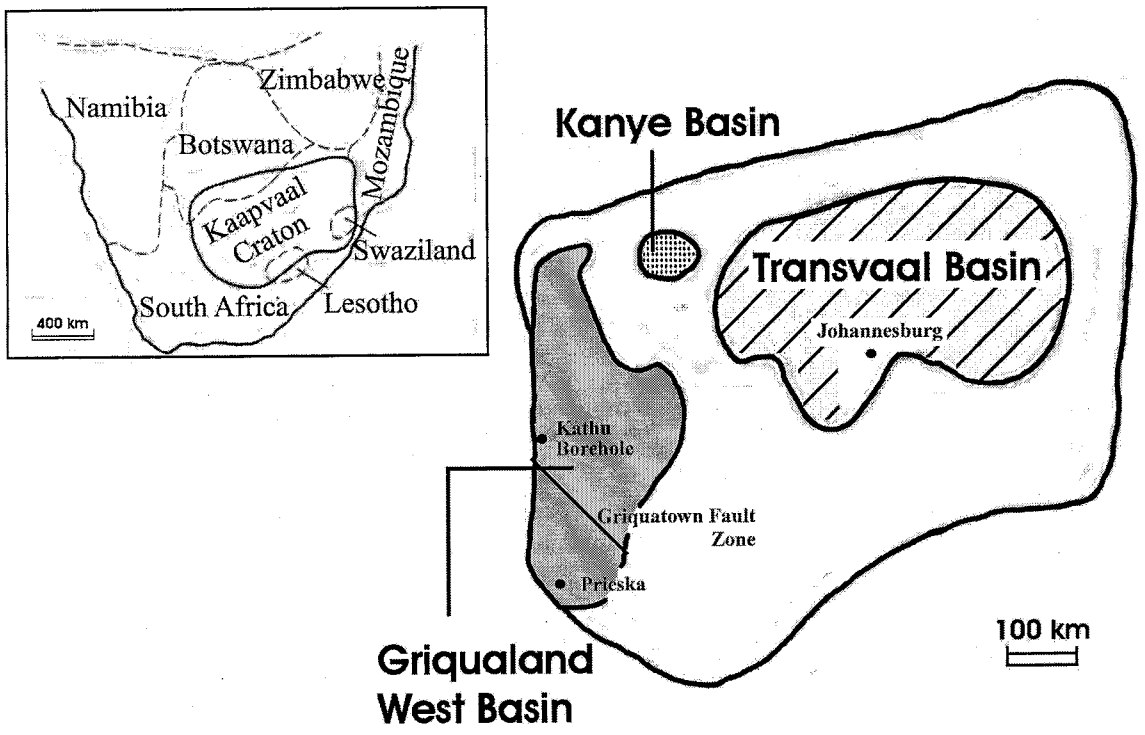

Figure 1: Map of the Kaapvaal craton with the location of three Archean basins that formed during the marine transgression between 2.7 and 2.4 Ga (after Eriksson et al., 2001). The Prieska facies occur south of the Griquatown fault zone while the Ghaap Plateau facies occur north of the fault zone.

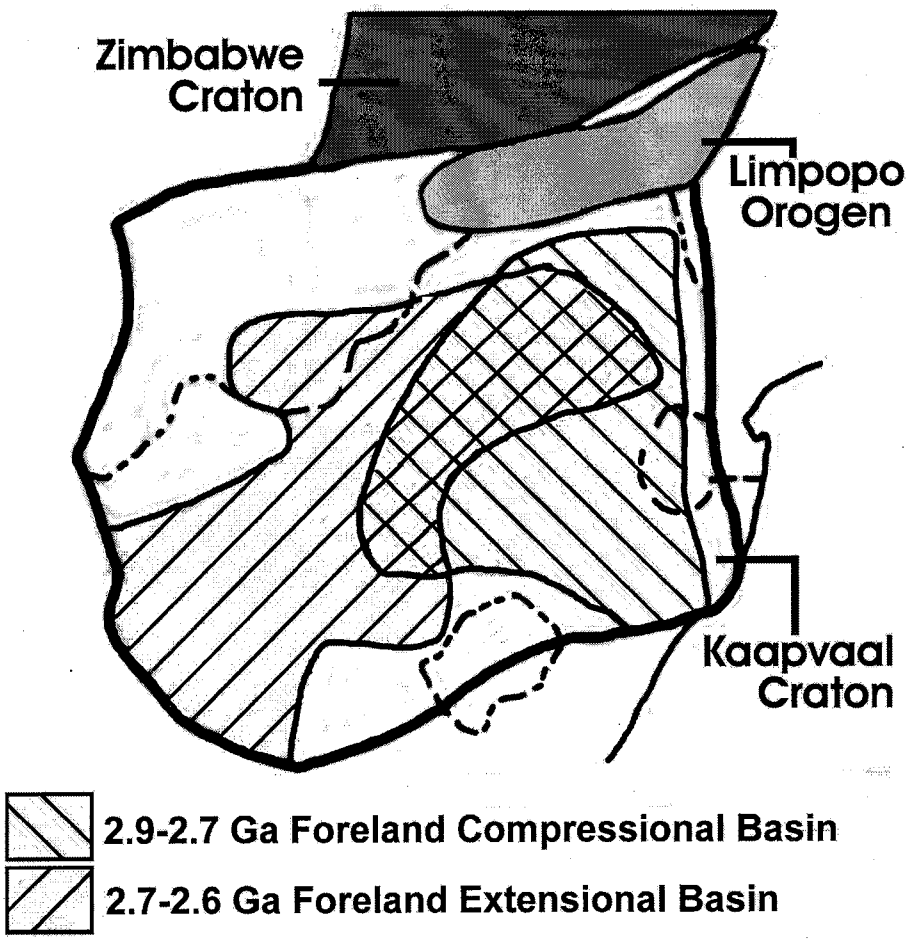

Figure 2: Diagram of extension and compression zones in the Kaapvaal craton during the Limpopo Orogeny (after de Wit et al., 1992).

map of the Kaapvaal craton with the locations of the three basins. Between 2.65 and 2.5 Ga, marine water transgressed from the southwest portion of the craton towards the northeast portion of the craton. The Griqualand West basin, located in the Northern Cape Province of South Africa, formed south and west of the Kanye and Transvaal basins and represents the deepest waters of the transgressive epeiric sea. The Kanye basin, the smallest of the three basins, is located in Botswana. It is located almost directly north of the Griqualand West basin. The Transvaal basin is located to the northeast of the Griqualand West basin in the Transvaal region of South Africa. Because of its location, the Transvaal basin has carbonate rocks that were deposited in the shallowest waters of the epeiric sea.

The Griqualand West basin is divided into two facies: the Prieska facies and the Ghaap Plateau facies. Figure 1 shows the orientation of the Griquatown Fault, which separates these two facies. Sedimentary rocks deposited in either the Schmidtsdrif or Cambellrand Subgroups north and east of the Griquatown Fault are known as the Ghaap Plateau facies. Sedimentary rocks deposited during the same time frame south and west of the Griquatown Fault are known as Prieska facies. Figure 3 shows the time correlation between the sedimentary sequences in the Prieska and Ghaap Plateau facies. The Schmidtsdrif and Cambellrand subgroups are part of the Ghaap stratigraphic group and the Transvaal Supergroup (Altermann and Siegfried, 1997). The Schmidtsdrif Subgroup, the older of the two carbonate platforms, lies unconformably on the rocks of the Ventersdorp Supergroup, which is composed predominantly of basaltic lava flows. The Schmidtsdrif Subgroup is composed of stromatolitic carbonates, siliclastic sediments and basaltic lava flows. The Cambellrand Subgroup, the younger of the two carbonate

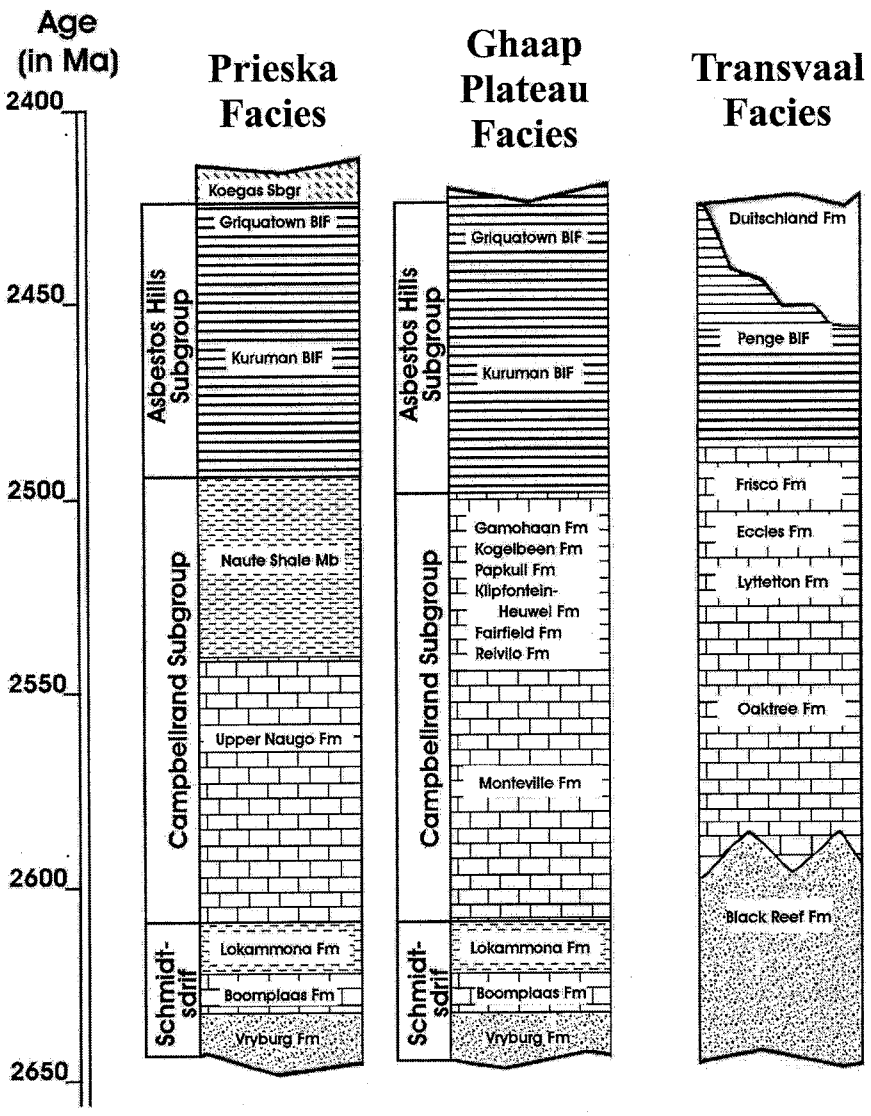

Figure 3: Three stratigraphic columns from the Kaapvaal craton showing the change in lithology with region. The Prieska facies represent the stratigraphy south of the Griquatown fault in the Griqualand West basin. The Ghaap Plateau facies represent the stratigraphy north of the Griquatown fault in the Griqualand West basin. The Transvaal facies are from the Transvaal basin (after Eriksson et al., 1999).

platforms, is overlain by the banded iron formations of the Asbestos Hills subgroup. In the Prieska facies nomenclature, the Schmidtsdrif and Cambellrand Subgroups are called the Nauga Formation. The Nauga Formation is considerably thinner than the corresponding units in the Ghaap Plateau facies. The Griquatown fault has not been observed through field observations but has been inferred to explain the lower rate of sedimentation in the Prieska facies (pers comm. W. Altermann, 2002). The difference in thickness between the Prieska facies and the Ghaap Plateau facies has also been attributed to differences in water depth (Eriksson and Altermann, 1998). Because the Prieska facies formed south of the Ghaap Plateau facies, they formed closer to the marine inlet of the epeiric sea. Therefore, the Prieska facies represents the deepest deposits of the epeiric sea. Regardless of the original cause of the variation in stratigraphic thickness, the two facies have been correlated using tuff layers.

The Griqualand West, Transvaal, and Kanye basins have similar lithostratigraphy and are believed to have formed simultaneously between 2.709 and 2.642 Ga (Altermann and Nelson, 1998). Although there are no outcrops that connect the Transvaal basin with the Griqualand West basin, these two basins were both deposited on top the Ventersdorp lava and therefore have been assumed to be continuous during the Archean. Figure 3 shows the stratigraphy that formed in the Transvaal basin and the Griqualand West basin. The Transvaal basin is represented by the Transvaal facies. The Griqualand West basin is divided into the Prieska and Ghaap Plateau facies.

The deposition of the carbonates is believed to be the result of an epeiric sea that transgressed onto the continent in a N-NE direction (Tankard et al., 1982; Clendenin et al., 1988). At approximately 2.55 Ga, another marine transgression increased water

depths throughout the basin (Altermann and Nelson, 1998). This transgression was followed by deposition of Superior-type banded iron formations, that have rare earth element signatures consistent with banded iron formations of geothermal origin. At its peak, the epeiric sea is estimated to have covered at least 500,000 km^2 of the Kaapvaal Craton (Tankard et al., 1982). During this time, the Griqualand West, Transvaal, and Kanye basins were most likely joined by marine seaways (Eriksson et al., 1991). By the time the epeiric sea had regressed, two distinct carbonate platforms had developed: the Schmidtsdrif and the Cambellrand Subgroup, which combine to form the oldest giant carbonate shelf on Earth (Eriksson and Altermann, 1998; Altermann and Siegfried, 1997).

The ages attributed to the early formation of the basins were ascertained by dating zircons in the underlying Ventersdorp Supergroup and lava at the base of the Vryburg Formation (Altermann and Nelson, 1998). Zircons from the upper portion of theVentersdorp Supergroup were dated at 2709 Ma (Armstrong et al., 1991). Zircons from lava at the base of the unconformably overlying Vryburg Formation was dated at 2642 +/- 3 Ma (Altermann and Nelson, 1998). These two dates provide the lower limit of deposition for the carbonate shelves in the Transvaal and Griqualand West basins.

Altermann and Nelson (1998) used U-Pb ages from zircons found in tuff layers to correlate the deposition of the Prieska and Ghaap plateau facies of the Griqualand West basin with the Transvaal facies of the Transvaal basin (Figure 3). The upper limit of the Cambellrand Subgroup in both basins is defined by a nonconformity between the Cambellrand Subgroup and the Kuruman Iron Formation. The age of this unconformity has been estimated previously based on a zircon age of 2521 +/- 3 Ma (Sumner and

Bowring, 1996). This zircon occurs in an ash bed in the Transvaal basin that was deposited 40-50 m below the unconformity. Altermann and Nelson (1998) dated zircons from an ash bed deposited 40 m below the nonconformity that separates the Cambellrand Subgroup and Kuruman Iron Formation. Their study found an age of 2516 +/- 4 Ma. Altermann and Nelson (1998) further interpret the ash bed they dated in the Griqualand West basin to be the same ash bed that Sumner and Bowring (1996) dated in the Transvaal basin. This allows the two basins to be correlated at the uppermost portion of the Campbellrand subgroup and allows an estimate of 2500 Ma to be made for the onset of banded iron formation deposition.

The stratigraphy of the Kaapvaal craton of South Africa contains black shale deposits, banded iron formations and an increase in magmatism near 2.5 Ga. In addition, the deposition in the Transvaal basin of South Africa represents a marine transgression (Simonson et al., 2000). The combined presence of these features may mean that geochemical evidence for a mantle plume event might also be preserved in the stratigraphy.

3.2 Kathu Borehole

The samples used in this study were taken from the Kathu borehole. The location of the Kathu borehole is marked on Figure 1. Samples are indicated in Figure 4 with their position in the stratigraphy of the Ghaap Plateau facies. In addition, the samples and their respective depth within the core are presented in Table 1. The Kathu borehole is a drill core that represents a 3 km thick continuous stratigraphic section through the carbonate platform in the Griqualand West basin (Altermann and Nelson, 1998; Altermann and Siegfried, 1997). Only the base of the Schmidtsdrif Subgroup and the top

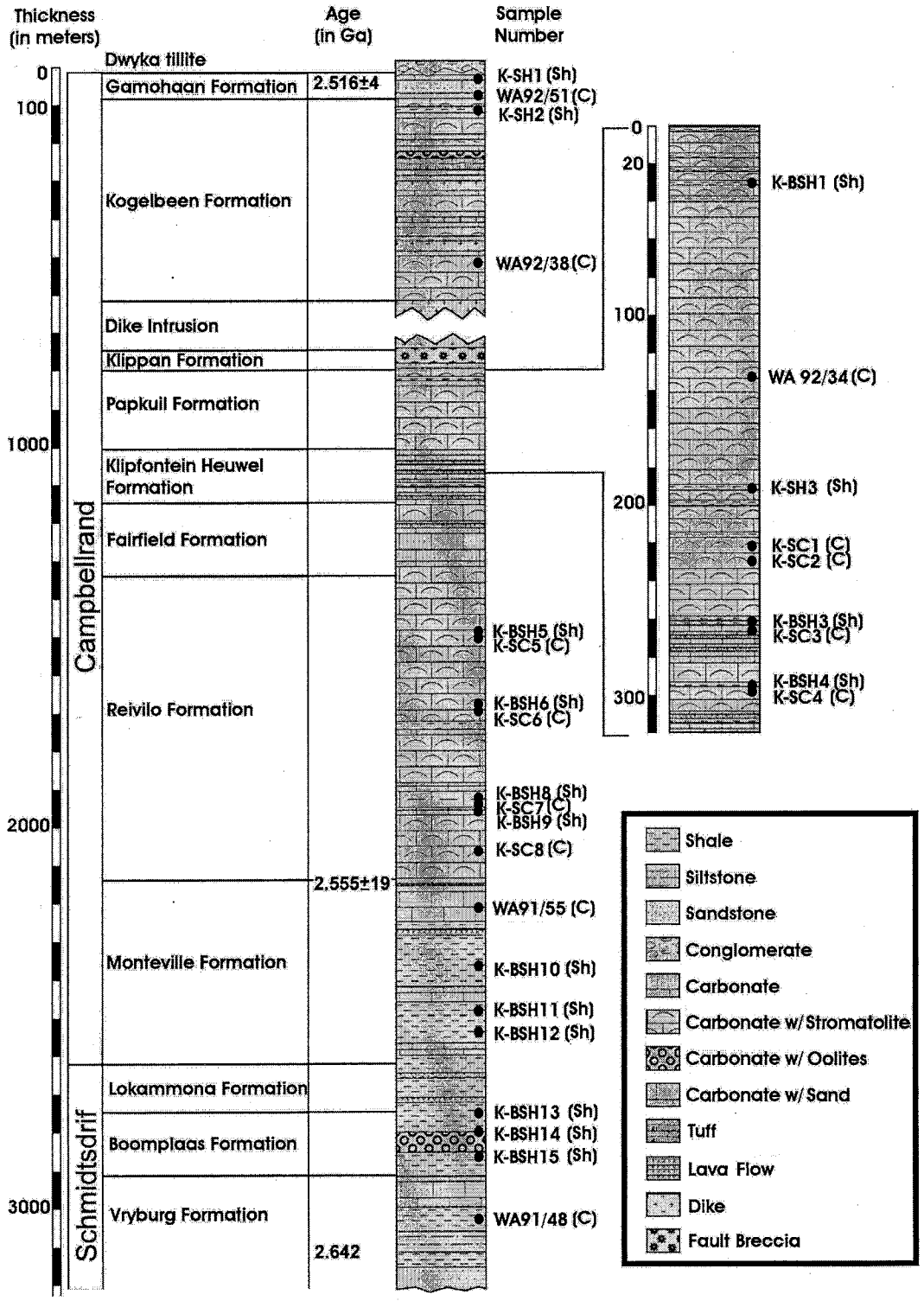

Figure 4: Stratigraphy of the Kathu Borehole (after Altermann and Nelson, 1998). Sample numbers marked with (C) at the end of the sample number are carbonate samples. Sample numbers marked with (Sh) are shale samples.

Table 1: Samples from the Kathu borehole and their depth with in the core. (The Paleozoic/Archean unconformity occurs at a depth of 326 feet in the Kathu borehole.)

Formation	Sample	Depth (meters)
Gamohaan Formation	KSh1	373
	KSh2	378
	WA 92/51	382
Kogelbeen Formation	WA 92/38	832
Papkuil Formation	KBSh1	1239
	WA 92/34	1355
	KSh3	1423
	KSC1	1444
	KSC2	1447
Klipfontein Heuwel Formation	KBSh3	1475
	KSC3	1477
	KBSh4	1500
	KSC4	1501
Reivilo Formation	KBSh5	1930
	KSC5	1931
	KSC6	2193
	KBSh6	2206
	KSC7	2453
	KBSh8	2469
	KSC8	2545
Monteville Formation	WA 91/55	2685
	KBSh10	2895
	KBSh11	2960
	KBSh12	3015
Boomplaas Formation	KBSh13	3239
	KBSh14	3286
	KBSh15	3360
Vryburg Formation	WA 91/48	3585

of the Cambellrand Subgroup are not exposed. The core was drilled North of the Griquatown fault, where a geophysical anomaly is observed. At the time, speculation regarding the geophysical anomaly was that it represented a crystallized mafic intrusion. Examination of the core shows no evidence supporting a large mafic intrusion at this site. The core is now kept at the Geological Survey of South Africa in Upington. The Vryburg Formation is the stratigraphic unit at the base of the Kathu borehole. A zircon found in a volcanic ash layer within the Vryburg Formation was dated at 2642 Ma (pers. comm., W. Altermann, 2002). Using conventional zircon age dating using a several zircons, Altermann and Nelson (1998) obtained two additional ages for ash beds found within the carbonate shelf. A date for an ash bed at the top of the Monteville Formation is dated at 2555 +/- 19 Ma. The second age corresponds to an ash bed in the Gamohaan Formation, which represents the top of the Cambellrand Subgroup found in the Kathu borehole. This age is 2516 +/- 4 Ma. The three zircon dates reported by Altermann and Nelson (1998) provide the upper and lower limits of the deposition of the carbonate shelf in the Kathu borehole. The ash beds also allow the stratigraphy in the Kathu borehole to be correlated with the Prieska facies of the Griqualand West basin and the Transvaal facies of the Transvaal basin.

3.3 Sampling Strategy

In order to determine the chemostratigraphy of the Griqualand West basin, samples were taken at intervals through the Schmidtsdrif and Cambellrand Subgroups. An attempt was made to have an even distribution of samples throughout the section. However, as the Kathu borehole is over 3000 m long and there is a charge for each box accessed, it was necessary to choose suitable sections of the core for sampling in

advance. In order to choose suitable sampling sites, the stratigraphy of the Kathu borehole published by Altermann and Siegfried (1997) was analyzed. The first regions selected were areas of the core where carbonates and black shales are interbedded. These sites were selected in order to get samples of organic and carbonate carbon that were deposited at approximately the same time. However, as the shales are not always interbedded with carbonates, several carbonate and shale samples were chosen independently of the other rock type. Sampling sites were selected from areas in the core that Altermann and Siegfried (1997) indicate are undeformed and unmetamorphosed. In addition, Wlady Altermann provided several samples in an attempt to provide as much coverage of the core as possible. These sample numbers are identified with "WA" followed by a number in Figure 4. Not all of the sample sites selected, nor all of the samples provided by Altermann are suitable for geochemical analysis. Several of these samples show veining indicating post-diagenetic fluid flow and some are partially silicified. These samples were not analyzed. In addition, to avoid the possibility of selecting samples with hydrothermal alteration, no samples were selected near igneous intrusions or near faults or areas of deformation. Because of these problems, it has not been possible to obtain representative samples from the entire borehole.

In order to effectively sample the geochemical event, it is important to estimate the extent of the geochemical changes. Carbon isotopic changes that may be associated with a mantle plume event are short-lived events. Valladares et al. (1996) report a positive $\delta^{13}C_{carb}$ excursion in carbonates of the Iberian peninsula that were deposited during the upper Cenomanian age of the Cretaceous period. The entire excursion, including both the increasing and decreasing $\delta^{13}C_{carb}$ values surrounding the peak, occurs

in a section of the stratigraphy that is less than 50 m thick. Davis (1998) reports a positive $\delta^{13}C_{org}$ excursion also from the Cenomanian age deposits. This excursion is recorded in a section of the stratigraphy that is less than 25 m thick. Since both excursions are completely contained within the Cenomanian deposits, they occurred within a maximum of a 5 million year interval. Therefore, in order to effectively sample the Griqualand West basin, samples should be obtained within 5 million years of the onset of the mantle plume event if it is to be observed geochemically. It is difficult to obtain unaltered samples from the top of the Gamohaan formation from outcrops. Likewise, it is difficult to obtain samples of this age in the Kathu borehole because the upper portion of the Gamohaan formation has been eroded in this section. However, based on estimates of the thickness of the Gamohaan formation, less than 30 meters was eroded between the Paleozoic/Archean unconformity and what was the base of the Kuruman banded iron formation. Futhermore, Isley and Abbot (1999) estimate that deposition of banded iron formations may lag 1 to 3 million years behind the onset of the mantle plume event. Therefore, geochemical changes may be observed in the top portion of the Gamohaan formation exposed in the Kathu borehole.

4 Methods

4.1 Carbonates

4.1.1 Petrography

Thin sections of the carbonate samples were examined using plane polarized (ppl) and cross- polarized (xpl) light. Thin sections were also examined under reflected light using the white card method (Folk, 1987) in order to assess the organic content of the carbonate. Cathodoluminescence was used to study the diagenesis of the samples. Cathodoluminescence was performed on a ELM-3R Luminiscope at vacuums of approximately 130 millitorr with voltages between 10-15 kV. The beam focus was between 25-50%.

4.1.2 Carbon and Oxygen Isotopes

Approximately 15-30 mg of crushed whole rock carbonate sample was digested with phosphoric acid (H_3PO_4) at 50°C for 4 hours to produce CO_2. Isotopic analysis of the CO_2 was performed on a duel inlet gas source magnetic sector isotope ratio mass spectrometer using PDB as the standard. In addition, Solenhofen standard was run with each batch of samples to determine the acid fractionation factor for oxygen isotopes. This corrects for the oxygen lost to water during the reaction of carbonate and acid to form CO_2.

4.1.3 Trace Metals

Carbonates were analyzed for several trace metals including Li, B, Ti, V, Cr, Co, Ni, Cu, and Zn. Approximately 0.2-0.3 mg of crushed carbonate sample was digested with nitric acid (HNO_3) and reverse osmosis water (RO H_20) in a Milestone Ethos

microwave. The samples were than filtered and diluted with RO H_20, before running on an Agilent 7500i inductively coupled plasma injected mass spectrometer (ICP-MS).

4.2 Shales

4.2.1 Carbon Isotopes

Initially, organic carbon was separated from the shale samples using the following procedure. Crushed shale samples were digested in cold followed by hot hydrochloric acid (HCl). The resultant solids were centrifuged and washed with distilled water, before reacting with hydrofluoric acid (HF) for 16 hours. After reacting, the resultant solids are washed and centrifuged again and an acidic zinc bromide solution is added. The solids are dried and then analyzed on a Delta^{Plus}XL mass spectrometer for their carbon isotopic values. Separation of organic solids was performed by Geochem Laboratories, Inc. Isotopic analysis was completed at University of New Mexico.

4.2.2 Sulfur Isotopes

Sulfur was extracted from the shale samples using the following procedure. Crushed shale samples were reacted using a Cr-reduction technique to form H_2S that was captured in Zn acetate solution as ZnS. After decanting the Zn acetate solution and rinsing the ZnS three times with millipore water, the ZnS was converted to Ag_2S by reaction with $AgNO_3$. The Ag_2S was centrifuged and the $AgNO_3$ solution decanted. The $AgNO_3$ was then dried in an 80°C oven. Once dry, the resultant solid was analyzed on a Micromass Isoprime mass spectrometer for its isotopic values. The entire procedure was performed at the University of Maryland, College Park.

5 Results

5.1 Petrography and Cathodoluminescence of Carbonates

Thin sections were obtained for 11 of the carbonate samples. Based on petrographic characteristics, the carbonates can be divided into 2 groups (Table 2). Group I carbonates are composed of microcrystalline dolomite with primary fabrics at least partially preserved after dolomitization (Figure 5). In contrast, Group II carbonates have macrocrystalline dolomite that have very little preserved primary depositional fabric (Figure 6). The dolomite in these samples largely or completely disrupts primary fabrics. Groups I and II carbonate have little to no clastic contribution.

When observed using cathodoluminescence, both Groups I and II carbonates show at least two generations of dolomite. The first generation is characterized by bright red luminescent dolomite rhombs, while the second generation forms a deep red luminescent matrix surrounding the first generation (Figure 7). The change in the luminescent color implies a change in the water composition during dolomitization (Machel et al., 1991). Increasing concentrations of manganese (Mn) increases the luminescence from black and brown to bright red. On the other hand, increasing concentrations of Fe, Co, and Ni decreases the luminescence from bright red to black or brown. Therefore, changes in the luminescent color indicates a change in the concentration or the ratio between minor and trace metals in a carbonate. In addition, to changes in the luminescence between the two dolomite phases, samples that contain vugs and/or veins show zonation of the dolomite composition under cathodoluminescence.

Table 2: Petrographic classification of carbonates from the Griqualand West basin

Group	Sample Number	Description
Group I	WA 92/51, WA 92/38, KSC5, KSC8, WA 91/55	microcrystalline dolomite; primary fabrics preserved
Group II	WA 92/34, KSC1, KSC2, KSC3, KSC7	macrocrystalline dolomite; primary fabrics partially or completely obscured

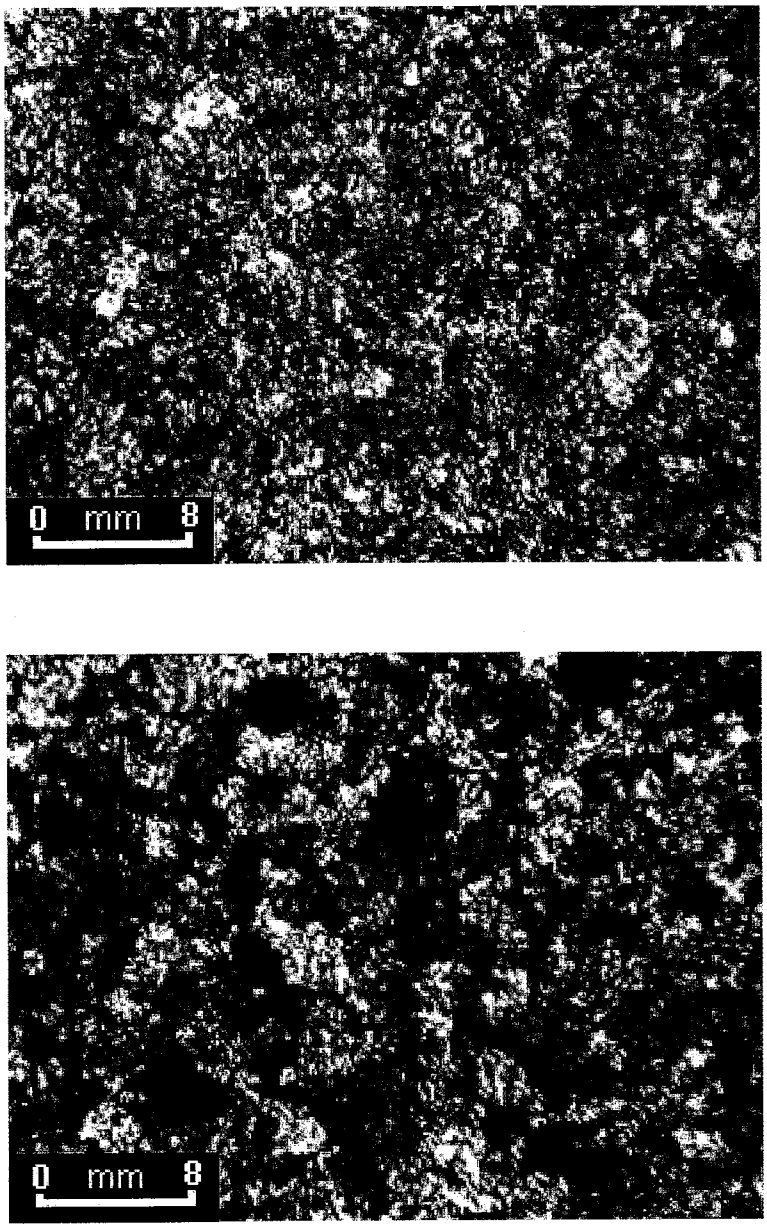

Figure 5: Photomicrographs of carbonate sample KSC1 (Group II) in plane polarized light (upper image) and cross-polarized light (lower image). Both images show microcrystalline dolomite rhombs and the original fabric of the rock.

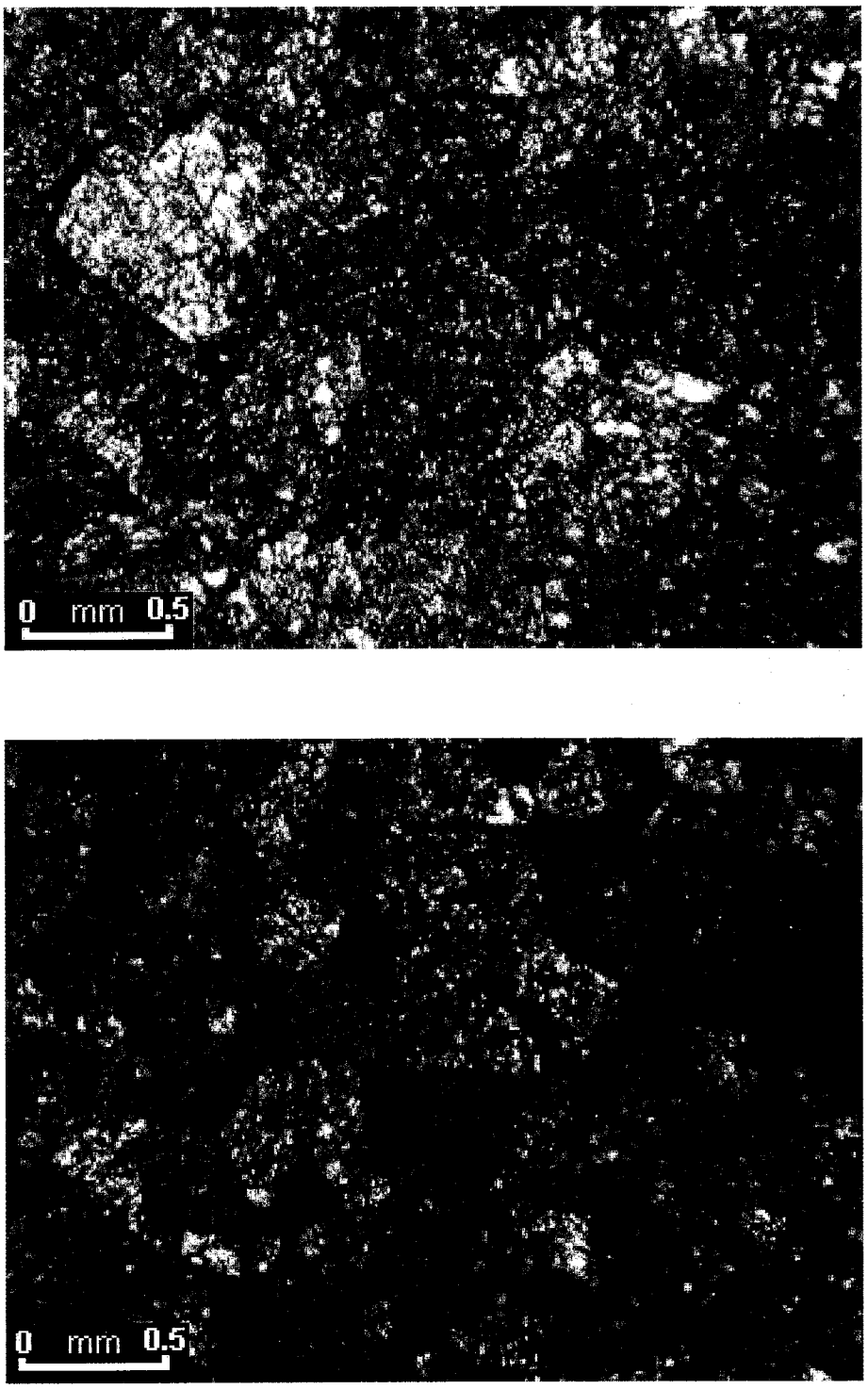

Figure 6: Photomicrographs of carbonate sample WA 92/34 (Group I) in plane polarized light (upper image) and cross polarized light (lower image). Both images show macrocrystalline dolomite and no original fabric.

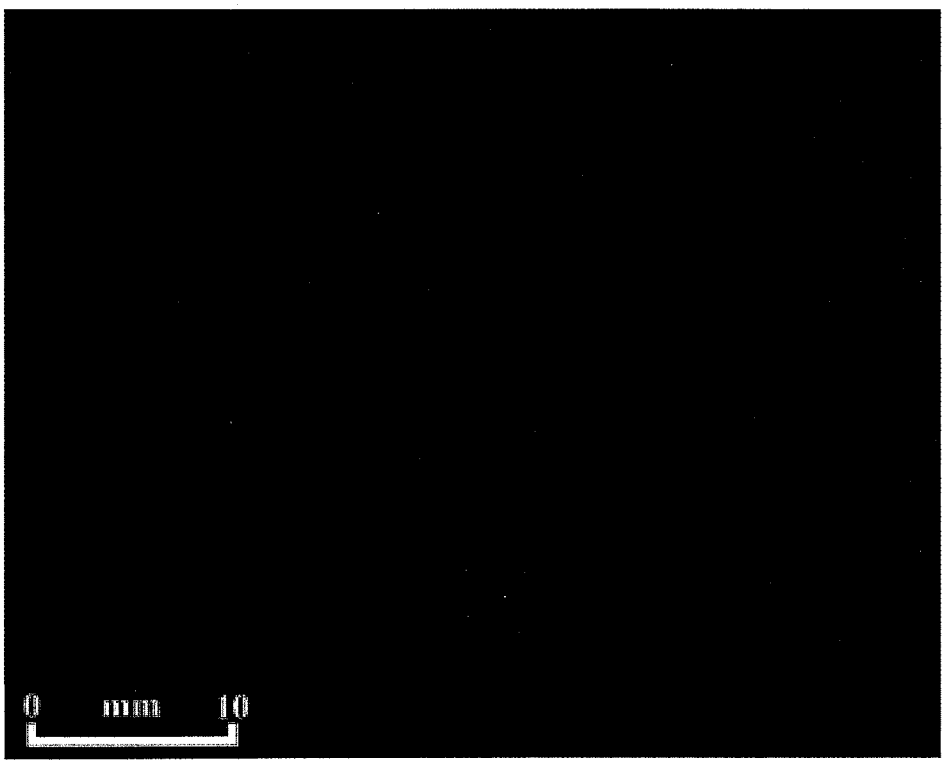

Figure 7: Photomicrograph of sample KSC5 under cathodoluminescence.

5.2 Petrography and Cathodoluminescence of Sandstones

A sandstone with carbonate cement (WA 91/48) contains clasts of quartz, feldspar, and igneous rock fragments. It has a poikilotopic carbonate cement that surrounds the sedimentary clasts and the cement shows zonation around several of the clasts when viewed in cross-polarized light. The cement contains twins and deformation bands, but it does not luminesce under cathodoluminescence. The carbonate twins indicate that the rock was subjected to high pressures (Nesse, 1986). However, none of the rocks used in this study shows any evidence of metamorphism such as ductile deformation or crystallization of minerals such as talc, tremolite, or diopside.

5.3 Carbonates

5.3.1 Carbon and Oxygen Isotopes

The results of $\delta^{13}C_{carb}$ and $\delta^{18}O$ analysis of the carbonate samples are presented in Table 3. All of the carbonate samples have $\delta^{13}C_{carb}$ values between –1 and 0‰ (PDB) and there is no systematic variation in the $\delta^{13}C_{carb}$ values with stratigraphic height (Figure 8). The $\delta^{18}O$ values of the carbonates vary between 28 and 34‰ (SMOW). Again there is no systematic variation in $\delta^{18}O$ values of the carbonates with stratigraphic height. There is no consistent trend in $\delta^{13}C_{carb}$ between Groups I and II carbonates. However, Group I carbonates have lower $\delta^{18}O$ values than Group II (Figure 9). The one exception is KSC5, a Group I carbonate, which has a $\delta^{18}O$ that is similar to Group II carbonates.

Table 3: Carbon and oxygen isotopes and trace element concentrations in carbonate samples from the Griqualand West basin. δ13C values are reported in parts per mil with respect to PDB. δ18O values are reported in parts per mil with respect to SMOW. Trace element concentrations are in parts per million (ppm).

Formation	Sample	$\delta^{13}C_{carb}$	$\delta^{18}O$	Li		B		Ti		V		Cr		Co		Ni		Cu		Zn	
				Conc	Std Dev	Conc	Std Dev	Conc	Std Dev	Conc	Std Dev	Conc	Std Dev	Conc	Std Dev	Conc	Std Dev	Conc	Std Dev	Conc	Std Dev
Gamohaan	WA 92/51	-0.1	17.4	**2.4**	2.98	**2.4**	1.25	**5.1**	3.68	**1.8**	2.44	**2.4**	1.95	**0.7**	3.89	**3.9**	2.94	**7.8**	0.59	**6.1**	1.08
	WA 92/38	-0.6	19.1	--	--	--	--	--	--	--	--	--	--	--	--	--	--	--	--	--	--
Papkuil	WA 92/34	-0.1	21.7	**2.8**	3.64	**2.8**	4.57	**3.4**	2.39	**1.3**	2.87	**3.7**	2.07	**0.3**	1.19	**2.8**	1.53	**9.1**	0.33	**22**	0.63
	WA 92/34	-0.1	21.7	**2.8**	2.53	**3.0**	1.04	**3.0**	4.82	**1.2**	5.13	**2.7**	0.54	**0.3**	1.89	**2.6**	3.7	**8.8**	0.76	**18**	1.5
	KSC1	-0.5	23.1	**1.5**	6.00	**6.0**	1.14	**7.4**	0.35	**2.3**	0.16	**3.0**	1.7	**0.8**	0.53	**3.4**	2.74	**5.6**	0.83	**4.6**	0.85
	KSC2	-0.7	22.3	**0.9**	2.56	**6.5**	0.82	**2.7**	0.91	**0.6**	7.3	**2.7**	0.81	**0.4**	2.94	**3.2**	0.35	**6.3**	0.41	**5.4**	0.92
	KSC3	-0.7	21.4	**0.5**	11.01	**2.4**	1.85	**1.6**	8.05	**0.0**	11.98	**0.3**	3.93	**0.3**	2.02	**2.1**	2.95	**8.6**	0.50	**4.0**	1.86
Reivilo	KSC5	-0.9	22.0	**1.0**	4.48	**3.0**	2.51	**3.0**	3.69	**0.1**	26.6	**0.3**	3.55	**0.4**	1.71	**2.7**	0.85	**8.9**	0.69	**5.2**	0.81
	KSC6	--	--	**2.1**	4.53	**4.7**	6.36	**5.1**	2.61	**0.7**	3.51	**0.5**	2.35	**0.4**	1.95	**2.5**	2.37	**9.3**	1.76	**4.0**	1.46
	KSC7	-0.8	21.7	**0.5**	5.34	**3.2**	1.29	**2.0**	3.96	**0.0**	48.56	**0.7**	2.79	**0.5**	1.41	**2.8**	1.61	**7.9**	0.72	**4.5**	1.11
	KSC8	-0.5	21.3	**0.7**	7.23	**2.8**	0.68	**3.9**	1.25	**1.1**	4.22	**1.8**	5.15	**0.4**	5.02	**4.1**	0.34	**7.7**	0.71	**2.9**	0.93
Monteville	WA 91/55	-0.9	19.4	**0.7**	3.58	**2.3**	5.42	**2.1**	4.18	**0.9**	5.94	**4.0**	1.62	**0.5**	3.68	**3.9**	1.35	**8.6**	1.55	**6.1**	1.64
	WA 91/55	-0.9	19.4	**0.4**	5.77	**1.8**	1.73	**2.7**	2.47	**1.3**	2.17	**4.8**	1.94	**0.5**	2.3	**4.7**	3.38	**6.9**	0.60	**6.3**	0.39
Vryburg	WA 91/48	-10.1	15.7	**5.2**	3.35	**11**	4.43	**41**	1.07	**8.5**	2.07	**26**	1.1	**42**	0.62	**63**	1.28	**140**	0.24	**18**	0.96
	WA 91/48	-10.7	15.2	**5.2**	3.35	**11**	4.43	**41**	1.07	**8.5**	2.07	**26**	1.1	**42**	0.62	**63**	1.28	**140**	0.24	**18**	0.96
	Standard	--	--	**0.8**	2.88	**6.1**	1.84	**10**	3.49	**2.5**	3.15	**2.9**	0.69	**0.3**	3.2	**3.1**	1.84	**11**	0.87	**30**	0.77
	Standard	--	--	**1.0**	2.93	**5.6**	0.96	**7.9**	2.01	**2.4**	3.58	**2.6**	1.26	**0.3**	1.78	**2.5**	1.55	**11**	0.88	**29**	0.15
	Standard - Expected	--	--					**0.0**				**2.3**		**1.0**							
Detection Limit		--	--	**1.46**		**0.67**		**2.02**		**0.11**		**.6**		**1.27**		**1.63**		**0.09**		**0.23**	

Note: Expected standard values are uncertified values.

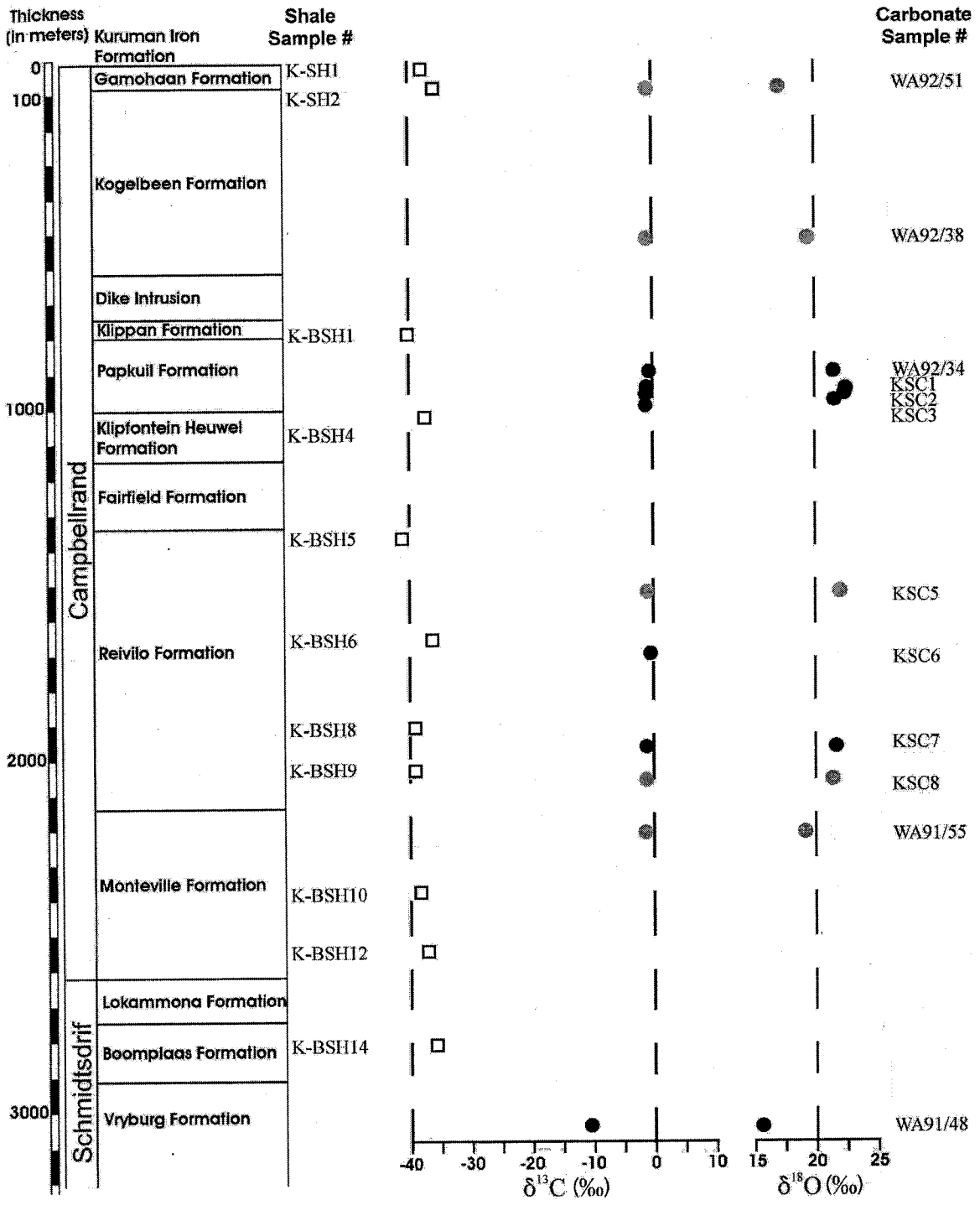

Figure 8: Stratigraphy of the Kathu borehole (After Altermann and Nelson, 1998) showing location of samples and carbon and oxygen isotopic results. Open squares represent the results for black shale samples. Grey circles represent the results for Group I carbonate samples while black represents the results for Group II carbonates. Vertical lines have been chosen arbitrarily.

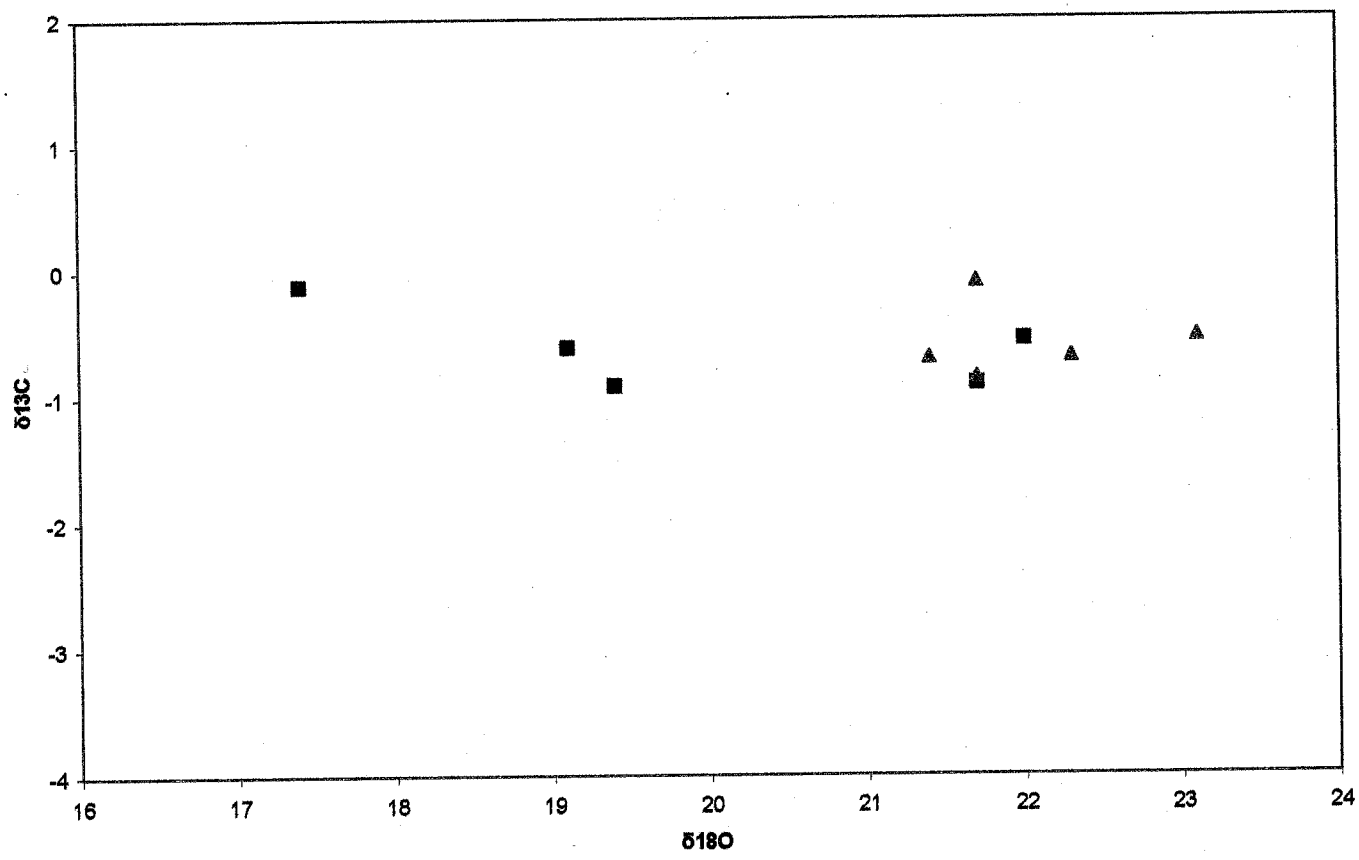

Figure 9: Plot of carbon vs. oxygen isotopes from the Griqualand West basin. Squares represent Group I carbonates and triangles represent Group II carbonates.

Although Sample WA 91/48 is a sandstone, it is included with the carbonate section because the carbonate cements were analyzed for carbon and oxygen isotopes. It has a $\delta^{13}C_{carb}$ value of –10.6‰, which is considerably lower than the carbonate values. Likewise, the $\delta^{18}O$ value for WA 91/48 is 16.15‰, which is isotopically lighter than the values obtained for the carbonates.

5.3.2 Trace Elements

Of the trace elements measured in the carbonates, only the elements listed in Table 3 are above the detection limit. Li, B, Ti, V, Cr, Co, Ni, and Cu range from 0 to 10 ppm for all the carbonate samples and most have standard deviations between 0 and 6. Li and V have notably high standard deviations for sample KSC3 (11.01 and 11.98 respectively.) In addition, V has a standard deviation of 48.56 for sample KSC7. However, this sample has concentrations below the detection limit of the ICP-MS. Concentrations of Zn range from 0 to 22 ppm with standard deviations between 0 and 2. (Instrumental standard analysis is presented in Appendix III.)

There is no systematic change in trace element concentration with stratigraphic height for any of the trace or major elements analyzed in this study (Figure 10). None of the trace elements occur in sufficient concentrations to identify differences between carbonate groups with any confidence. The carbonate cement of WA 91/48 has a higher concentration of Li, B, Ti, V, Cr, Co, Ni, and Cu than the carbonate rocks.

Trace metal ratios, Co/Ni, Cr/Ni, and Cu/Zn, are graphed as a function of stratigraphic height for carbonate samples (Figure 11, Table 4). There is little variation in the Co/Ni ratio with all samples having a ratio between 0.1 and 0.2 with the exception of sample WA 91/48, which is 0.7. Cr/Ni values vary from 0.1 to 1.1. Likewise, Cu/Zn

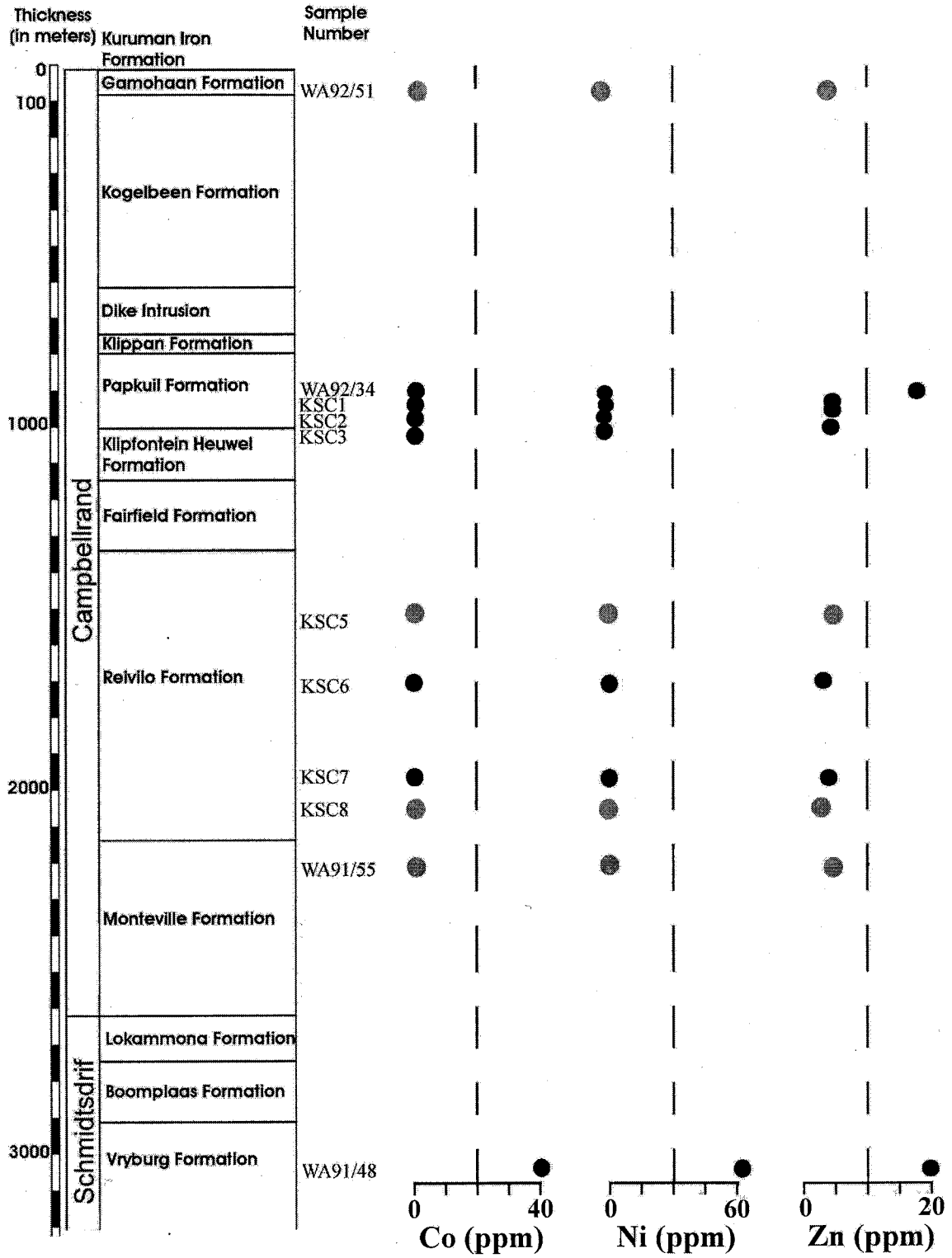

Figure 10: Graph of trace metal concentration in carbonate samples with respect to stratigraphic height. Grey circles represent the results for Group I carbonate samples while black circles represent the results for Group II carbonates. Vertical lines are arbitrary.

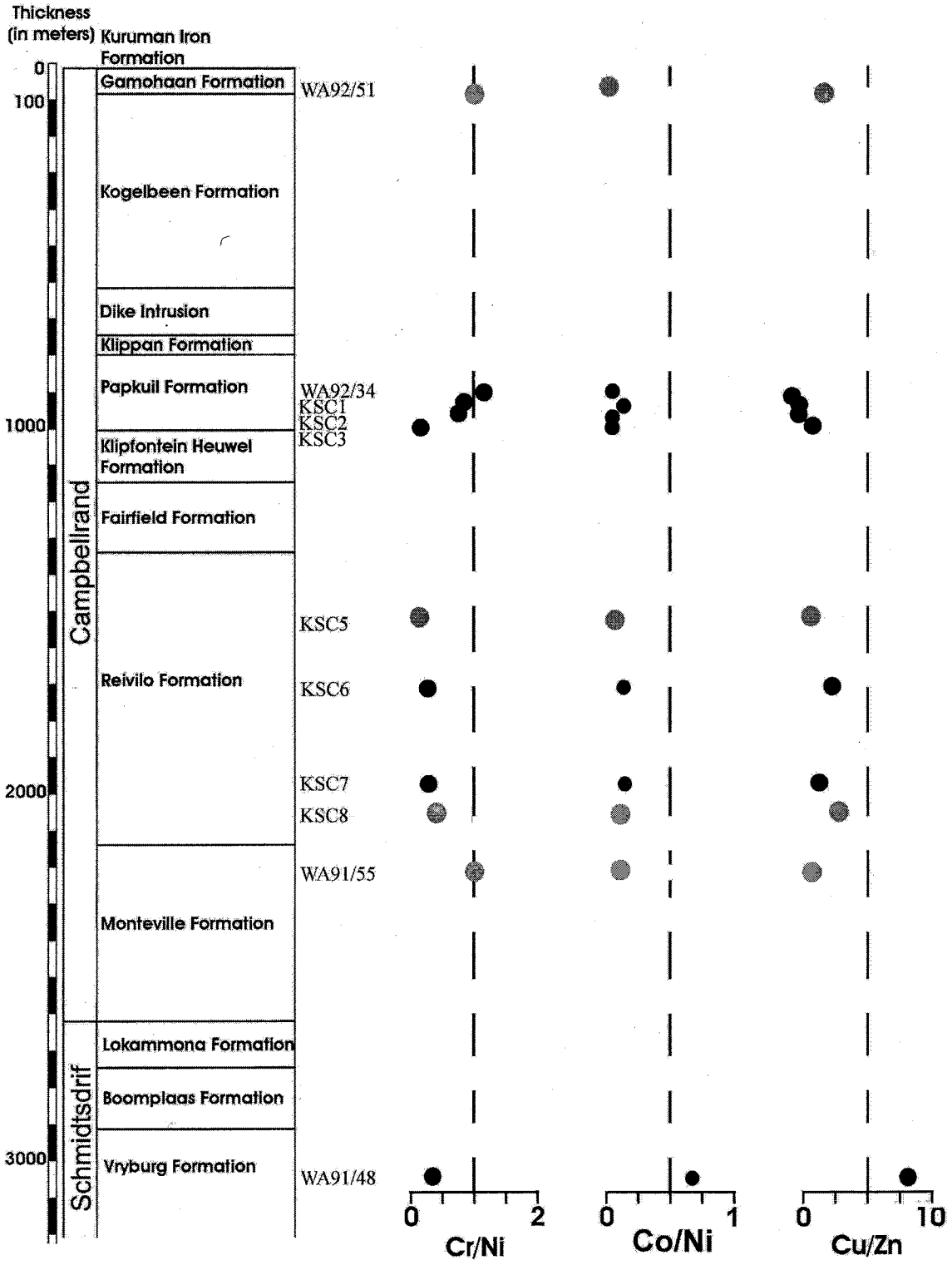

Figure 11: Selected ratios of trace metals with respect to stratigraphic height. Grey circles represent the results for Group I carbonate samples while black circles represent the results for Group II carbonates. Vertical lines are arbitrary.

Table 4: Trace element ratios for carbonate samples.

Formation	Sample	Co/Ni	Cr/Ni	Cu/Zn
Gamohaan	WA 92/51	0.2	0.6	1.3
Papkuil	WA 92/34	0.1	1.1	0.5
	KSC1	0.2	0.9	1.2
	KSC2	0.1	0.8	1.2
	KSC3	0.1	0.1	2.1
Reivilo	KSC5	0.1	0.1	1.7
	KSC6	0.2	0.2	2.3
	KSC7	0.2	0.3	1.8
	KSC8	0.1	0.4	2.8
Monteville	WA 91/55	0.1	1	1.4
Vryburg	WA 91/48	0.7	0.4	8.6

values fall between 0.5 and 2.8 with the exception of WA 91/48 at 8.1. None of the ratios shows systematic variation with stratigraphic height.

5.4 Shales

5.4.1 Carbon Isotopes

Many of the shales from the Griqualand West basin have both organic and carbonate carbon components. Initially, all the samples were analyzed for organic carbon without having separated the organic and carbonate carbon components. Consequently, some of the initial results for $\delta^{13}C_{org}$ reflect a $\delta^{13}C_{carb}$ component. For the final analyses, several samples were selected for organic carbon separation and were analyzed for their organic carbon isotopic values. The $\delta^{13}C_{org}$ of the organic fractions of the shales are presented in Table 5. The total range in $\delta^{13}C_{org}$ for the organic carbon in the shales is from –41 to –34.4‰. There is no apparent correlation between the $\delta^{13}C_{org}$ of the shales and stratigraphic height (Figure 12).

5.4.2 Sulfur Isotopes

Many previous attempts to analyze sulfur isotopes from shales in the Transvaal basin report the sulfur concentration to be below detection limit of the mass spectrometers used (Watanabe et al., 1997). This study used a recently developed process to extract and concentrate the sulfur from shale samples (see Appendix I for sulfur preparation procedures). This method allows isotopic values of sulfur to be reported that may have been below the detection limit of other methods. The $\delta^{34}S$ for shales in this study range from –2.93 to 14.44‰ (Table 5). As with $\delta^{13}C_{org}$, there is no relationship between $\delta^{34}S$ in the shales and stratigraphic height (Figure 12).

Table 5: Carbon and sulfur isotopes in shale samples from the Griqualand West basin. Both carbon and sulfur values are in parts per mil with respect to PDB.

Formation	Sample	$\delta^{13}C_{org}$	$\delta^{34}S$
Gamohaan Formation	KSh1	-37.3	-2.93
	KSh2	-34.4	10.19
Papkuil Formation	KBSh1	-40.2	1.12
	KBSh16	--	1.72
Klipfontein Heuwel Formation	KBSh4	-37.6	0.04
Reivilo Formation	KBSh5	-41	13.46
	KBSh6	--	3.03
	KBSh8	-39.4	5.9
	KBSh9	--	-2.3
Monteville Formation	KBSh10	-38.33	7.67
	KBSh11	--	7.76
	KBSh12	-36.5	14.44
Boomplaas Formation	KBSh13	--	-1.96
	KBSh14	-35	1.67
	KBSh15	--	1.38

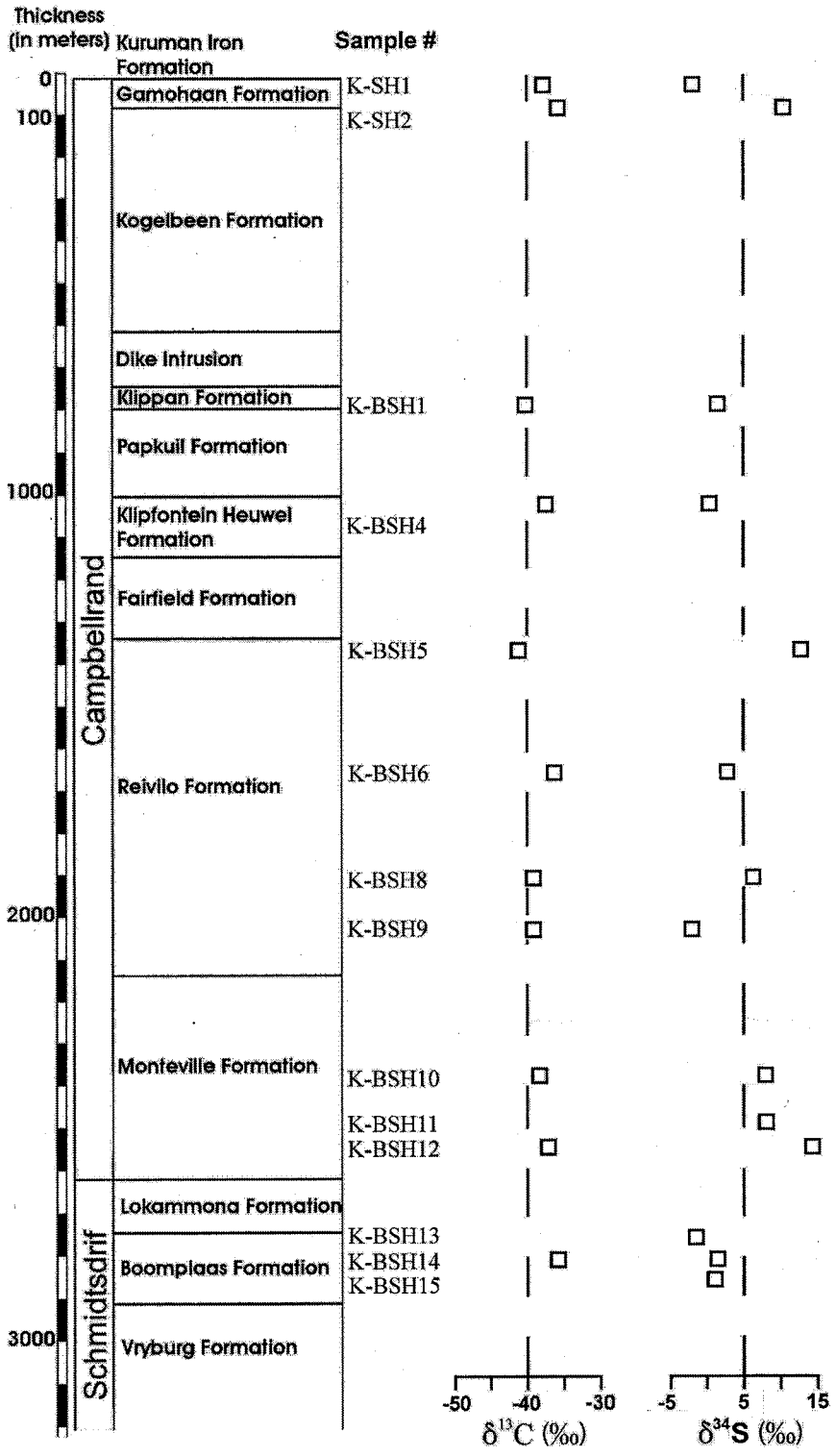

Figure 12: Carbon and sulfur isotopes in black shale deposits of the Griqualand West basin. Vertical lines are arbitrary.

6 Discussion

There are two possible models for dolomitization. The seepage-reflux model relies upon evaporation in a shallow basin to concentrate the Mg in a fluid (Tucker, 2001). Evaporation increases the density of the overlying water and causes the surface water to be cycled down through the carbonate deposits where it can precipitate the Mg as dolomite. Dolomites believed to form by the seepage-reflux model are often associated with evaporites but there is no evidence of evaporite deposition in the Kaapvaal craton carbonate deposits between 2.65 and 2.5 Ga. The second model is the ocean current/tidal pumping model. In this model, large volumes of seawater are cycled through the carbonate platform through the geothermal gradient within the carbonate platform. This means the first stages of dolomitization occurred in waters of a chemical composition similar to the depositional waters of the limestone precursor.

The dolomitization of Groups I and II carbonates resulted in different degrees of fabric disruption. This is possibly due to the burial depth at which dolomitization occurred. Low-Mg calcite is more stable then high-Mg calcite, therefore the longer a limestone is buried, the more likely it will stabilize to low-Mg calcite prior to dolomitization (Tucker, 2001). In addition, high-Mg calcite is less resistant to dolomitization than low-Mg calcite and therefore is more likely to retain its primary fabrics during dolomitization. Because Group I carbonates have microcrystalline dolomite and preserved primary fabric (Figure 6), this may indicate that dolomitization began soon after deposition. On the other hand, Group II carbonates retain little of their primary fabric and have macrocrystalline dolomite rhombs (Figure 5). The disruption of the primary fabric may indicate that the calcite recrystallized to low-Mg calcite prior to dolomitization and was therefore buried for an extended period of time prior to

dolomitization. Another possibility is that Group II dolomites initially began dolomitization at shallow depths but a second generation of dolomitization occurred as a later stage, which proceeded to obscure the primary fabric.

If constant production of carbonate on the shelf is assumed, the length of time in which the calcite was buried can be directly correlated to the depth of burial. Therefore, limestone precursors of Group II carbonates underwent at least part of their dolomitization at a greater depth than Group I carbonates. Altermann and Nelson (1998) calculated the sedimentation rates of rocks in the Kathu borehole and observed three minor transgression/regression cycles. These transgressions and regressions may reflect changes in the sedimentation rate on the carbonate shelf, which would have affected the dolomitization depth of the carbonates. However, the correlation between the transgressive and regressive episodes discussed by Altermann and Nelson (1998) and the dolomitization pattern of the carbonates in this study is not clear.

Although thin section analysis of the carbonates would seem to indicate that the dolomitization of Groups I and II carbonates can be distinguished by a depth, the oxygen isotopes are not necessarily consistent with this interpretation (Figure 9). If temperature and water compositions are the two major controls on oxygen isotopic fractionation, Group II carbonates would be expected to be isotopically lighter than Group I carbonates. This is because temperature increases with depth, which causes fractionation to decrease. Based on known fractionation of between water and carbonates, the depositional water of carbonates tends to be isotopically lighter than the carbonates. Therefore, if fractionation between the water and the carbonate undergoing dolomitization decreases, the dolomite

would be expected to get isotopically lighter with increasing depth of dolomitization, not heavier as is the case with the Griqualand West carbonates.

Lee and Bethke (1996) modeled carbon and oxygen isotopes during dolomitization under a variety of conditions. They determined that the CO_2 fugacity of the dolomitizing water has a strong effect on the isotopic composition of the dolomite. As fugacity increases, the isotopic composition of the dolomite is increasingly influenced by the isotopic composition of the dolomitizing fluid. Therefore, if the dolomitizing water is the same isotopic composition of the limestone depositional water, dolomites formed in waters with high CO_2 fugacity will become isotopically lighter. However, at low fugacities, the original composition of the calcite becomes more important and the dolomite will become correspondingly heavier as it reflects the heavier isotopic signature of the calcite. Therefore, a change in CO_2 fugacity in the dolomitizing water may explain the discrepancy between the oxygen isotopes of the Groups I and II carbonates.

Both Groups I and II carbonates lack significant clastic contamination. Although this is a common characteristic of carbonates deposited in the Griqualand West basin and has been discussed by several authors, the exact cause of the absence of clastic material is not known (Altermann and Nelson, 1998).

One of the primary questions is whether the samples analyzed in this study are reliable indicators of the original carbonate or if they reflect a post-depositional diagenetic processes. The mobility of carbon isotopes has been addressed by several studies that indicate carbon isotopes do not vary greatly during diagenesis (Veizer, 1983; Azmy et al., 2001). Veizer (1983) noted that a low water/rock ratio during dolomitization of stromatolitic carbonates leads to very little carbon exchange during

diagenesis. Additional evidence for the dolomitization having little effect on $\delta^{13}C_{carb}$ for the Griqualand West samples comes from comparison of the $\delta^{13}C_{carb}$ variability of the carbonates. There is no correlation between $\delta^{13}C_{carb}$ values and Groups I and II carbonates. If dolomitization has had a significant effect on $\delta^{13}C_{carb}$, it is reasonable to expect that Group I dolomites, which experienced dolomitization at shallow depths, would have different $\delta^{13}C_{carb}$ than Group II dolomites, which experienced initial dolomitization at greater depths and/or experienced more than one generation of dolomitization at greater depth than Group I carbonates. Likewise, if low CO_2 fugacity is responsible for the heavy $\delta^{18}O$ values for the Group II dolomites, this would indicate that both the carbon and oxygen isotopes are characteristic of the original carbonate and not the dolomitization fluids (Lee and Bethke, 1996).

$\delta^{13}C_{carb}$ values of Griqualand West carbonates show little variation. Figure 14 shows Groups I and II carbonates on a plot of $\delta^{13}C$ vs. $\delta^{18}O$. Although $\delta^{13}C_{carb}$ does not vary between the two groups, Group I carbonates tend to have lighter $\delta^{18}O$ values than Group II carbonates. One exception is sample KSC5, a Group I carbonate that has a $\delta^{18}O$ similar to the Group II carbonates. KSC5 has zones of mixed grain size and it is classified with Group I carbonates based on the proportion of microcrystalline to macrocrystalline dolomite. Although its appearance is predominantly fine grained, KSC5 has the isotopic signature of the macrocrystalline Group II carbonates.

Carbonate carbon isotope analyses are graphed as a function of stratigraphic height in Figure 8. Although the number of samples analyzed is low, of the samples analyzed there is no evidence for a $\delta^{13}C_{carb}$ excursion as the samples approach the top of the Gamohaan formation as expected at the onset of the mantle plume event at this time.

However, the $\delta^{13}C_{carb}$ values are consistent with $\delta^{13}C$ values obtained in unmetamorphosed carbonates of similar ages in the Transvaal basin (Strauss and Moore, 1992).

Major Late Archean carbonates were also deposited in the Hamersley basin of Western Australia at the same time as the carbonate deposition in the Griqualand West basin (Eriksson et al., 1999). Figure 13 is a plot of $\delta^{13}C_{carb}$ from the Griqualand West basin carbonates with stratigraphic height compared to the $\delta^{13}C_{carb}$ values of the Hamersley basin carbonates. Two interesting points can be made: 1) like the Griqualand West basin, the Hamersley basin carbonates lack any evidence for a carbonate carbon isotope excursion at 2.5 Ga (Lindsay and Brasier, 2002); and 2) the Hamersley basin carbonates are isotopically heavier than the Griqualand West basin carbonates.

The mean $\delta^{13}C_{carb}$ for samples taken from five separate cores within the Hamersley basin representing ages between 2.7 and 2.5 Ga range from 0.03 to 0.73‰ (Lindsay and Brasier, 2002). There are three possible explanations for the differences in $\delta^{13}C_{carb}$ between the Hamersley and the Griqualand West carbonates.

First, it is possible that the different compositions reflect contamination by organic carbon. Organic carbon that is preserved in the sedimentary record is isotopically lighter than carbonate carbon (Kump and Arthur, 1999). For example, modern day carbonate carbon values are approximately 1‰, while modern organic carbon values are approximately -29‰. A small amount of organic matter could conceivably contaminate a carbonate sample and cause the resultant isotopic values to become lighter. Since the Griqualand West basin carbonates from this study are lighter than the temporal

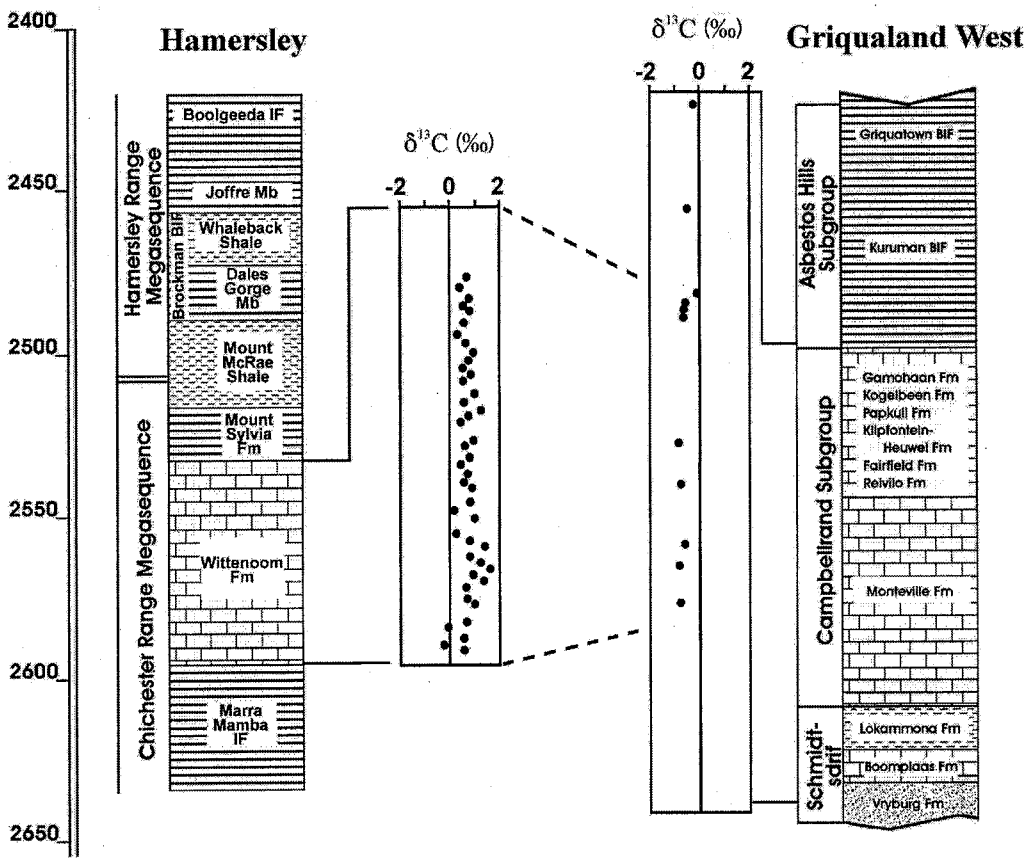

Figure 13: Stratigraphy and carbon isotopic data from the Hamersley basin compared with the stratigraphy and carbon isotopic data from the Griqualand West basin (after Eriksson et al., 1999 and Lindsay et al., 2002).

counterparts in the Hamersley basin, the Griqualand West basin samples could possibly be contaminated with organic carbon. However, the analytical procedure used in this study (see Appendix 1) does not use a strong acid to digest organic carbon and convert it to CO_2. Therefore, any organic carbon that may have been in the original rock, is not analyzed as CO_2 with the carbonate carbon.

A second possibility that might explain the geochemical discrepancies between the Hamersley and the Griqualand West basin carbonates is different patterns of dolomitization. If diagenetic alteration occurred at different depths and/or under different compositions of water, it might be possible to alter the $\delta^{13}C_{carb}$ signatures of one or more of the basins so that they no longer reflect the same carbon isotope values. Since the carbon and oxygen isotopic signature of Griqualand West carbonates is likely the result of low CO_2 fugacity and therefore representative of the original calcite isotopic composition, the only way the Hamersley basin carbonates could become heavier during diagenesis would be if they were dolomitized in even lower fCO_2 water.

A third alternative is that the carbonates in the two basins were deposited in waters of different chemical composition. Although both basins were deposited under marine conditions, different environmental conditions can effect the composition of the water. One of these environmental considerations is river runoff, which may alter the isotopic chemistry of a basin through mixing of meteoric water that is isotopically different from surrounding marine water (Holmden et al., 1998). Holmden et al. (1998) suggested that the chemistry of semi-restricted basins is affected by meteoric contributions more strongly than unrestricted basins. They further give an example of lateral $\delta^{13}C_{carb}$ variations in the Paleozoic Mowhakian Sea that is related to mixing of

different water types within the basin. The authors also point out that the geometry of a basin can act as an environmental control on the chemistry of the water. Shallow basins can undergo large amounts of evaporation, leaving behind isotopically heavier $\delta^{18}O$ values in water. Likewise, shallow waters may undergo increased exchange between atmospheric CO_2 and bicarbonate dissolved in the water. This would lead to isotopically heavier $\delta^{13}C$ values for the water. Another possible source of deviation between the water chemistries of the two basins might be hydrothermal activity. Carbon values of hydrothermal systems vary but are, in general, isotopically lighter than marine water. If one of the basins was effected by a hydrothermal system, the $\delta^{13}C$ values of both the carbonate and organic carbon would be expected to get isotopically lighter. Thus, there may be an environmental control that explains the variation of $\delta^{13}C_{carb}$ values between the Hamersley basin and the Griqualand West basin.

The study performed by Holmden et al. (1998) was based on observed lateral variations with in the Paleozoic Mowhakian Sea. No such lateral variation has been observed on the Kaapvaal craton where $\delta^{13}C_{carb}$ for the Griqualand West carbonates are comparable to the values obtained in previous studies of the Transvaal basin (Strauss and Moore, 1992). Carbonates from the Hamersley basin show variation between sampling sites (Lindsay and Brasier, 2002). Lindsay et al. (2002) collected data from three drill cores through the Wittenoom Formation. The mean values of carbonates from these drill cores are 0.02, 0.22, and 0.03‰ with standard deviations of 0.41, 0.18, and 0.17 respectively. The authors also collected data from two drill cores in the Carawine dolomite, which is located northeast of the Wittenoom formation, and the mean values for these two drill cores are 0.06 and 0.73 ‰ and standard deviations of 0.56 and 0.32

respectively. Lindsay et al. (2002) also point out that the Carawine dolomite, which was deposited in a shallow marine environment, is depositionally distinct from the Wittenoom formation, which was deposited in deep water. This implies that the depositional environment may have controlled the isotopically heavy mean value for the carbonates in the Carawine dolomite. This also indicates that there is some lateral variation in the chemical composition of the water during deposition in the Hamersley basin, which may account for the variation in the Hamersley basin carbonates compared to the Griqualand West basin carbonates. If the Hamersley basin did, in fact, undergo chemical compositional changes caused by different depositional environments, this could explain the difference in the $\delta^{13}C_{carb}$ of carbonates between the two basins.

$\delta^{18}O$ values from dolomitized carbonate cement for the Carawine dolomite of the Hamersley basin range from –8.2 to –1.3‰ with respect to PDB (Winhusen, 2001). $\delta^{18}O$ values from the Wittenoom Formation, in the Hamersley basin are between –14 and –6 ‰ with respect to PDB (Lindsay and Brasier, 2002). This study reports the values of carbonates from the Griqualand West basin between 16 to 24‰ with respect to SMOW. This corresponds to values between –15 and -6‰ in PDB (Figure 8). If these two basins experienced deposition in water of the same chemical composition, it is clear that the carbonates in the Hamersley basin and the carbonates in the Griqualand West basin also underwent similar post-depositional diagenetic processes.

Like the $\delta^{13}C_{carb}$, the $\delta^{13}C_{org}$ for the Griqualand West shales show no evidence of a negative excursion as the samples approach 2.5 Ga (Figure 12). They are comparable to $\delta^{13}C_{org}$ for other shales from the Transvaal basin on the Kaapvaal craton. $\delta^{13}C_{org}$ values for relatively unaltered shales in the Transvaal basin range between –43 and -31‰

(Strauss and Beukes,1996; Strauss and Moore, 1992). Strauss and Beukes (1996) studied several shales from the Transvaal basin and concluded that thermal alteration due to metamorphism or diagenesis will cause shales to become isotopically heavier. This is most likely the result of mobilization of the lighter isotopes. Therefore, $\delta^{13}C_{org}$ values that are lighter than –31‰ are believed to be relatively unchanged during burial and diagenesis. Since the samples used in this study are between –41 and –34.4‰, they are unlikely to have been altered after burial and diagenesis, using the Strauss and Beukes (1996) model.

Although it is possible that there is significant variation in $\delta^{13}C$ in regions that were not sampled more extensively, of the samples analyzed neither the $\delta^{13}C_{carb}$ nor the $\delta^{13}C_{org}$ vary significantly with stratigraphic height. Figure 14 is a graph of $\delta^{13}C_{carb}$ of the carbonates and $\delta^{13}C_{org}$ of the shales versus depth in the Kathu borehole. Time can be directly correlated with depth, so the deepest strata are also the oldest strata. A model by Kump et al. (1999) suggests that during episodes of increased volcanism changes in atmospheric CO_2 are due to increased volcanic degassing. This, in turn, causes a shift in the fractionation between $\delta^{13}C_{carb}$ and $\delta^{13}C_{org}$ ($\Delta_{carb\text{-}org}$) values. These authors further predict that a negative $\delta^{13}C_{org}$ excursion unaccompanied by change in $\delta^{13}C_{carb}$ could indicate a major increase in volcanic activity. Figure 14 shows that neither $\delta^{13}C_{carb}$ nor $\delta^{13}C_{org}$ change systematically with depth in the Kathu borehole, although there is a suggestion of a slight decrease in the $\delta^{13}C_{org}$ values towards the top of the borehole. Kump et al. (1999) predict an excursion of approximately 2‰ should accompany the onset of a mantle plume event. Therefore, the borehole results suggest that there was not

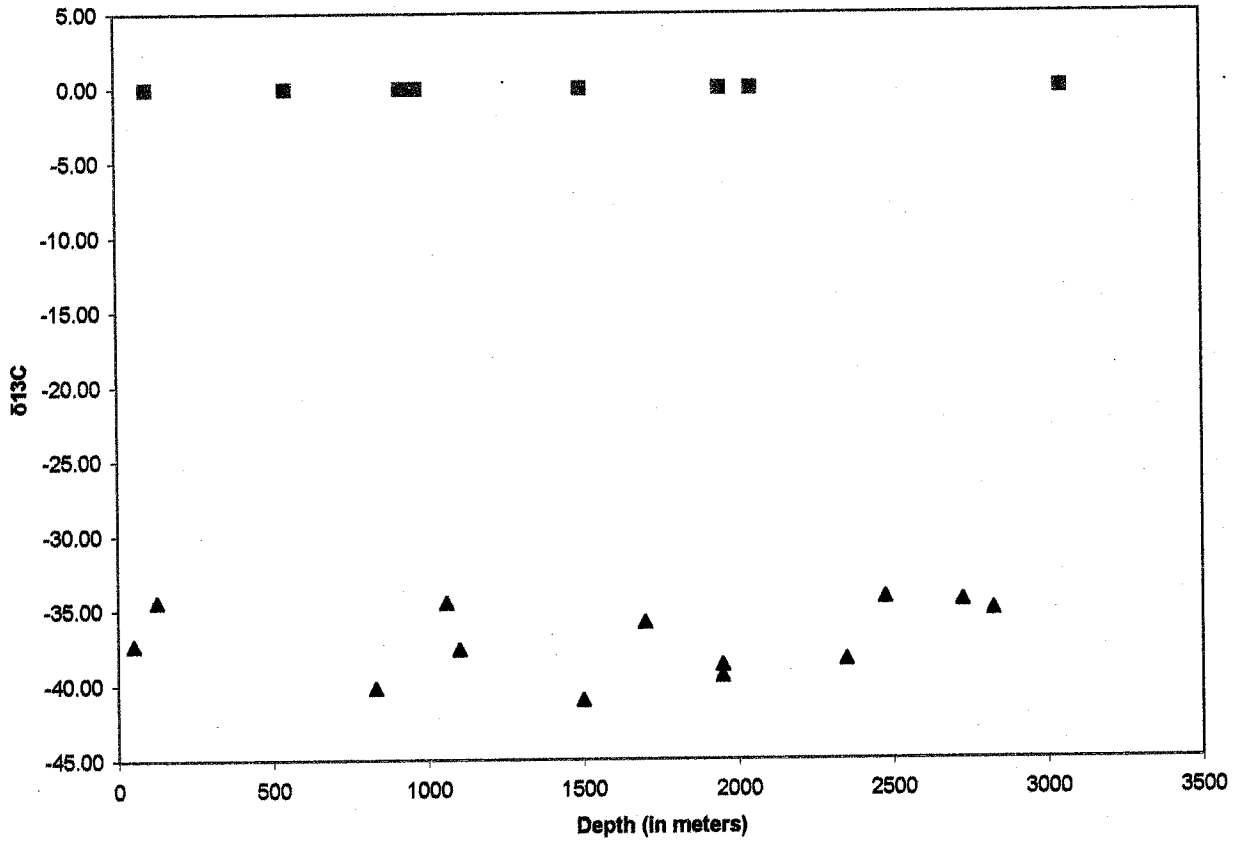

Figure 14: Graph of $\delta^{13}C$ for organic carbon from black shales (triangles) and $\delta^{13}C$ for carbonate carbon (squares) with depth in the Kathu borehole.

a significant change in the organic carbon burial rate between 2.65 and 2.5 Ga in the Griqualand West basin.

Very few data are available for sulfur isotopes in the Archean basins of the Kaapvaal Craton. Of previously reported sulfur isotope measurements from the Transvaal basin, $\delta^{34}S$ ranges from –1.3 to 23.6‰ in sedimentary pyrite (Strauss and Beukes, 1996). Strauss and Beukes (1996) note that $\delta^{34}S$ values do not appear to be facies dependent and attribute the variation to changes in the rate of bacterial sulfate reduction in the system. This is consistent with the results of this study, where the $\delta^{34}S$ ranges from –2.93 to 14.44‰ (Table 5). Meyer and Robb (1996) suggest that isotopically heavy $\delta^{34}S$ comes from hydrothermal sources while values that are isotopically light are controlled by bacterial sulfate reduction.

$\delta^{34}S$ is plotted with stratigraphic height in Figure 14. As with the data of Strauss and Beukes (1996), the $\delta^{34}S$ in the Griqualand West basin does not show a consistent change with stratigraphic height. In addition, there is no apparent correlation between $\delta^{34}S$ and $\delta^{13}C_{org}$ values (Figure 15). This may indicate one of two things. First, small changes in the isotopic composition of buried organic carbon do not have a clear relationship to changes in the $\delta^{34}S$. If sulfur isotopic variability is controlled solely by changes in bacterial sulfate reduction, then the sulfate reduction is not connected to the same bacterial control on organic carbon fractionation. A second possibility is that $\delta^{34}S$ is partially controlled by hydrothermal waters and that these waters did not have a comparable effect on the $\delta^{13}C_{org}$ of the shales. As an extension of this conclusion, since the trace metals found in the carbonates in which the shales are interbedded also do not

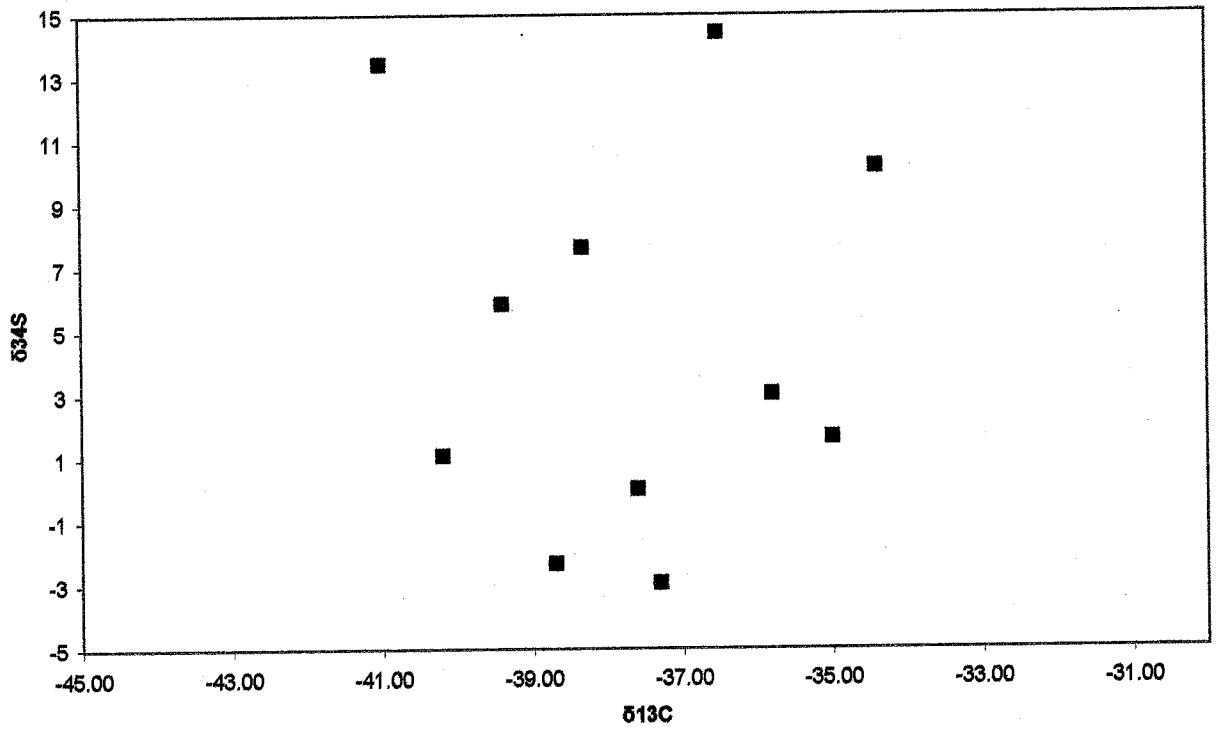

Figure 15: δ13C vs. δ34S for black shale samples from the Griqualand West basin.

show significant changes in trace metal concentrations, the carbonates are also relatively unaffected by the hydrothermal waters.

Figure 10 graphs selected trace metal concentrations with stratigraphic height. As with the $\delta^{13}C_{carb}$, there is a question of whether the trace metals can be mobilized during dolomitization and diagenesis. In an attempt to answer this question, several trace element ratios are presented in Table 4 and Figure 11. One of the goals is to determine if there is fractionation between elements of different mobility or between elements that are typically held in clastic components. Overall, there is very little deviation in the ratio of the trace elements with stratigraphic height. However, there is a drop in the Cr/Ni ratio between sample KSC1 and KSC2. However, because both Cr and Ni are near detection limits, this drop may result from analytical error. The relative mobility of trace metals in carbonates, not resulting from clastic contamination, is addressed in several studies, which indicate that most trace metals do not vary significantly during diagenesis in a closed system (Veizer, 1983; Brand and Veizer, 1980). Veizer (1983) showed that even in diagenetic events of differing water composition, the water/rock ratio is usually quite low and therefore the shift in trace metal concentration is minimal. Brand et al. (1980) conclude that the trace element concentration is adequate to determine the original concentration and the diagenetic history of a sample. An additional point that can be made from the data in Figure 11 is that there is no variation in trace metal concentration based on the characteristics that may be linked to dolomitization, such as the size of dolomite rhombs, presence or absence of primary fabrics, and $\delta^{18}O$ values. Therefore, it may be assumed that the depositional and diagenetic waters for the Griqualand West basin were relatively constant in their trace metal concentrations.

A major objective of this project is to see if there is evidence for a mantle plume event at 2.5 Ga reflected in geochemical changes with stratigraphic height in marine sedimentary rocks in the Griqualand West basin. At the onset of a possible mantle plume event at 2.5 Ga, several chemical changes in seawater are to be expected and these changes should be recorded in marine sedimentary deposits. The trace metals in marine carbonates are expected to increase in concentration with stratigraphic height as a reflection of increased metal flux from oceanic volcanic centers. In addition, $\delta^{34}S$ and $\delta^{13}C_{carb}$ are expected to show positive excursions. $\delta^{34}S$ is also expected to increase because reduced iron from oceanic volcanism preferentially incorporate ^{32}S to from pyrite (Derry and Jacobsen, 1990). Sulfate-reducing bacteria will increase around volcanic vents and these bacteria preferentially use ^{32}S as well. This decreases the ^{32}S available for incorporation in shale deposits. For $\delta^{13}C_{carb}$ the excursion is the result of increased burial of organic carbon, which preferentially incorporates ^{12}C and removes it from the system (Karhu, 1993; Condie et al. 2000, 2001). This means that carbonates incorporate anomalously heavy carbon. $\delta^{13}C_{org}$ is expected to show a negative excursion due to the increase in organic matter production caused by increased output of nutrients from volcanic vents. In fact none of these geochemical changes are observed. Furthermore, the composition of the sediments is surprisingly invariant for such an extended depositional interval.

There are three possible reasons for the lack of geochemical change in the Griqualand West section. First, it is possible that samples were not obtained close enough to the onset of a possible mantle plume event at 2.5 Ga. The top of the Kathu borehole is comprised of sedimentary rocks of the Gamohaan formation overlain by

glacial tillite, therefore the boundary between the Gamohaan formation and the Kuruman Iron Formation is not included in the section sampled. Furthermore, it was difficult to obtain suitable samples from outcrops due to faulting that obscures the stratigraphy. It is possible that a geochemical change might have occurred in the sequence of rocks that was eroded during the glacial period responsible for the tillite deposits. A second possibility is that samples were not obtained with a high enough frequency to obtain the see a change in the geochemistry of the rocks.

A third reason why there may not be a geochemical change in the rocks of the Griqualand West basin is that the there may be a delay in the onset of the changes in seawater composition after the onset of mantle plume activity. Jahren (2002) compiled carbon isotopic data from samples that were deposited during a proposed Cretaceous mantle plume event. She estimated the onset of the mantle plume event at 125 Ma with a global positive carbon excursion at 115 Ma, and the excursion impacted both the organic and carbonate $\delta^{13}C$ values. The carbon excursion associated with the Cretaceous mantle plume event began at least 10 Ma after the onset of increased oceanic crust production and subduction-associated volcanism.

If a delay in the chemical changes of seawater is typical of a mantle plume event, the estimated age of the onset of magmatism related to the proposed mantle plume event at 2.5 Ga is approximately 2.49 Ga and should continue until approximately 2.45 Ga (Kump et al., 2001). This time interval roughly corresponds with the deposition of the banded iron formations on the Kaapvaal craton and in the Hammersley basin. In fact, positive carbon excursions are recorded in carbonates that lie unconformably above the banded iron formation after the onset of the possible mantle plume event (Buick et al.,

1998). Buick et al. (1998) record a positive excursion in $\delta^{13}C_{carb}$ of carbonates deposited in the Transvaal Supergroup of the Transvaal basin at 2.43 Ga. Both this excursion and the positive excursion associated with the Cretaceous mantle plume event occurred a minimum of 10 My after the onset of volcanism.

It is more difficult to find suitable samples for the study of organic carbon and sulfur isotopes after 2.45 Ga because there are few if any shale beds deposited at this time in the Griqualand West basin. The marine transgression that resulted in thick marine carbonates and black shales in the interiors of the continents had completely regressed by 2.4 Ga when the Earth experienced wide-scale glaciation (Kirschvink et al., 2000). Furthermore, black shale and carbonate deposits formed on the continental shelf of the Kaapvaal craton should have been subjected to deformation and metamorphism in the ensuing orogenies around the perimeter of the Kaapvaal craton. The samples analyzed in this study are incredibly homogenous and will provide an effective baseline for sedimentary sequences deposited above the banded iron formations.

7 Conclusions

1. Marine carbonates from the Griqualand West basin of the Kaapvaal craton, South Africa can be divided into two groups: Group I, which has microcrystalline dolomite and very little disruption of the original fabric, and Group II, which has macrocrystalline dolomite and is characterized by disrupted fabric.
2. Carbonates of Groups I and II show the same range of $\delta^{13}C_{carb}$ values (-0.9 to -0.1‰) and neither group shows substantial changes in $\delta^{13}C$ values with stratigraphic height.
3. $\delta^{13}C_{org}$ and $\delta^{34}S$ of black shales from the Griqualand West basin show only limited variation and do not vary systematically with stratigraphic height.
4. Trace metal contents (Li, B, Ti, V, Cr, Co, Ni, Cu, and Zn) and ratios do not vary significantly between carbonates of Groups I and II and they do not show systematic variation with stratigraphic height.
5. There is no suggestion of an excursion in the $\delta^{13}C_{carb}$ or trace metal contents and ratios in marine carbonates from the Griqualand West basin prior to a proposed mantle plume event at approximately 2.5 Ga. Likewise, $\delta^{13}C_{org}$ and $\delta^{34}S$ values of black shales in this succession do not show evidence of an isotopic excursion.
6. The Griqualand West carbonates have $\delta^{13}C_{carb}$ values that are isotopically lighter than carbonates of a similar age from the Hamersley basin in Western Australia, indicating possible differences in the chemical composition of seawater or diagenetic histories between the two basins.

References Cited

Al-Aasm, I. (2000). "Chemical and Isotopic Constraints for Recrystallization of Sedimentary Dolomites from the Western Canada Sed°imentary Basin." Aquatic Geochemistry **6**: 227-248.

Altermann, W. and Siegfried, H.P. (1997). "Sedimentology and facies development of an Archaean shelf: carbonate platform transition in the Kaapvaal Craton, as deduced from a deep borehole at Kathu, South Africa." Journal of African Earth Sciences **24**(3): 391-410.

Altermann, W. and Nelson, D.R. (1998). "Sedimentation rates, basin analysis and regional correlations of three Neoarchaean and Palaeoproterozoic sub-basins of the Kaapvaal craton as inferred from precise U-Pb zircon ages from volcaniclastic sediments." Sedimentary Geology **120**: 225-256.

Altermann, W., (2002), personal communication.

Armstrong, R.A., Compston, W., Retief, E.A., Williams, I.S. and Welke, H.J. (1991). "Zircon ion microprobe studies bearing on the age and evolution of the Witwatersrand triad." Precambrian Research **53**: 243-266.

Azmy, K., Veizer, J., Misi, A., de Oliveira, T.F., Sanches, A.L. and Dardenne, M.A. (2001). "Dolomitization and isotope stratigraphy of the Vazante Formation, Sao Francisco Basin, Brazil." Precambrian Research **112**: 303-329.

Barley, M.E., Pickard, A.L. and Sylvester, P.J. (1997). "Emplacement of a large igneous province as a possible cause of banded iron formation 2.45 billion years ago." Nature **385**: 55-58.

Brand, U. and Veizer, J. (1980). "Chemical Diagenesis of a Multicomponent Carbonate System-1: Trace Elements." Journal of Sedimentary Petrology **50**(4): 1219-1236.

Buick, I.S., Uken, R., Gibson, R.L. and Wallmach, T. (1998). "High-d13C Paleoproterozoic carbonates from the Transvaal Supergroup, South Africa." Geology **26**(10): 875-878.

Clendenin, C.W., Charlesworth, E.G. and Maske, S. (1988). "An early Proterozoic three-stage rift system, Kaapvaal Craton, South Africa." Tectonophysics **145**: 73-86.

Condie, K. C., Des Marais, D. J. and Abbott, D. H. (2000). Geologic evidence for a mantle superplume event at 1.9 Ga. Geochemistry, Geophysics, Geosystems, **1**: Paper no. 2000GC000095.

Condie, K. C., Des Marais, D. J. and Abbott, D. H. (2001). Precambrian superplumes and supercontinents: a record in black shales, carbon isotopes, and paleoclimates? Precambrian Research **106**: 239-260.

Davis, C.L. (1998). Paleoceanographic Influences on Accumulation of Organic Matter and Trace Metals in Cretaceous Black Shale and Carbonate, Western Maracaibo Basin, Venezuela. Department of Geological Sciences. Bloomington, Indiana University: 348.

de Wit, M.J., Roering, C., Hart, R.J., Armstrong, R.A., de Ronde, C.E.J., Green, R.W.E., Tredoux, M., Peberdy, E. and Hart, R.A. (1992). "Formation of an Archaean continent." Nature **357**: 553-562.

Derry, L.A., Kaufman, A.J. and Jacobsen, S.B. (1992). "Sedimentary cycling and environmental change in the Late Proterozoic: Evidence from stable and radiogenic isotopes." Geochimica et Cosmochimica Acta **56**: 1317-1329.

Des Marais, D.J., Strauss, H., Summons, R.E. and Hayes, J.M. (1992). "Carbon isotope evidence for the stepwise oxidation of the Proterozoic environment." Nature **359**: 605-609.

Eriksson, P.G., Schreiber, U.M. and van der Neut, M. (1991). "A review of the sedimentology of the Early Proterozoic Pretoria Group, Transvaal Sequence, South Africa: implications for tectonic setting." Journal of African Earth Sciences **13**(1): 107-119.

Eriksson, P.G. and Altermann, W. (1998). "An overview of the geology of the Transvaal Supergroup dolomites (South Africa)." Environmental Geology **36**(1-2): 179-188.

Eriksson, P.G., Mazumder, R., Sarkar, S., Bose, P.K., Altermann, W., and van der Merwe, R. (1999). "The 2.7-2.0 Ga volcano-sedimentary record of Africa, India, and Australia: evidence for global and local changes in sea level and continental freeboard." Precambrian Research **97**: 269-302.

Eriksson, P.G., Martins-Neto, M.A., Nelson, D.R., Aspler, L.B., Chiarenzelli, J.R., Catuneanu, O., Sarkar, S., Altermann, W., and de W. Rautenbach, C.J. (2001). "An introduction to Precambrian basins: their characteristics and genesis." Sedimentary Geology **141-142**: 1-35.

Farquahar, J., Bao, H. and Thiemans, M. (2000). "Atmospheric influence of Earth's earliest sulfur cycle." Science **289**: 756-758.

Folk, Robert L., (1987). "Detection of organic matter in thin-sections of carbonate rocks using a white card." Sedimentary Geology 54: 193-200.

Force, E.R. (1984). "A Relation Among Geomagnetic Reversals, Seafloor Spreading Rate, Paleoclimate, and Black Shales." EOS **65**(3): 18-19.

Fryer, B.J., Fyfe, W.S. and Kerrich, R. (1979). "Archaean Volcanogenic Oceans." Chemical Geology **24**: 25-33.

Garzanti, E. (1993). "Himalayan ironstones, "superplumes," and the breakup of Gondwana." Geology **21**: 105-108.

Heaman, L.M. (1997). "Global mafic magmatism at 2.45 Ga: Remnants of an ancient large igneous province?" Geology **25**(4): 299-302.

Hoefs, J. (1997). Stable Isotope Geochemistry, Berlin, Springer-Verlag, 201 p.

Holmden, C., Creaser, R.A., Muehlenbachs, K., Leslie, S.A. and Bergstrom, S.M. (1998). "Isotopic evidence for geochemical decoupling between epeiric seas and bordering oceans: Implications for secular curves." Geology **26**(6): 567-570.

Isley, A.E. and Abbott, D.H. (1999). "Plume-related mafic volcanism and the deposition of banded iron formations." Journal of Geophysical Research **104**(B7): 15,461-15,477.

Jahren, A.H. (2002). "The biogeochemical consequences of the mid-Cretaceous superplume." Journal of Geodynamics **34**: 177-191.

Karhu, J.A. (1993). "Paleoproterozoic Evolution of the Carbon Isotope Ratios of Sedimentary Carbonates in the Fennoscandian Shield." Geological Survey of Finland, Bulletin 371.

Kerr, A. C. (1998). "Oceanic plateau formation: a cause of mass extinction and black shale deposition around the Cenomanian-Turonian boundary?" Journal of the Geological Society of London **155**: 619-626.

Kirschvink, J.L., Gaidos, E.J., Bertani, L.E., Beukes, N.J., Gutzmer, J., Maepa, L.N. and Steinberger, R.E. (2000). "Paleoproterozoic snowball Earth: Extreme climatic and geochemical global change and its biological consequences." Proceedings of the National Academy of Sciences of the United States of America **97**(4): 1400-1405.

Klemm, D.D. (2000). "The formation of Palaeoproterozoic banded iron formations and their associated Fe and Mn deposits, with reference to the Griqualand West deposits, South Africa." Journal of African Earth Sciences **30**(1): 1-24.

Kump, L.R. and Arthur, M.A. (1999). "Interpreting carbon-isotope excursions: carbonates and organic matter." Chemical Geology **161**: 181-198.

Kump, L.R., Kasting, J.F. and Barley, M.E. (2001). "Rise of atmospheric oxygen and the "upside-down" Archean mantle." Geochemistry, Geophysics, Geosystems **2**: 1-15.

Larson, R.L. (1991). "Geological consequences of superplumes." Geology **19**: 963-966.

Larson, R.L. and Pitman, W.C.I. (1972). "World-Wide Correlation of Mesozoic Magnetic Anomalies, and Its Implications." Geological Society of America Bulletin **83**: 3645-3662.

Lee, M. and Behke, C.M. (1996). "A model of isotope fractionation in reacting geochemical systems." American Journal of Science **296**: 965-988.

Lindsay, J.F. and Brasier, M.D. (2002). "Did global tectonics drive early biosphere evolution? Carbon isotope record from 2.6 to 1.9 Ga carbonates of Western Australian basins." Precambrian Research **114**: 1-34.

Machel, H.G., Mason, R.A., Mariano, A.N. and Mucci, A. (1991). Causes and Emission of Luminescence in Calcite and Dolomite. Luminescence Microscopy: Quantitative and Qualitative Aspects. C. E. Barker and O. C. Kopp.

Melezhik, V.A. and Fallick, A.E. (1996). "A widespread positive d13Ccarb anomaly at around 2.33-2.06 on the Fennoscandian Shield: a paradox?" Terra Research **8**: 141-157.

Meyer, F.M. and Robb, L.J. (1996). "The geochemistry of Black Shales from the Chuniespoort Group, Transvaal Sequence, Eastern Transvaal, South Africa" Economic Geology **91**: 111-121.

Nesse, W. D. (1986) Introduction to Optical Mineralogy. New York: Oxford University Press, 335 p.

Ohmoto, H. and Felder, R.P. (1987). "Applications of sulfur and carbon isotopes in ore deposit research." In H. L. Barnes, ed., Hydrothermal Ore Deposits, v. 3, J. Wiley, NY.

Pavlov, A.A., Kasting, J.F., Brown, L.L., Rages, K.A., and Freedman, R. (2000). "Greenhouse warming by CH4 in the atmosphere of early Earth." Journal of Geophysical Research, E, Planets **105**(5): 11,981-11,990.

Puchtel, I.S., Haase, K.M., Hofmann, A.W., Chauvel, C., Kulikov, V.S., Garbe-Schonberg, C.-D. and Nemchin, A.A. (1997). "Petrology and geochemistry of crustally contaminated komatiitic basalts from the Vetreny Belt, southeastern Baltic Shield: Evidence for an early Proterozoic mantle plume beneath rifted Archean continental lithosphere." Geochemica et Cosmochimica Acta **61**(6): 1205-1222.

Schidlowski, M. (1995). "Isotope Fractionations in the Terrestrial Carbon Cycle: A Brief Overview." Advancements in Sapce Research **15**(3): 441-449.

Schlanger, S.O., Jenkyns, H.C. and Premoli-Silva, I. (1981). "Volcanism and Vertical Tectonics in the Pacific Basin Related to Global Cretaceous Transgressions." Earth and Planetary Science Letters **52**: 435-449.

Simonson, B.M. and Hassler, S.W. (1996). "Was the Deposition of Large Precambrian Iron Formations Linked to Major Marine Transgressions?" The Journal of Geology **104**: 665-676.

Simonson, B.M., Koeberl, C., McDonald, I. and Reimold, W.U. (2000). "Geochemical evidence for an impact origin for a Late Archean spherule layer, Transvaal Supergroup, South Africa." Geology **28**(12): 1103-1106.

Strauss, H. and Beukes, N.J. (1996). "Carbon and sulfur isotopic compositions of organic carbon and pyrite in sediments from the Transvaal Supergroup, South Africa." Precambrian Research **79**: 57-71.

Strauss, H. and Moore, T.B. (1992). Abundances and Isotopic Compositions of Carbon and Sulfur Species in Whole Rock and Kerogen Samples. The Proterozoic Biosphere: A multidisciplinary study. J. W. Schopf and C. Klein. Cambridge, Cambridge University Press: 711-798.

Sumner, D.Y. and Bowring, S.A. (1996). "U-Pb geochronologic constraints on deposition of the Campbellrand Subgroup, Transvaal Supergroup, South Africa." Precambrian Research **79**: 25-35.

Tankard, A.J., Jackson, M.P.A., Eriksson, K.A., Hobday, D.K., Hunter, D.R. and Minter, W.E.L. (1982). Crustal Evolution of Southern Africa: 3.8 Billion Years of Earth History. New York, Springer-Verlag, 523 p.

Thomas, R.J., von Veh, M.W. and McCourt, S. (1993). "The tectonic evolution of southern Africa: an overview." Journal of African Earth Sciences **16**(1/2): 5-24.

Treloar, P.J., Coward, M.P. and Harris, N.B.W. (1992). "Himalayan-Tibetan analogies for the evolution of the Zimbabwe Craton and Limpopo Belt." Precambrian Research **55**: 571-587.

Tucker, M.E. (2001). Sedimentary Petrology: An Introduction to the Origin of Sedimentary Rocks. Oxford, Blackwell Science Ltd., 261 p.

Valladares, I., Recio, C. and Lendinez, A. (1996). "Sequence stratigraphy and stable isotopes (d13C, d18O) of the Late Cretaceous carbonate ramp of the western margin of the Iberian Chain (Soria, Spain)." Sedimentary Geology **105**: 11-28.

Veizer, J. (1983). Trace Elements and Isotopes in Sedimentary Carbonates. Carbonates: Mineralogy and Chemistry. R. J. Reeder. Washington, DC, Mineralogical Society of America. **11:** 394.

Watanabe, Y., Naraoka, H., Wronkiewicz, D.J., Condie, K.C. and Ohmoto, H. (1997). "Carbon, nitrogen, and sulfur geochemistry of Archean and Proterozoic shales from the Kaapvaal Craton, South Africa." Geochimica et Cosmochimica Acta **61**(16): 3441-3459.

Winhusen, E.R. (2001). Precambrian seawater temperature analysis using oxygen isotopes from Hamersley carbonates, Western Australia. Cincinnati, University of Cincinnati: unpaginated.

Appendix A: Methods

1.1. Analysis of Carbonates

1.1.1. Carbon and Oxygen Isotopes

Approximately 15-30 milligrams of crushed sample were measured and placed into one side or a split reaction vessel. One reaction vessel was loaded with Solenhofen limestone, a calcite standard. Phosphoric acid (H_3PO_4) was added to the opposite side of the reaction vessel. The reaction vessels were placed on a CO_2 extraction line to vacuum out the atmosphere for 4 hours. The reaction vessels were then tipped so that the acid and the carbonate sample would react with each other. The vessels were then placed in a bath of ~50°C for approximately 12 hours. After reacting, the samples were cryogenically transferred from the sample reaction vessel to sample collection vessels. After all the samples had been collected, they were run on a duel inlet gas source magnetic sector isotope ratio mass spectrometer using PDB as the standard.

1.1.2. Trace Elements

Approximately 0.2 to 0.3 grams of crushed sample were measured into a Teflon beaker. One beaker was loaded with a standard, Claritas PPT Instrument Calibration Standard 1. 5 ml of reverse osmosis H_20 (RO H_20) were added. Then 5 ml of nitric acid (HNO_3) were added. The beakers were capped immediately. After 10-15 minutes at room temperature, the samples were put into a microwave. The samples were microwaved according to a pre-established protocol for biomass. After samples had been microwaved and cooled, the samples were filtered for residual material. The volume of the sample containers was brought to 50 mL by adding RO H_20. Before introducing the samples to the mass spectrometer, the samples were diluted a second time at a ratio of 1:4

(sample: RO H_20). The samples were then run on an Agilent 7500i inductively coupled plasma mass spectrometer (ICP-MS).

1.1.3. Petrography

Thin sections were analyzed under plane-polarized light (ppl) and cross-polarized light (xpl) without coverglasses. Thin sections were then viewed under reflected light with a white card as background and temporary cover slips. This allowed the organic matter in the thin sections to be viewed more efficiently. Uncovered, unpolished thin sections were also analyzed on a ELM-3R Luminiscope. They were analyzed at vacuums of approximately 130 millitorr at 0.5 mA with voltages between 10-15 kV. The beam focus was between 25-50%.

Analysis of Shales

1.1.4. Carbon Isotopes

To prepare the shale samples for organic carbon analysis, the organic carbon was separated from any carbonate carbon contained in the sample. To do this the crushed sample is digested in cold, followed by hot, 10% and concentrated (approximately 70%) hydrochloric acid. The resulting solution and solids are washed three times with distilled water and centrifuged between washes. The last washings are decanted and the resultant solids digested with cold 70% concentrated hydrofluoric acid for 16 hours. This solution is agitated to ensure complete acid treatment. The remaining hydrofluoric acid solution is centrifuged and decanted. Then it is washed 3 more times with distilled water, centrifuging between washings. Acidic zinc bromide solution is added to the resultant solids. This solution is then shaken to disperse solids and centrifuge. The organic matter is decanted and transferred into a glass test tube where it is diluted with water and

centrifuged. This solution is decanted with diluted zinc bromide and the resultant solid is washed three times with distilled water. Geochem Laboratories Inc performed this part of the procedure.

To determine the carbon isotopic composition of these solids, the organic matter is placed in a silver capsule and heated to 1325°C with a He flow. This reduces the organic matter to carbon monoxide (CO), which is then run on a Delta^{Plus}XL mass spectrometer. This portion of the procedure was performed by the stable isotope lab at University of New Mexico.

1.1.5. Sulfur Isotopes

Crushed shale samples were reacted using a Cr-reduction technique to form H_2S that was captured in Zn acetate solution as ZnS. After decanting the Zn Acetate solution and rinsing the ZnS three times with millipore water, the ZnS was converted to Ag_2S by reaction with $AgNO_3$. The Ag_2S was centrifuged and the $AgNO_3$ solution decanted. The $AgNO_3$ solution was then dried in an 80° C oven. Once dry, the resultant solid was analyzed on a Micromass Isoprime mass spectrometer. The entire procedure was performed at the University of Maryland, College Park.

Appendix B: Thin Section Analysis

WA 92/51 (Group 1 – Microcrystalline, Primary fabric evident)

This thin section transects a stromatolite head. It is mostly composed of recrystallized, microcrystalline dolomite rhombs (Figure B.1). However, organic matter forms in bands in the layers of the stromatolite head, which serve to outline the original morphology of the rock. In addition there are small nearly spherical collections of organic matter. There are also small irregularly shaped pockets that have been silicified. Several veins of dolomite run perpendicular to the stromatolite heads and cross cut the spherical collections of organic material. Cathodoluminescence of the thin section reveals two phases of dolomitization (Figure B.2). The first phase is characterized by bright red luminescent dolomite rhombs. The second phase is characterized by dark red luminescence that fills in the spaces between the bright red dolomite rhombs. Veins show a third type of luminescence that is light pink to white. Dolomitization crosses but does not completely obscure the primary fabric of the rock and indicates that the initial dolomitization did not begin immediately after deposition. Furthermore, there is no clastic material in this sample.

WA 92/38 (Group 1 – Microcrystalline, Primary fabric evident)

The thin section of WA 92/38 transects a stromatolite head. The thin section is predominantly recrystallized, microcrystalline dolomite rhombs, however organic matter occurs in very small spherical patches though out the thin section (Figure B.3). In addition, a vug appears at the base of the stromatolite head. The dolomite in the vug appears in a radiating spindle pattern and may represent recrystallization of a secondary

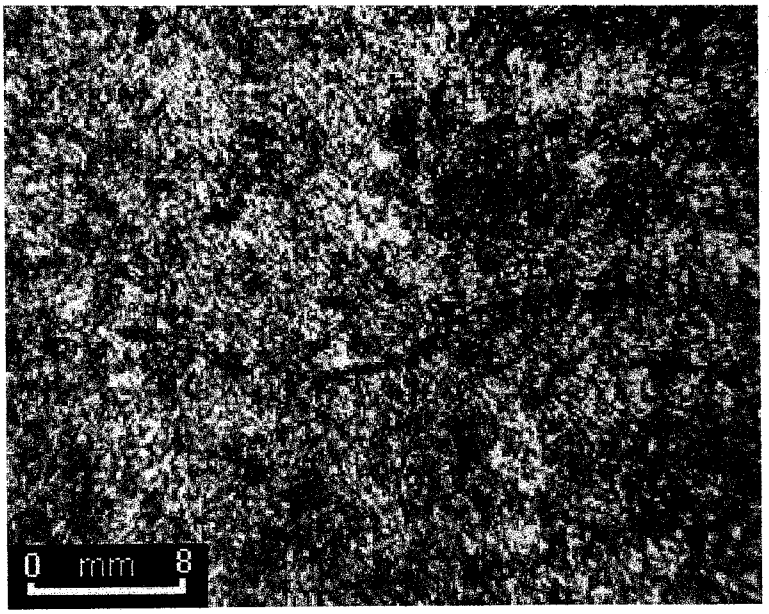

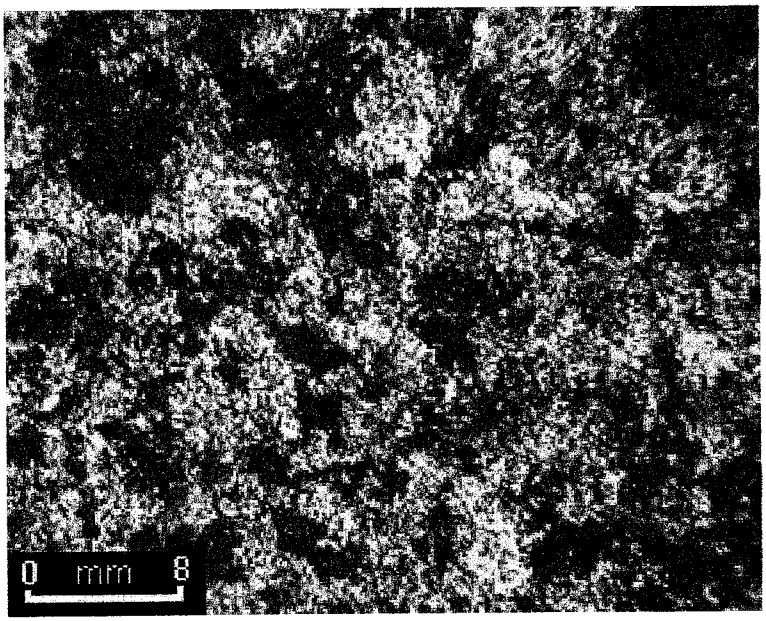

Figure B.1: Plane-polarized (upper image) and cross-polarized (lower image) photomicrographs of sample WA 92/51 showing microcrystalline dolomite.

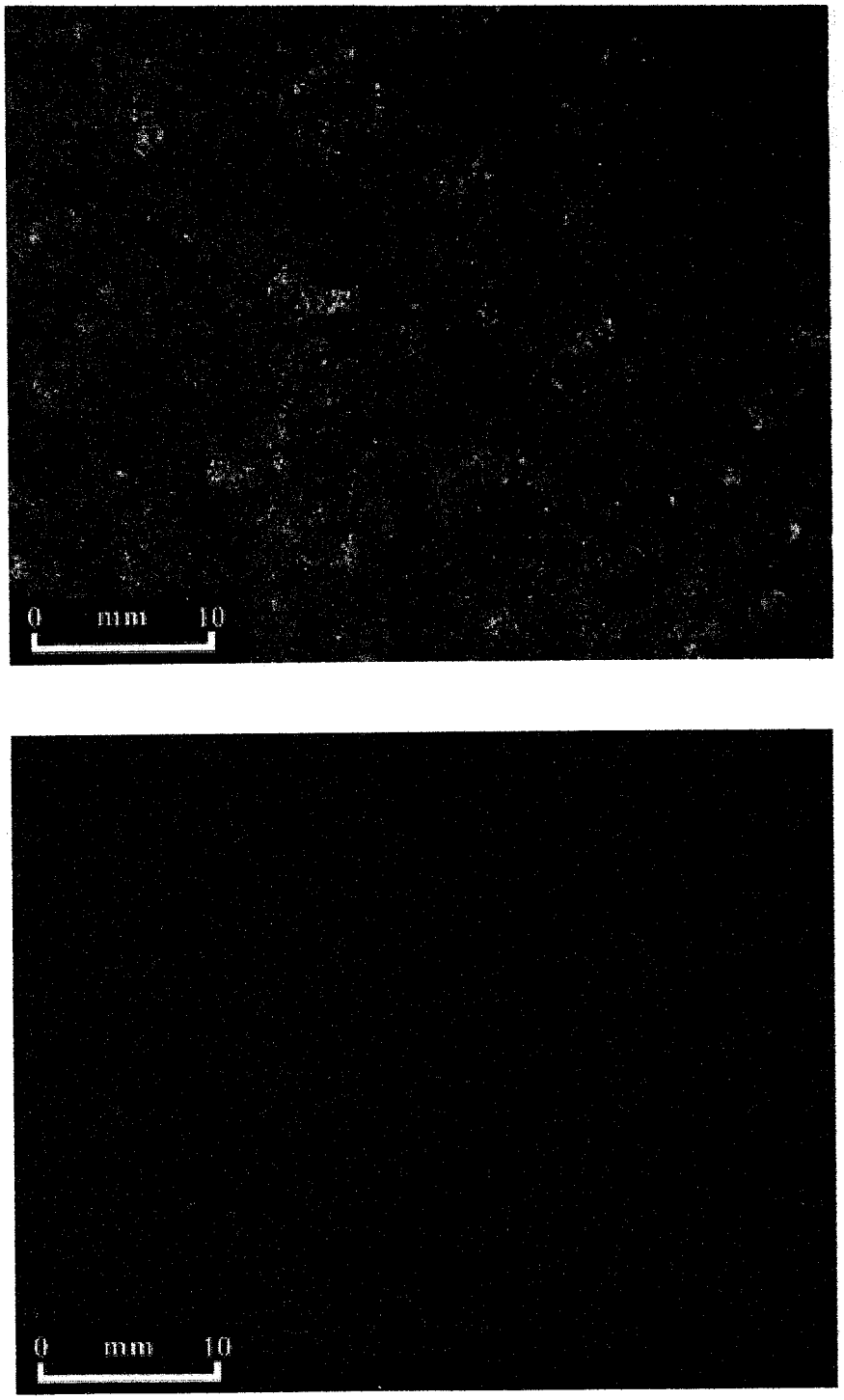

Figure B.2: Plane-polarized (upper image) and cathodoluminescent (lower image) photomicrographs of sample WA 92/51 showing two different shades of luminescent, in addition to a brightly luminescent vein.

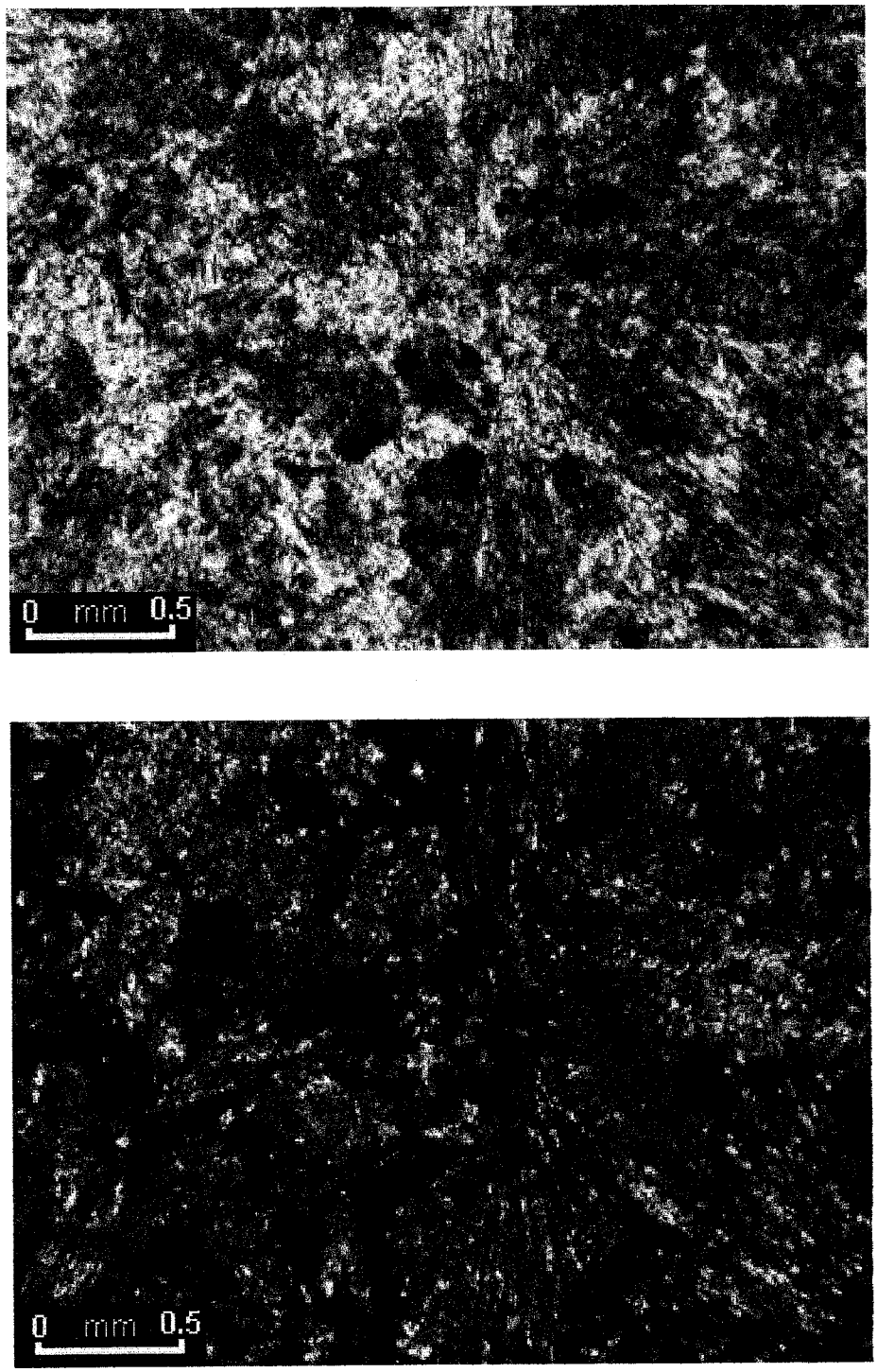

Figure B.3: Plane-polarized (upper image) and cross-polarized (lower image) photomicrographs of sample WA 92/38 showing primary fabric of rock.

mineral deposit (Figure B.4). An opaque mineral appears in the vug as well. Three small veins cross cut this thin section. One of the veins is silicic; the other two veins are dolomite and show individual zoning with in the veins. In cathodoluminescence, the majority of the thin section appears as bright red luminescent dolomite rhombs surrounded by a second composition of dark red luminescent matrix. There is no clastic material in this sample.

WA 92/34 (Group 2 – Macrocrystalline, Little or No Primary Fabric)

The thin section for sample WA 92/34 is composed of two distinct areas. The first area is microcrystalline dolomite. The second section is characterized by macrocrystalline dolomite rhombs (Figure B.5). Cleavage planes are sometimes visible with in the large dolomite rhombs. In addition, there is a late stage silicic cement surrounding some of the large rhombs. Organic matter has collected in a styolite and wispy pressure solution seams. Otherwise, the sample is organic free. There are no visible fractures or veins in this sample. Under cathodoluminescence, two distinct phases of dolomitization are shown (Figure B.6). The first phase is characterized by bright red luminescent dolomite rhombs. The second phase of dolomitization is characterized by dark red luminescent matrix surrounding the bright red luminescent dolomite rhombs. There is no clastic material in this sample.

KSC1 (Group 2 – Macrocrystalline, Little or No Primary Fabric)

This thin section is mostly microcrystalline recrystallized dolomite (Figure B.7). There are isolated larger dolomite rhombs, often associated with deposits of organic material. Organic material is distributed rather evenly throughout the thin section in bands that may represent the original fabric of the rock. However, dolomitization

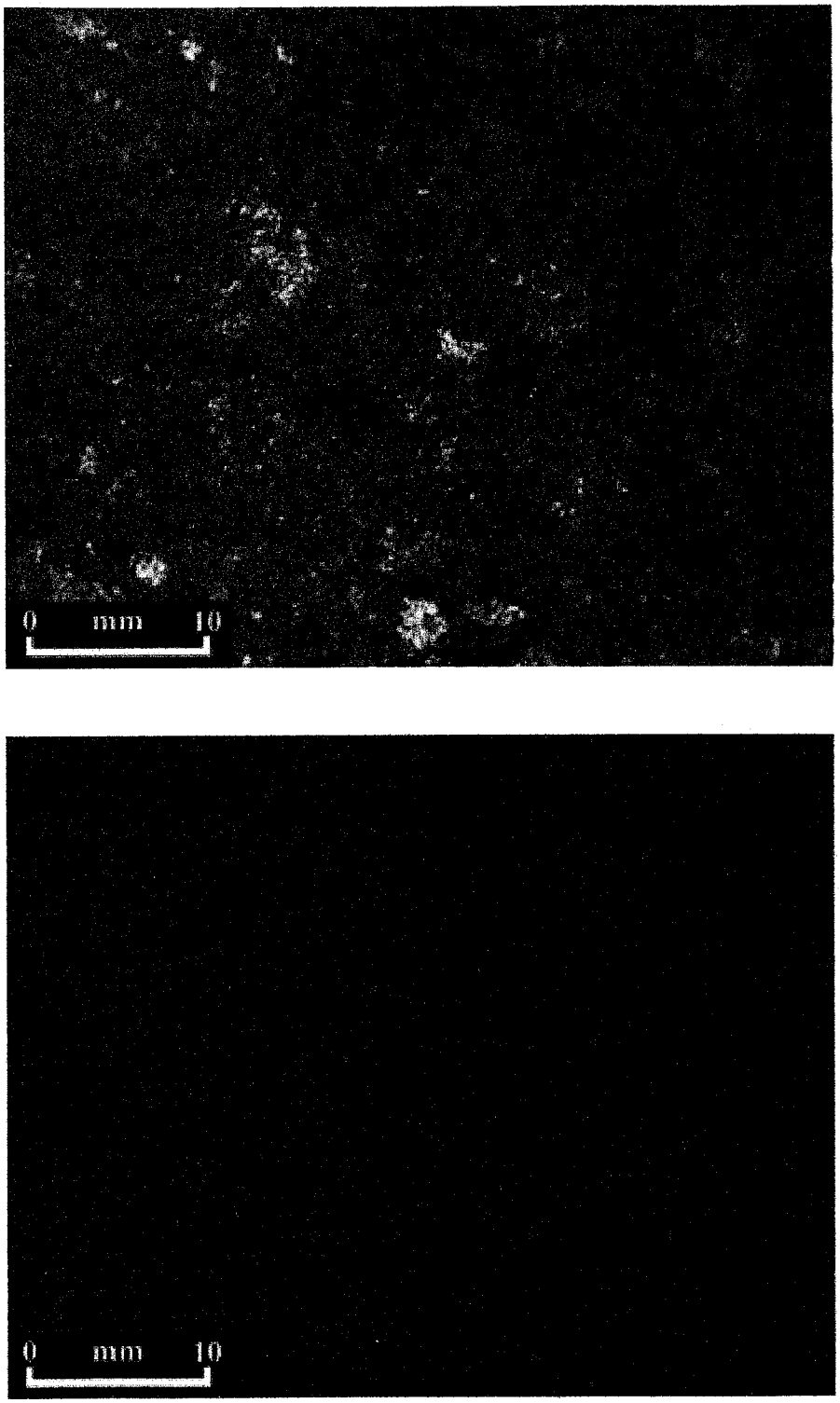

Figure B.4: Plane-polarized (upper image) and cathodoluminescent (lower image) photomicrographs of sample WA 92/38 showing a dolomite-filled vug.

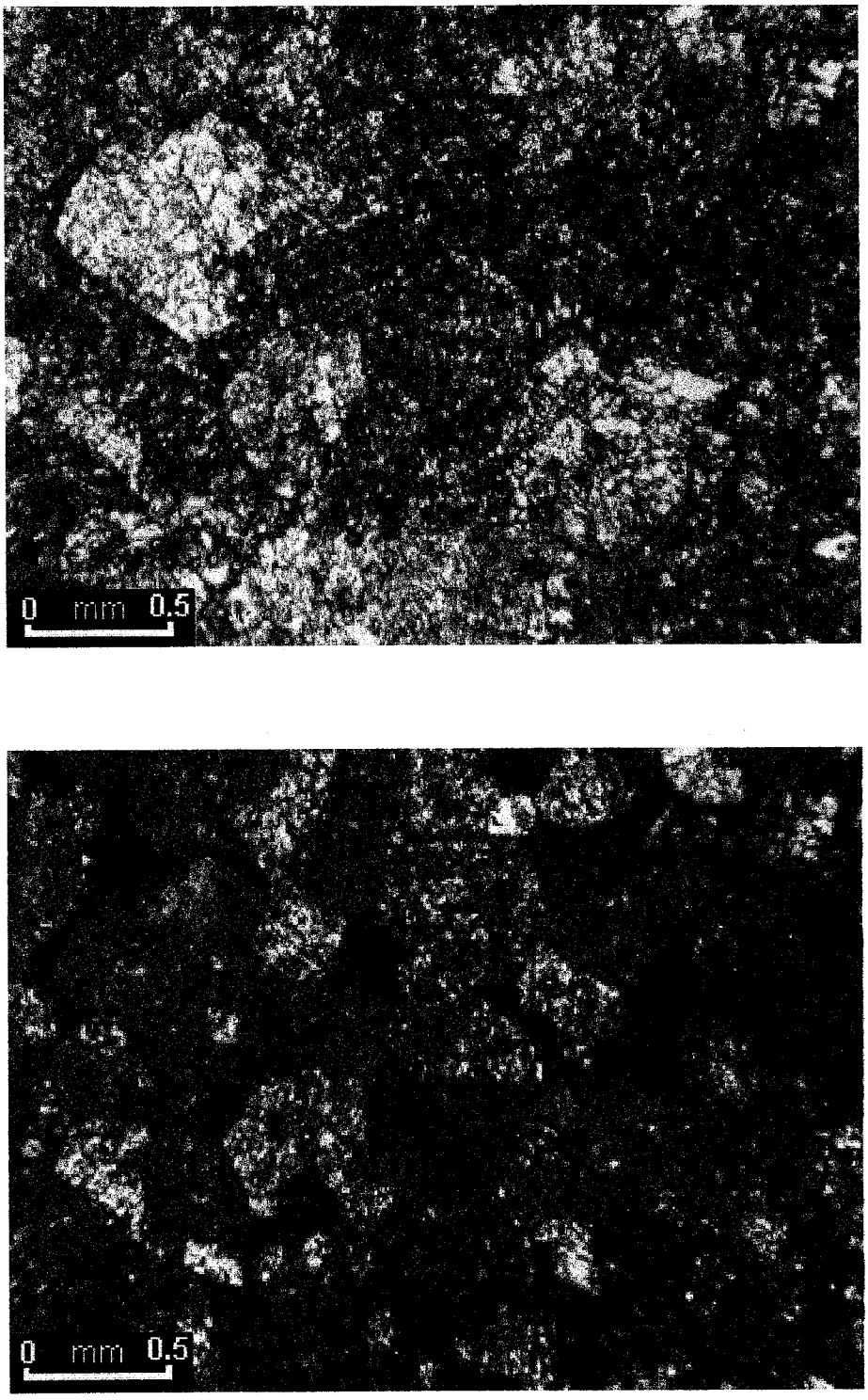

Figure B.5: Plane-polarized (upper image) and cross-polarized (lower image) photomicrographs of sample WA 92/34 showing macrocrystalline dolomite rhombs.

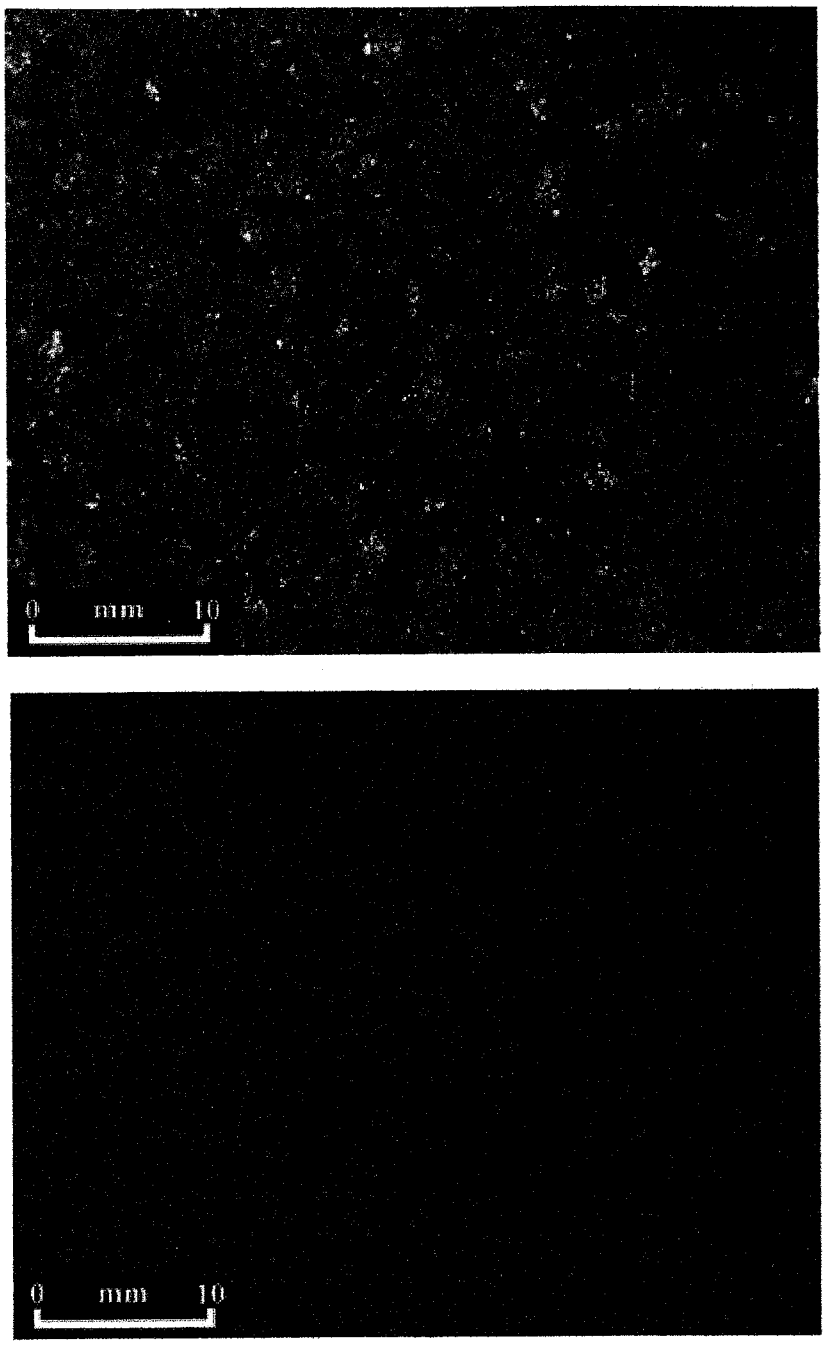

Figure B.6: Plane-polarized (upper image) and cathodoluminescent (lower image) photomicrographs of sample WA 92/34 showing different shades of cathodoluminescence.

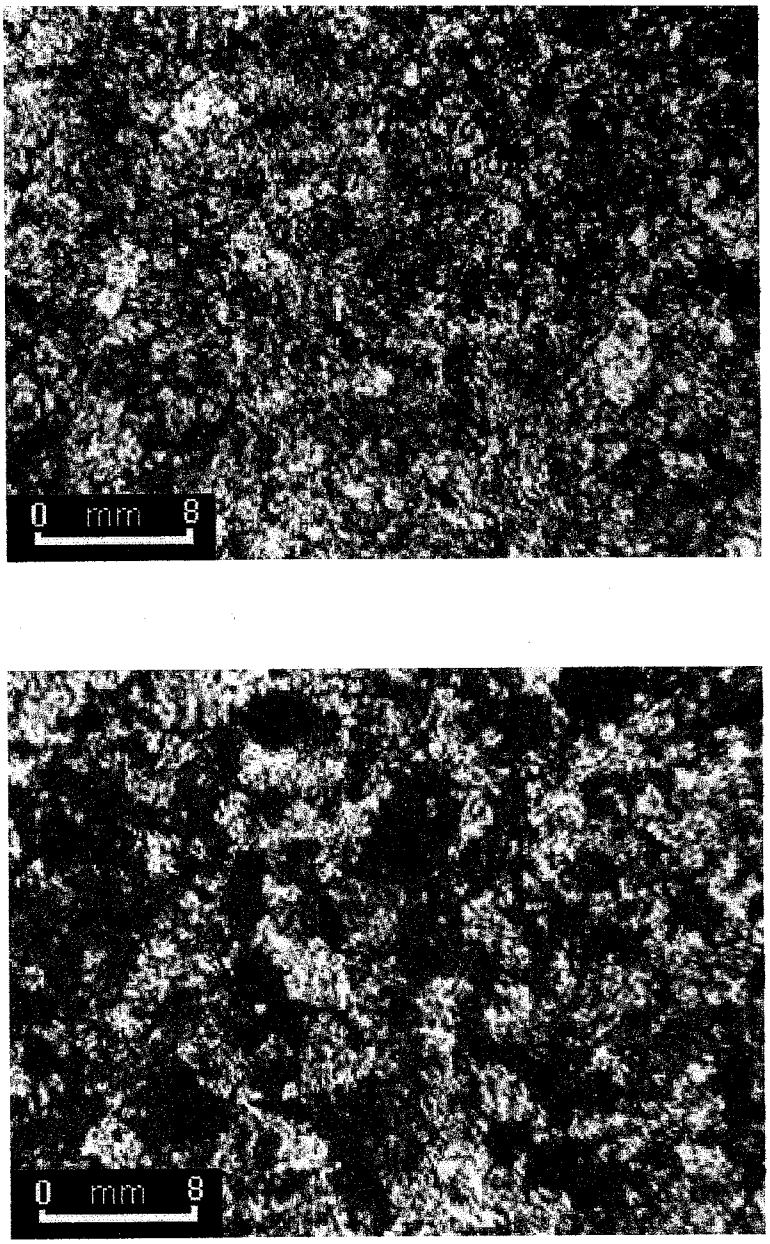

Figure B.7: Plane-polarized (upper image) and cross-polarized (lower image) photomicrographs of sample KSC1 showing macrocrystalline dolomite rhombs.

has almost completely obscured the original fabric. One small vein is visible transecting the organic bands. In cathodoluminescence, two distinct phases of dolomitization are revealed (Figure B.8). The first phase is characterized by bright red luminescent dolomite rhombs. The second phase of dolomitization is characterized by dark red luminescent matrix surrounding the bright red luminescent dolomite rhombs. There is no clastic material in this sample.

KSC2 (Group 2 – Macrocrystalline, Little or No Primary Fabric)

This thin section is almost entirely macrocrystalline recrystallized dolomite (Figure B.9). No primary fabric is visible. Furthermore, the dolomite forms a poikilotopic texture where it surrounds smaller dolomite rhombs. This indicates that there was more than one phase of dolomitization. Organic matter is absent except in pressure solution seams and styolites (Figure B.10). Cathodoluminescence of the thin section reveals two distinct phases of dolomitization. The first phase is characterized by bright red luminescent dolomite rhombs. The second phase of dolomitization is characterized by dark red luminescent matrix surrounding the bright red luminescent dolomite rhombs. There is no clastic material in this sample.

KSC3 (Group 2 – Macrocrystalline, Little or No Primary Fabric)

This sample is composed of macrocrystalline dolomite grains. The primary fabric is almost completely obscured by dolomitization. In addition, some of the dolomite grains are twinned, indicating that they were exposed to high pressures (Figure B.11). However, there is no evidence of metamorphism in this sample. This samples is almost completely devoid of organic matter except in styolites. There is a vein that is approximately 1 cm in thickness that runs through this sample. It is composed of

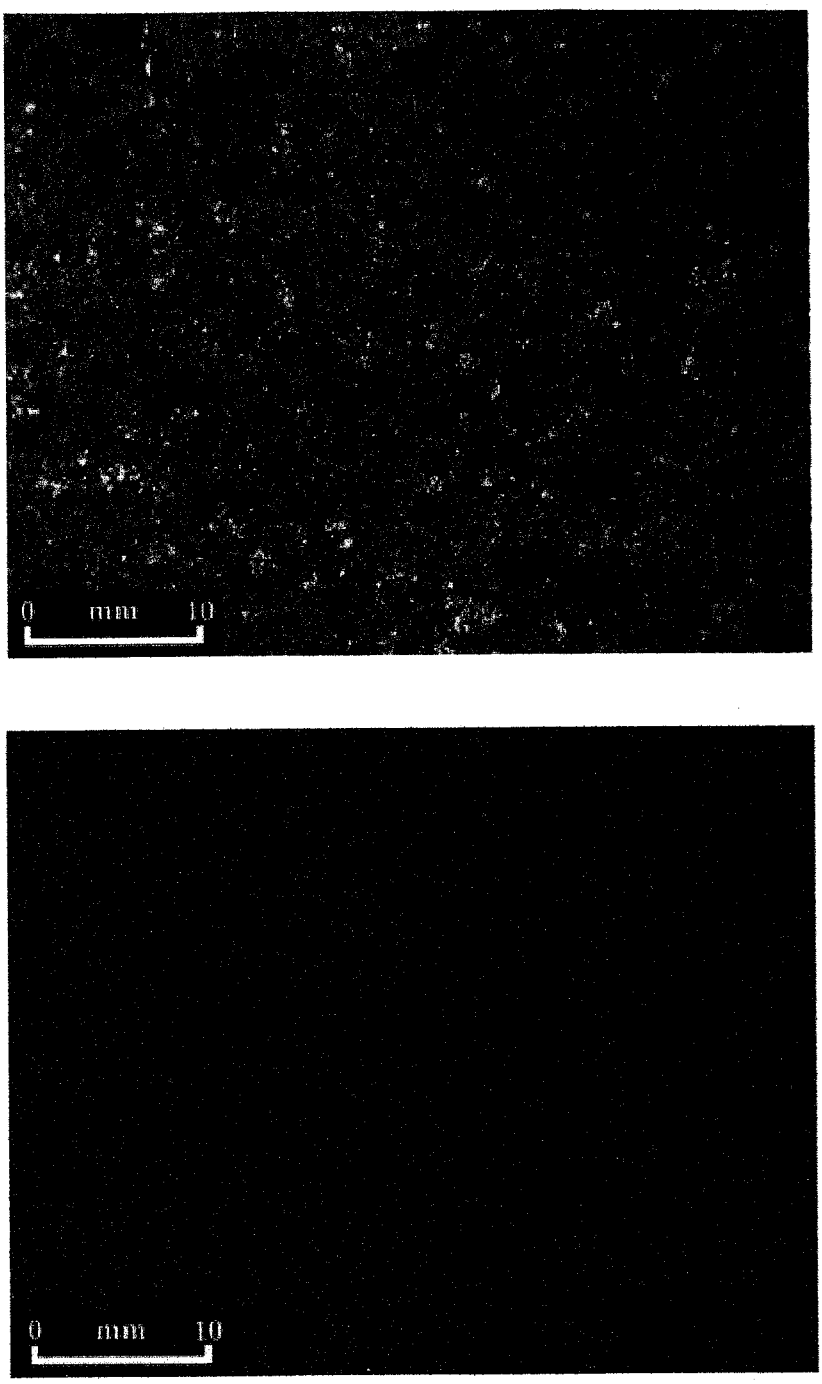

Figure B.8: Plane-polarized (upper image) and cathodoluminescent (lower image) photomicrographs of sample KSC1 showing different shades of dolomitization as well as a bright and a dark luminescent veins.

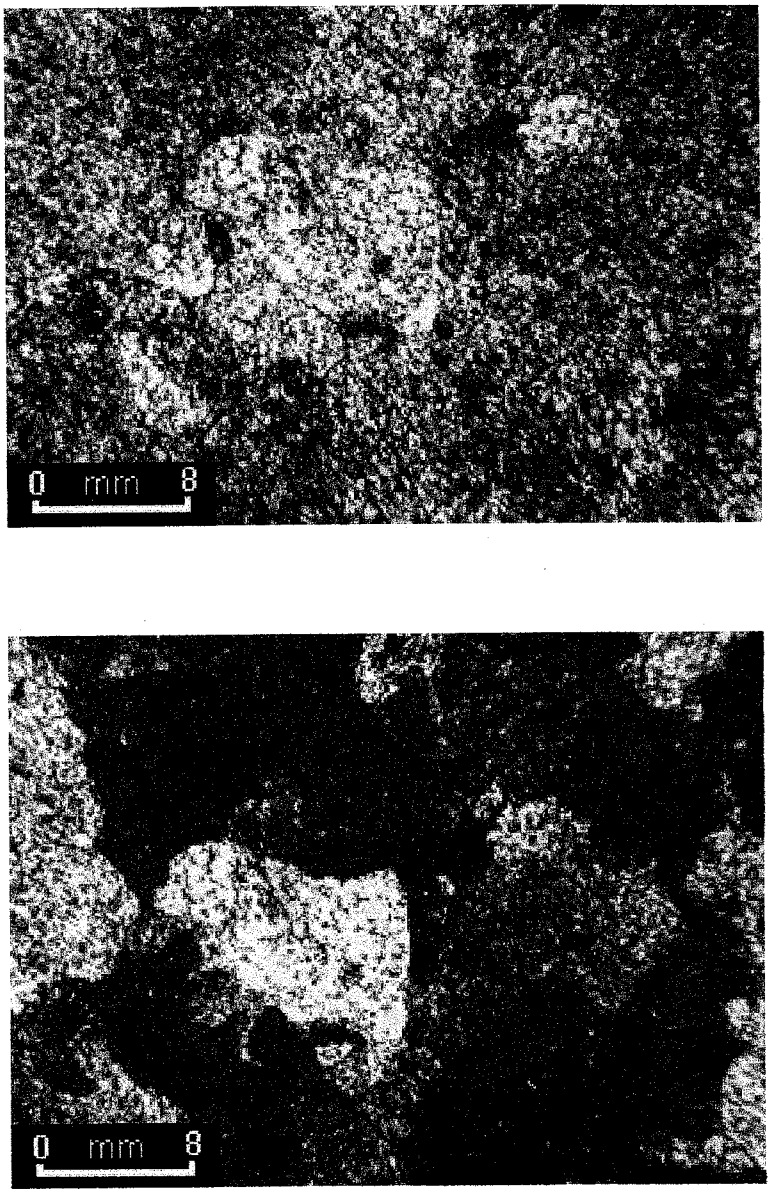

Figure B.9: Plane-polarized (upper image) and cross-polarized (lower image) photomicrographs of sample KSC2 showing poikilotopic dolomite.

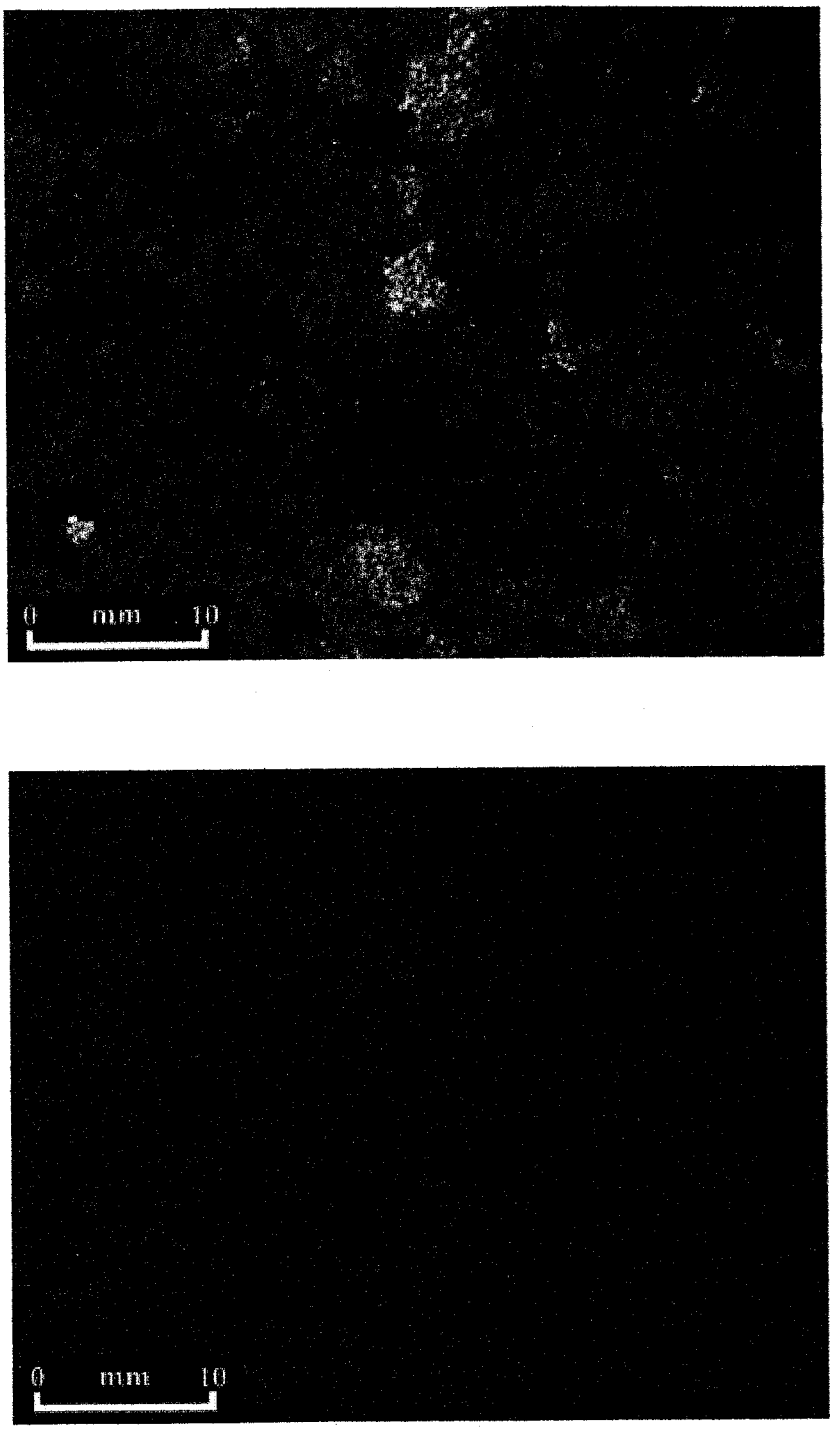

Figure B.10: Plane-polarized (upper image) and cathodoluminescent (lower image) photomicrographs of sample KSC2 showing different shades of cathodoluminescence as well as a styolite.

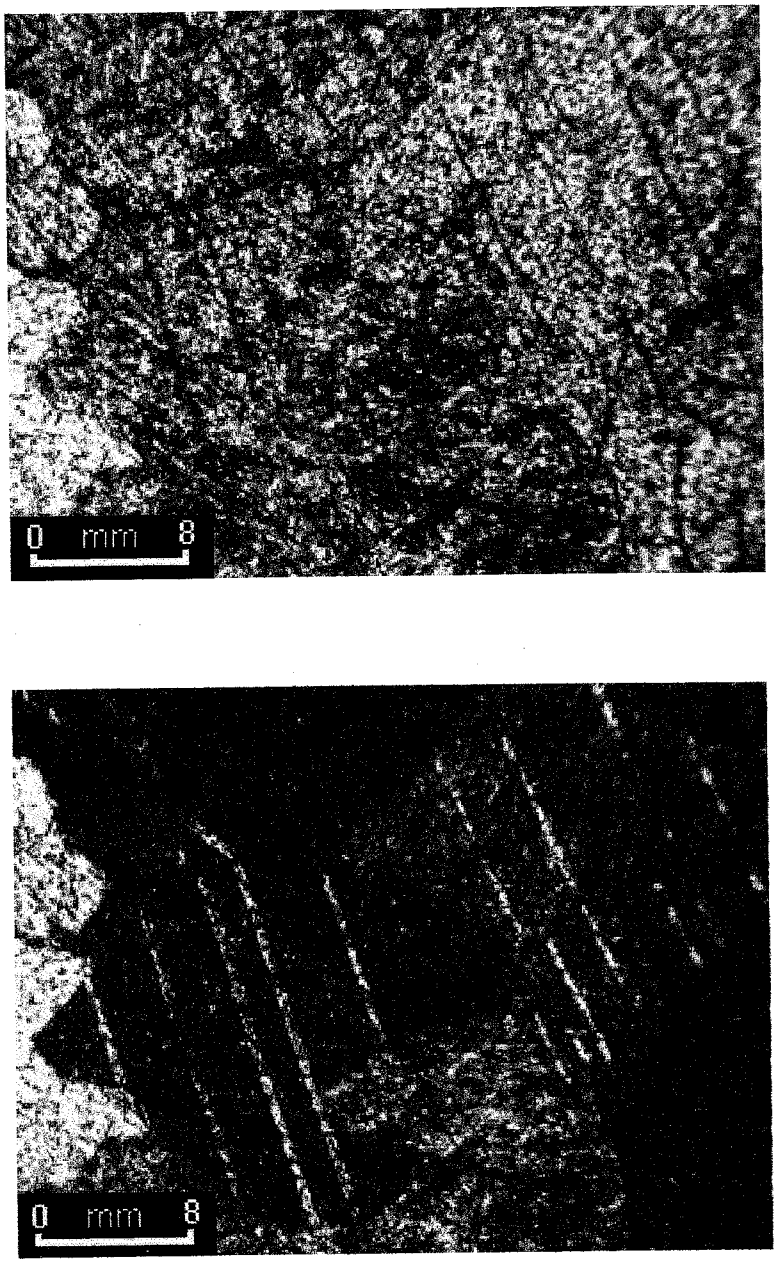

Figure B.11: Plane-polarized (upper image) and cross-polarized (lower image) photomicrographs of sample KSC3 showing carbonate twins.

macrocrystalline dolomite. Under cathodoluminescence, the dolomite grains in the vein have clear zonation, indicating that there was several generations of crystal growth under varying water compositions (Figure B.12). The remainder of the sample shows two distinct phases of dolomitization (Figure B.13). The first phase is characterized by bright red luminescent dolomite rhombs. The second phase of dolomitization is characterized by dark red luminescent matrix surrounding the bright red luminescent dolomite rhombs. There is no clastic material in this sample.

KSC5 (Group 1 – Microcrystalline, Primary fabric evident)

This sample cuts through two stromatolite heads. It is almost entirely microcrystalline dolomite (Figure B.14), however there are zones of larger dolomite rhombs within the matrix. In the microcrystralline regions, small rhombs are visible within the matrix. Under reflected light, wispy pressure solution seams composed of organic material are visible. Cathodoluminescence of the sample shows two distinct phases of dolomitization (Figure B.15). The first phase is characterized by bright red luminescent dolomite rhombs. The second phase of dolomitization is characterized by dark red luminescent matrix surrounding the bright red luminescent dolomite rhombs. There are no veins and no clastic material in this sample.

KSC7 (Group 2 – Macrocrystalline, Little or No Primary Fabric)

This sample is composed primarily of microcrystalline dolomite. Organic matter is distributed throughout the thin section (Figure B.16). It forms around macrocrystalline dolomite rhombs as well in wispy pressure solution seams and styolites. This thin section contains a vug that is filled with large dolomite rhombs and an opaque mineral.

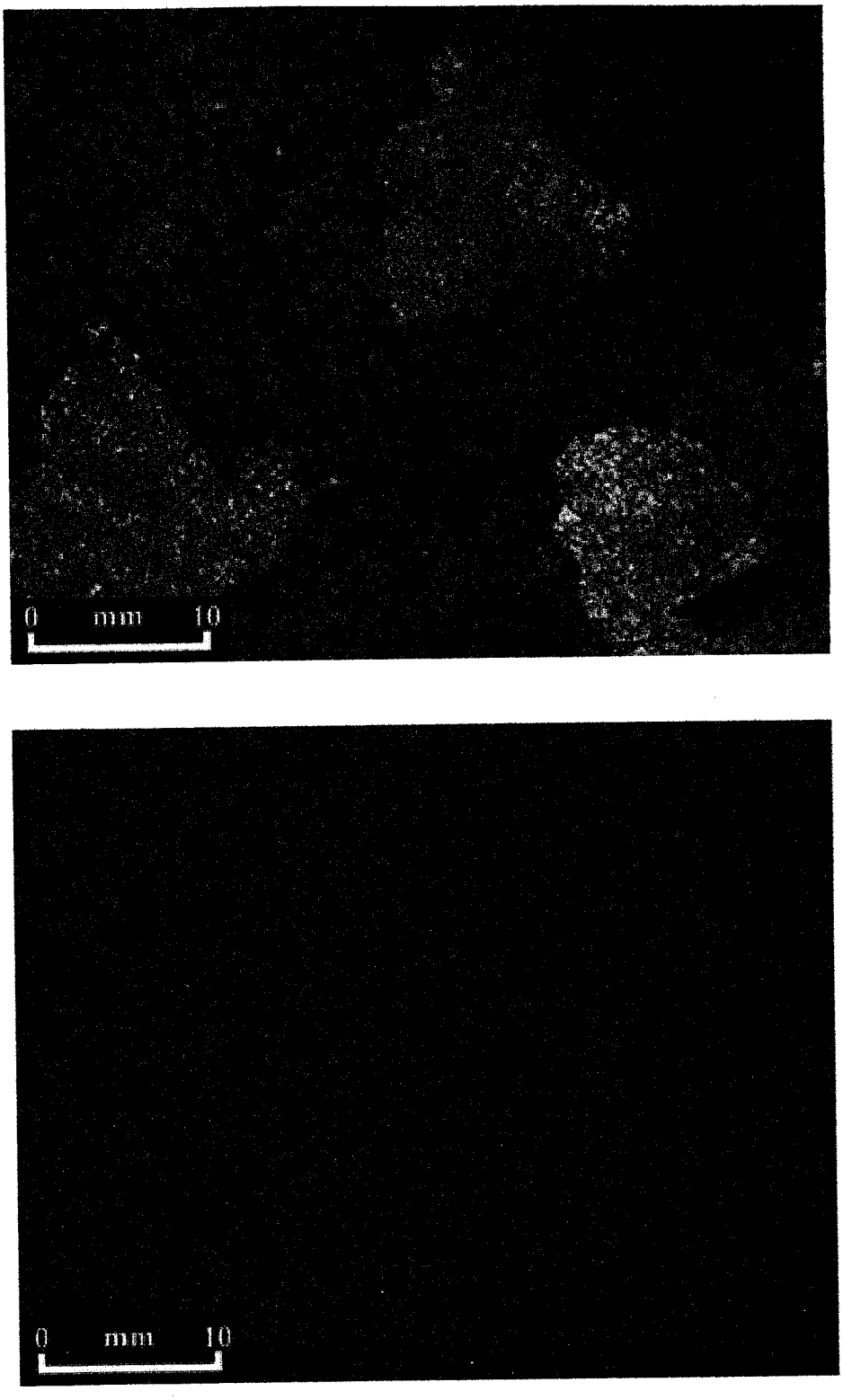

Figure B.12: Plane-polarized (upper image) and cathodoluminescent (lower image) photomicrographs of sample KSC3 showing zoned dolomite grains within a vein.

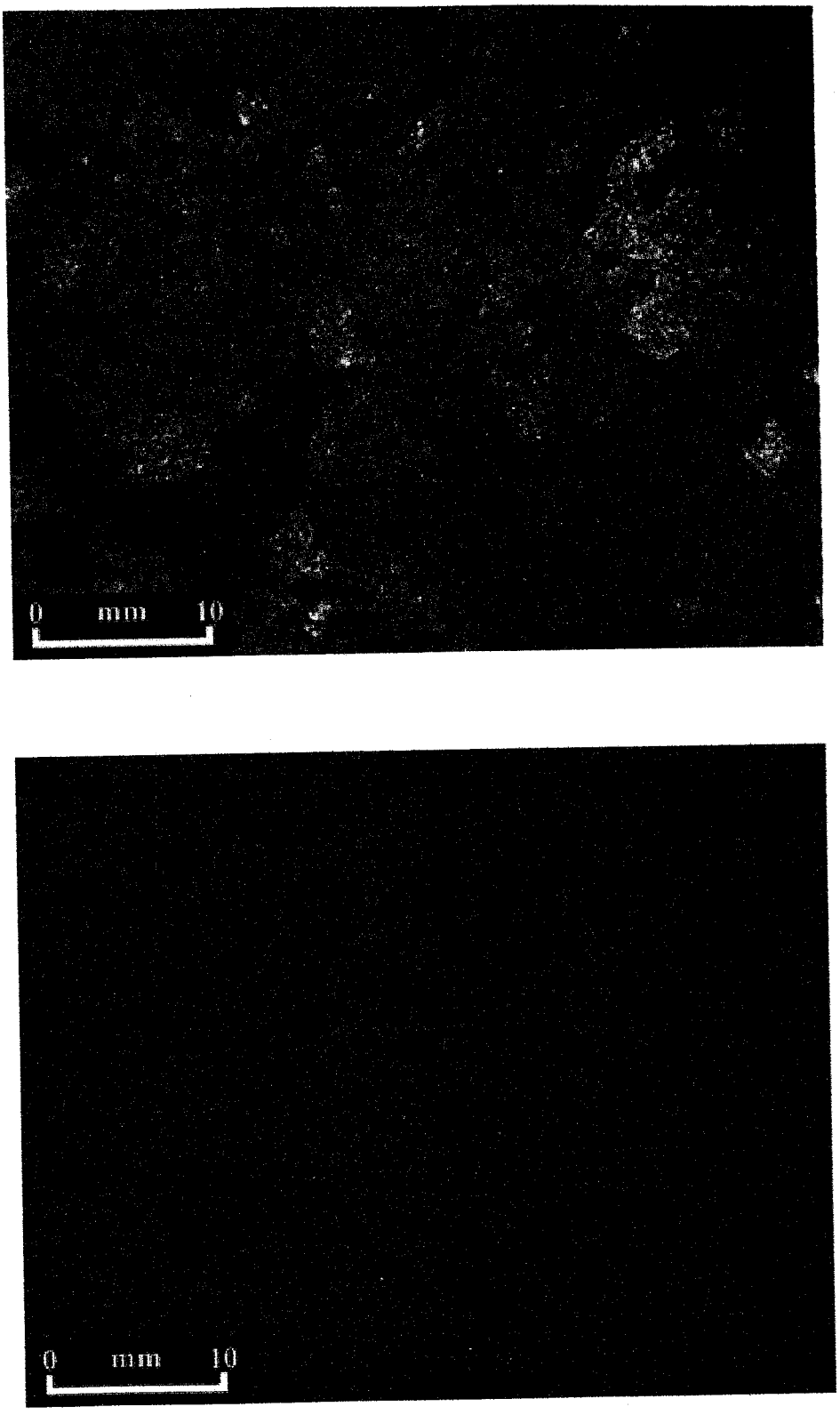

Figure B.13: Plane-polarized (upper image) and cathodoluminescent (lower image) photomicrographs of sample KSC3 showing two phases of dolomitization.

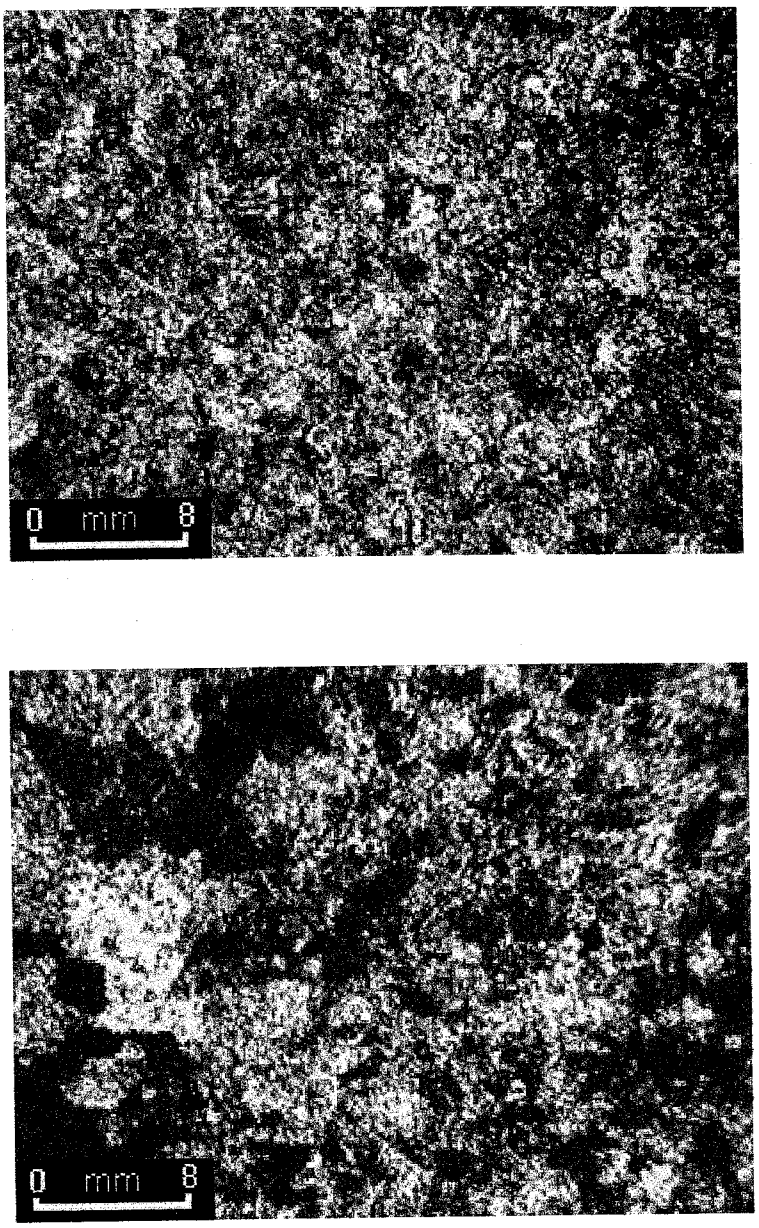

Figure B.14: Plane-polarized (upper image) and cross-polarized (lower image) photomicrographs of sample KSC5 showing microcrytalline dolomitization.

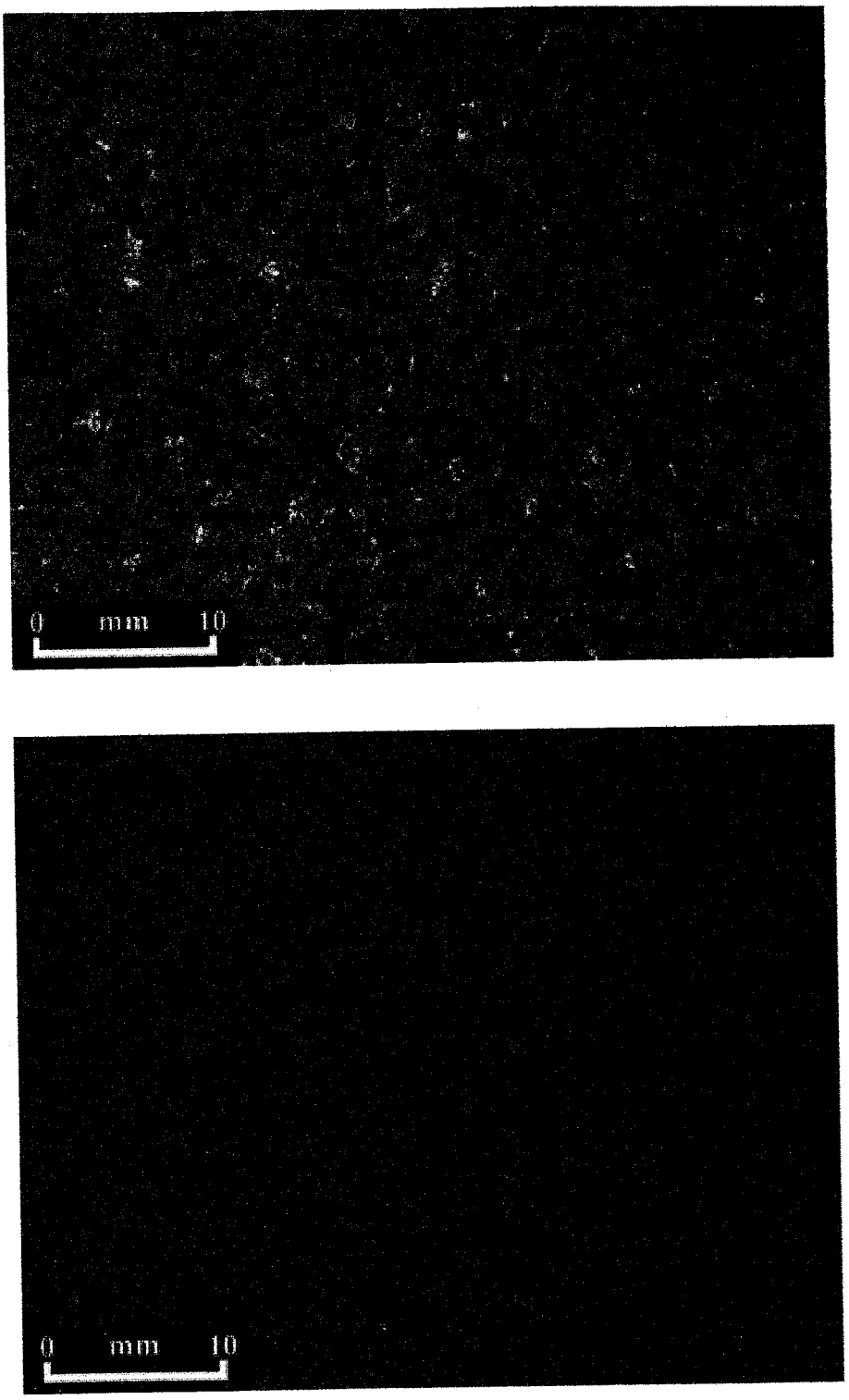

Figure B.15: Plane-polarized (upper image) and cathodoluminescent (lower image) photomicrographs of sample KSC5 showing two distinct shades of luminescence.

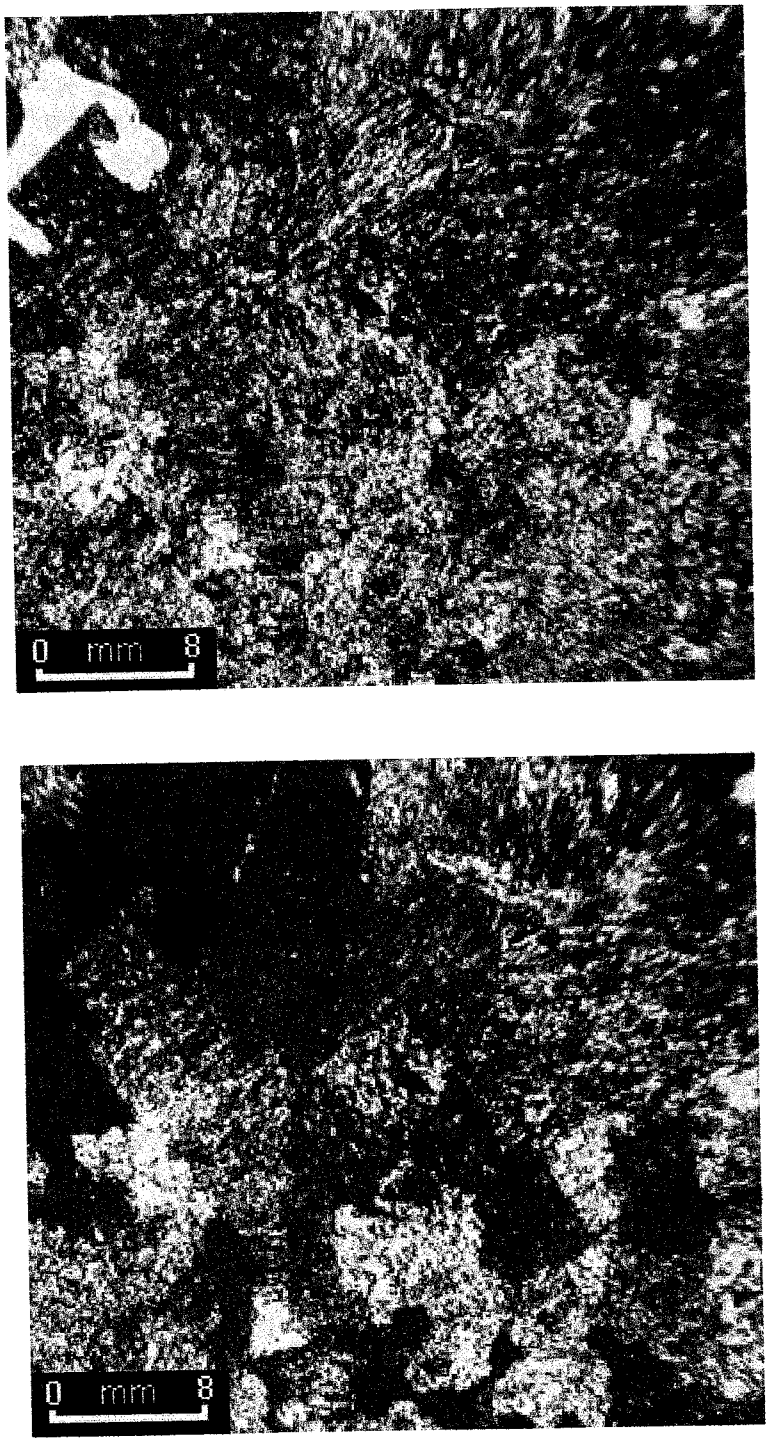

Figure B.16: Plane-polarized (upper image) and cross-polarized (lower image) photomicrographs of sample KSC7 showing macrocrystalline dolomitization.

Cathodoluminescence of the sample shows two distinct phases of dolomitization (Figure B.17). The first phase is characterized by bright red luminescent dolomite rhombs. The second phase of dolomitization is characterized by dark red luminescent matrix surrounding the bright red luminescent dolomite rhombs. There are no veins and no clastic material in this sample.

KSC8 (Group 1 – Microcrystalline, Primary fabric evident)

This sample is microcrystalline dolomite and may represent part of a stromatolite head (Figure B.18). Organic matter is distributed throughout this sample. It is found surrounding dolomite rhombs and as spherical nodules. The organic distribution defines the primary fabric in this sample. Cathodoluminescence of the sample shows two distinct phases of dolomitization (Figure B.19). The first phase is characterized by bright red luminescent dolomite rhombs. The second phase of dolomitization is characterized by dark red luminescent matrix surrounding the bright red luminescent dolomite rhombs. There are no veins and no clastic material in this sample.

WA 91/55 (Group 1 – Microcrystalline, Primary fabric evident)

This sample has two distinct regions. The first region is composed of two thin columnar stromatolite heads, which are composed of microcrystalline dolomite (Figure B.20). The second region is comprised of microcrystalline dolomitized sediments that fill in between the stromatolite heads. Most of the organic matter in this sample is contained in the stromatolite heads and defines the primary fabric of the rock. There is additional organic matter in the sediment rich section of the sample and this defines what appears to be bedding planes within the deposit. Cathodoluminescence of this sample

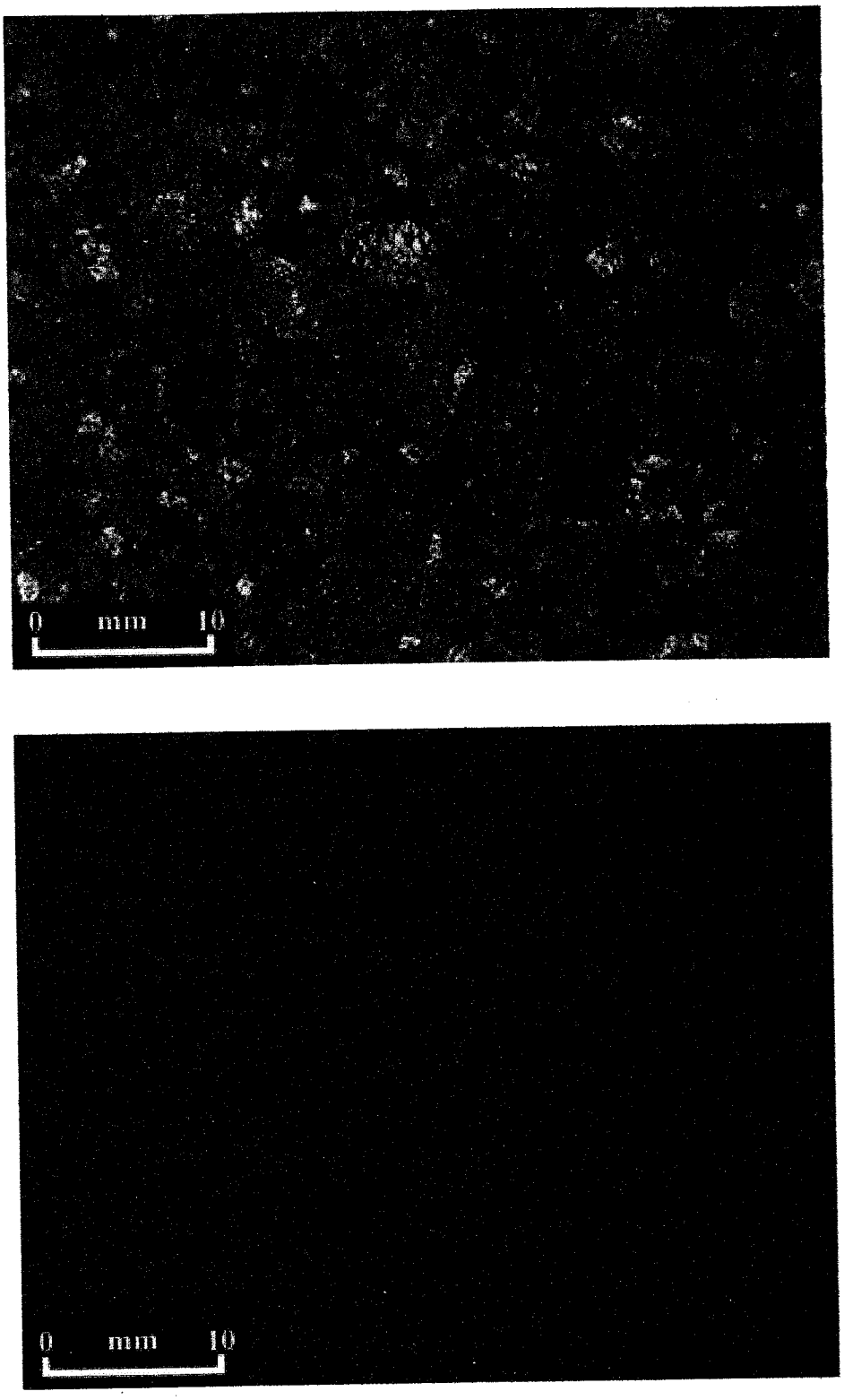

Figure B.17: Plane-polarized (upper image) and cathodoluminescent (lower image) photomicrographs of sample KSC7 showing a brightly luminescent vein.

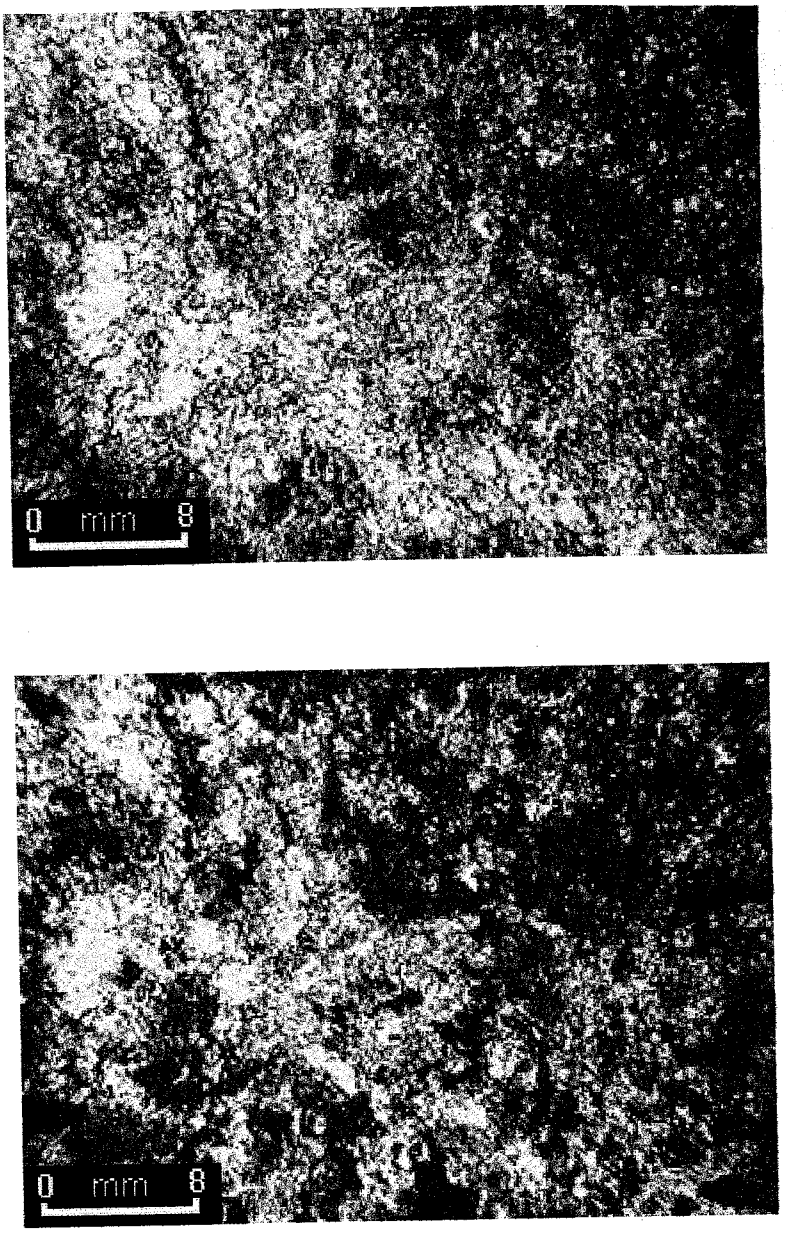

Figure B.18: Plane-polarized (upper image) and cross-polarized (lower image) photomicrographs of sample KSC8 showing microcrystalline dolomite.

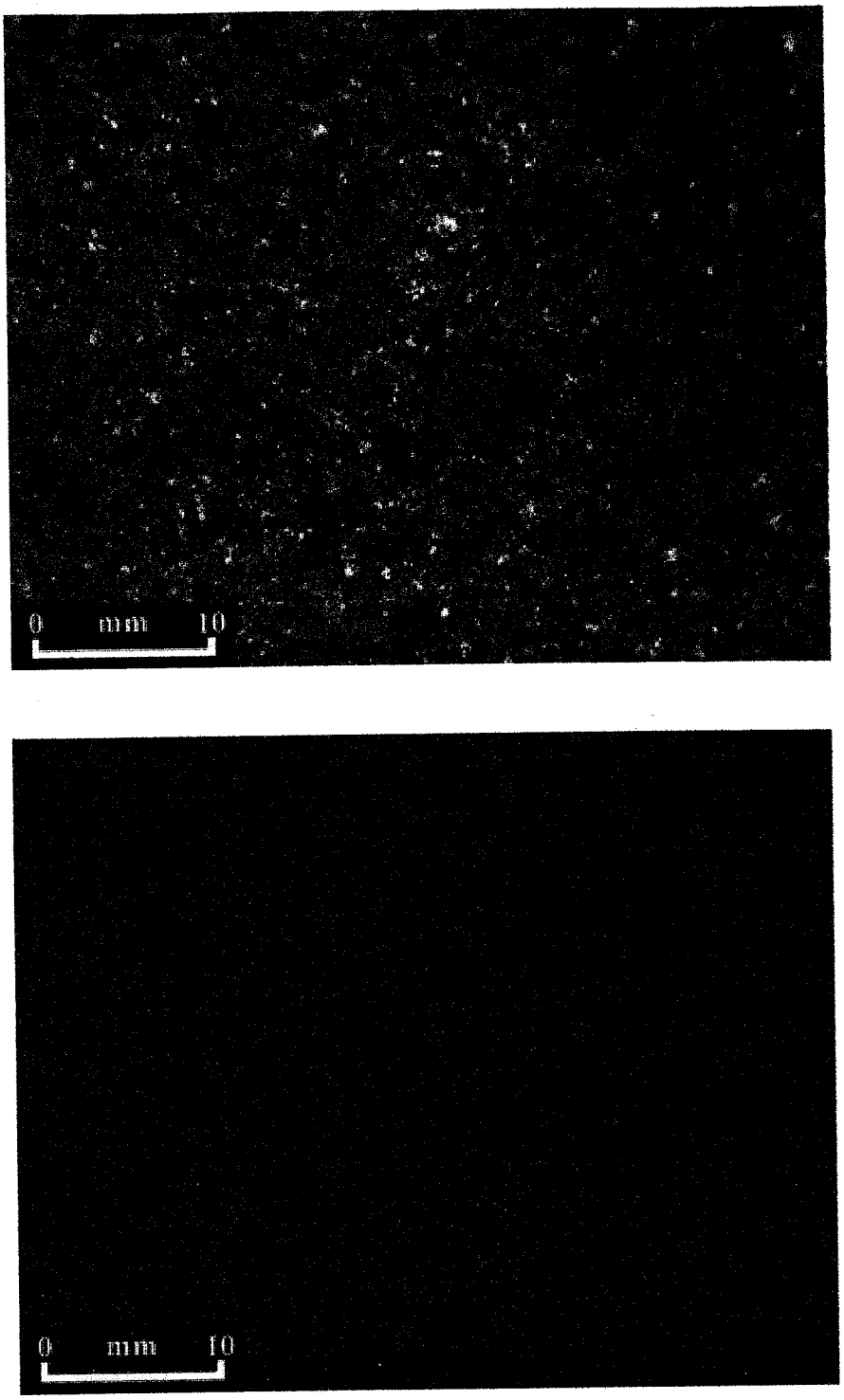

Figure B.19: Plane-polarized (upper image) and cathodoluminescent (lower image) photomicrographs of sample KSC8 showing two shades of luminescence.

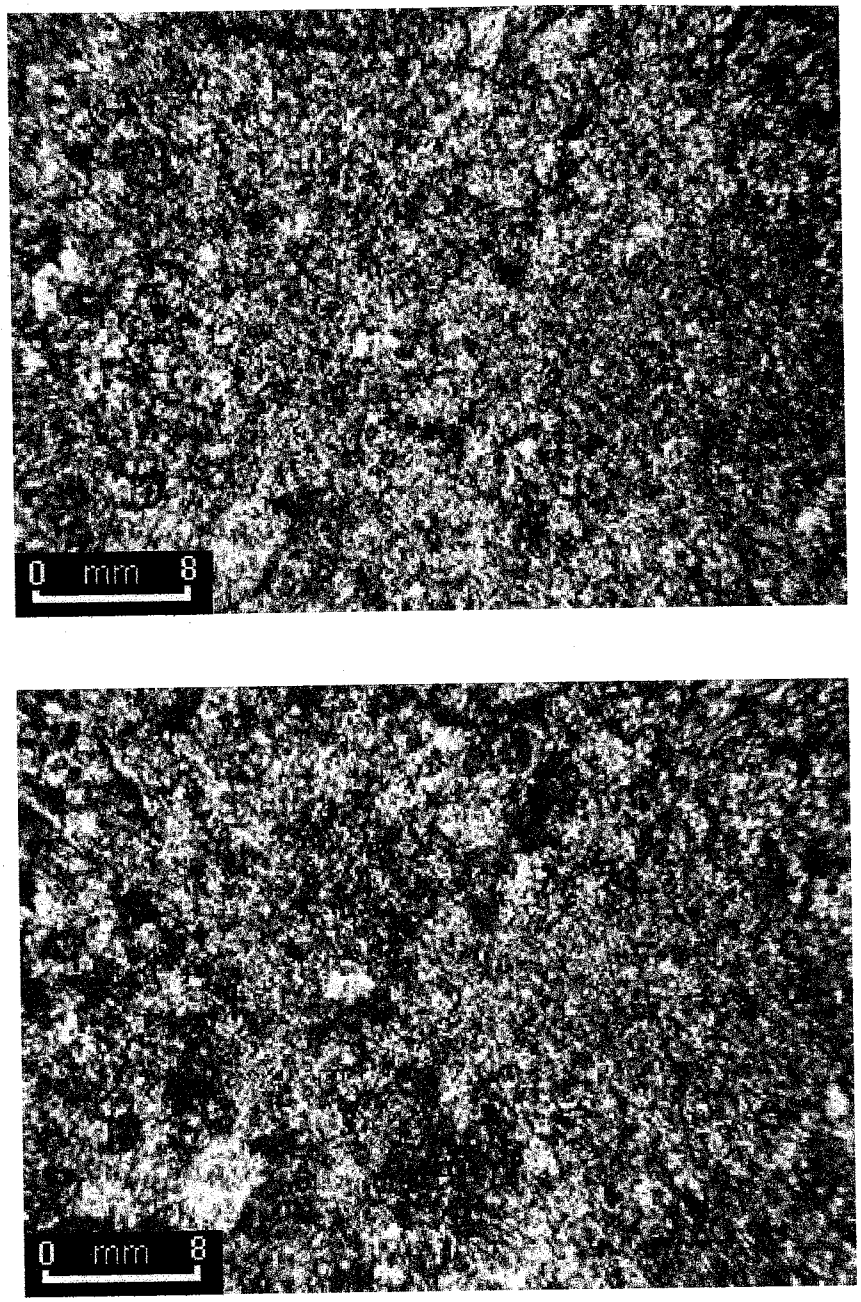

Figure B.20: Plane-polarized (upper image) and cross-polarized (lower image) photomicrographs of sample WA 91/55 showing microcrystalline dolomitization.

revealed that the sample had two very different regions of carbonate (Figure B.21). The stromatolites appear as bright red luminescent dolomite. The sediment fill has little to no luminescence. There are no veins in this sample.

WA 91/48 (Group 3 – Clastic sample, carbonate cement)

The thin section for sample number WA 91/48 reveals that this is a sandstone with a calcite cement. The clasts that make up this sample are predominantly feldspars, quartz, and chert although there are several smaller volcanic rock fragments. The calcite cement is twinned and in places is deformed around grains indicating that the rock was exposed to high pressures however, there is no indication of metamorphism. The calcite cement does not show any luminescence during cathodoluminescence. Organic matter is distributed evenly throughout the calcite cement. In addition, organic matter forms rims around clasts. Although there is veining in some of the clasts, there is no veining in the lithified rock.

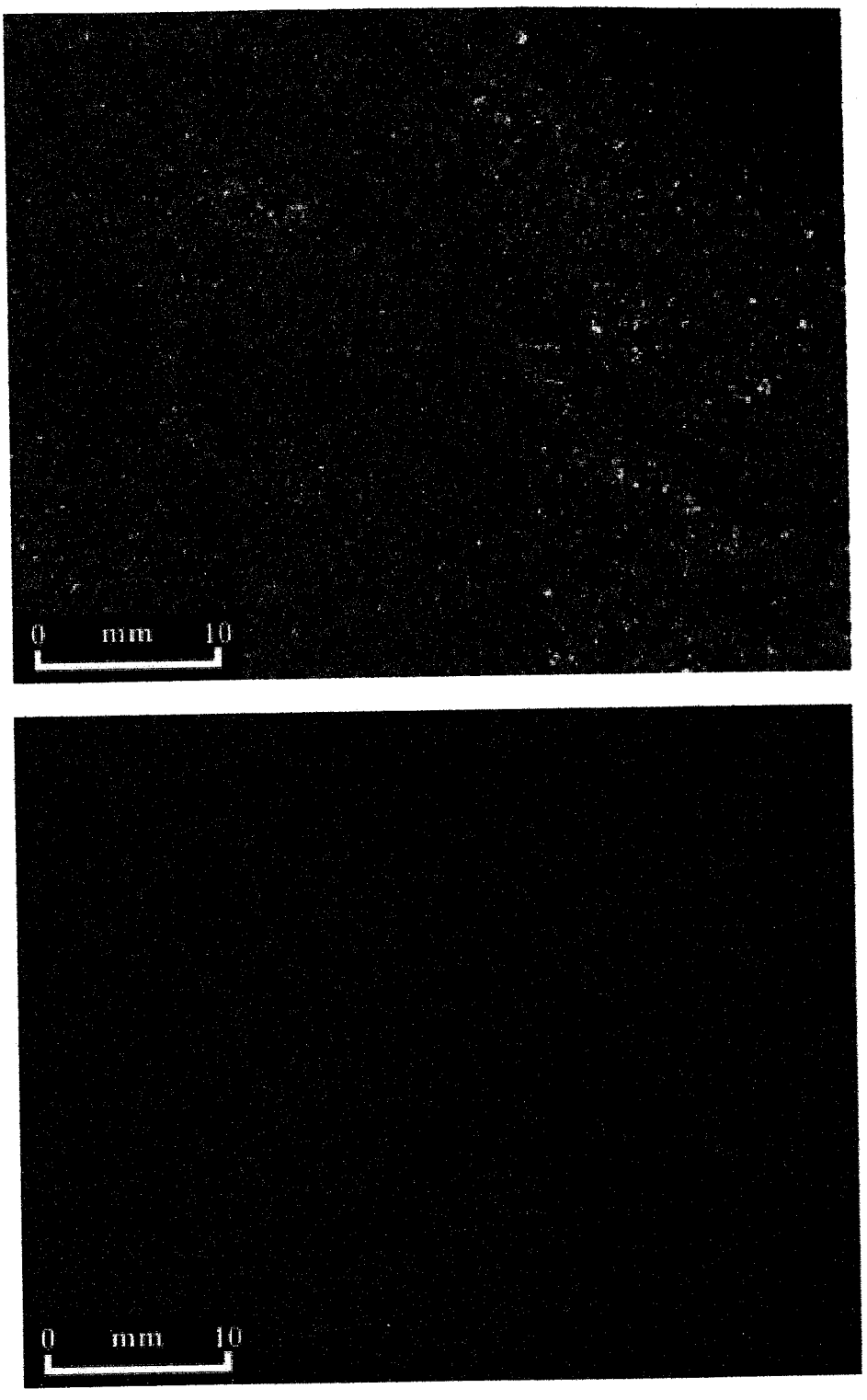

Figure B.21: Plane-polarized (upper image) and cathodoluminescent (lower image) photomicrographs of sample WA 91/55 showing the stromatolite head as bright red luminescent regions and the in-filled sediment as the non-luminescent regions.

Appendix C: Calibration standards used in ICP-MS analysis. Standards are listed in the order in which they were run.

Standard		Li		B		Ti		V		Cr		Co		Ni		Cu		Zn	
		Conc	Std Dev	Conc	Std Dev	Conc	Std Dev	Conc	Std Dev	Conc	Std Dev	Conc	Std Dev	Conc	Std Dev	Conc	Std Dev	Conc	Std Dev
ICV		**47.9**	2.2	**24.9**	0.4	**47.0**	0.5	**48.5**	1.7	**48.2**	6.6	**48.9**	0.8	**47.0**	0.6	**41.7**	0.1	**49.0**	0.5
	Expected Value	**50.0**		**25.0**		**50.0**		**50.0**		**50.0**		**50.0**		**50.0**		**50.0**		**50.0**	
ECS 20 ppb		**0.3**	22.6	**1.3**	5.2	**0.0**	100.0	**16.5**	2.1	**18.0**	1.6	**16.9**	1.2	**19.5**	2.2	**17.2**	2.8	**18.9**	1.9
	Expected Value							**20.0**		**20.0**		**20.0**		**20.0**		**20.0**		**20.0**	
Blank 1		**2.1**	13.9	**5.1**	5.7	**0.4**	73.1	**0.0**	8.9	**0.0**	90.5	**0.0**	13.6	**0.2**	7.9	**19.4**	0.4	**3.7**	0.4
Blank 2		**2.7**	2.7	**5.6**	5.2	**0.5**	25.8	**0.0**	7.6	**0.6**	5.3	**0.1**	9.1	**1.6**	4.6	**6.7**	0.9	**64.8**	0.1
	Expected Value	**0.0**		**0.0**		**0.0**		**0.0**		**0.0**		**0.0**		**0.0**		**0.0**		**0.0**	
ECS 20 ppb		**0.4**	7.2	**1.3**	3.5	**0.0**	51.0	**19.3**	0.3	**20.6**	0.4	**17.9**	0.9	**20.4**	1.1	**17.5**	0.9	**18.4**	1.1
	Expected Value							**20.0**		**20.0**		**20.0**		**20.0**		**20.0**		**20.0**	